Vortex Dynamics within the Laminar Separation Bubble over a NACA 0018 Airfoil at Low Reynolds Numbers

by

Andrew R. Lambert

A thesis
presented to the University of Waterloo
in fulfillment of the
thesis requirement for the degree of
Master of Applied Science
in
Mechanical Engineering

Waterloo, Ontario, Canada, 2015

I hereby declare that I am the sole author of this thesis. This is a true copy of the thesis, including any required final revisions, as accepted by my examiners.

I understand that my thesis may be made electronically available to the public.

Abstract

The structures formed in the separated shear layer within a Laminar Separation Bubble (LSB) over a NACA 0018 airfoil at a chord Reynolds number of 100,000 and Angles of Attack (AOA) of (5°, 8°, and 10°) were investigated. Techniques used during investigation include high-speed flow visualization synchronized with embedded microphones for pressure measurements.

High-speed flow visualizations reveal the formation of coherent structures within the laminar separation bubble. These structures develop from disturbances that roll up into vortices, may merge, and then break down as the shear layer reattaches. Microphone measurements indicate that the growth of the structures are accompanied by growth in a band of frequencies in the fluctuating surface pressures. When simultaneous visualizations and microphone measurements were compared, it was found that a local pressure minimum indicates a vortex passing over a microphone. The merging of vortices was found to result in the merging of the associated pressure minima. To track vortices along the separation bubble, the microphone signals were cross-correlated around the minima. This tracking matches well with the reference tracking of vortices from images.

The vortex dynamics at $AOA = 5°$, $8°$, and $10°$ were also compared. Visualizations show that structures decrease in scale at higher angles of attack, and show greater temporal variations. The spectra of pressure fluctuations show higher-frequency activity related to the smaller scales at greater angles of attack. The vortices at all of these angles of attack develop to a peak downstream of mean transition where roll-up is complete. At reattachment although the vortices come closer to the surface, the magnitudes of the pressure fluctuations decrease as the vortices break down. Merging of vortices was also investigated using the vortex tracking technique based on surface pressure fluctuations. Merging was present at $AOA = 5°$, $8°$, and $10°$, but more prevalent at larger angles of attack. Merging occurs at a range of intervals of vortices, and does not follow a dominant frequency from the disturbance environment.

Acknowledgements

I would like to thank my Master's supervisor Professor Serhiy Yarusevych for his support, guidance, and mentorship during the past nominal two years. His patience, encouragement, perceptiveness and knowledge have fostered an excellent environment for personal and professional growth.

I would like to thank Thomas M. Kirk and Holly Neatby for introducing me to Big Blue and its many intricacies. Your experience was invaluable and you both taught me a lot. I would particularly like to thank Tom for his participation in the flow visualization experiments, for both his expertise and streamlining the visualization process.

I would like to thank the visiting Professor Bulent Yaniktepe for his participation in early smoke-wire experiments that were developed into the techniques used in this thesis.

I would also like to thank the members of our office for their companionship and helpful discussions. I thank Sahil Mahey for his always enthusiastic discussions of the finer points of spectral analysis, and Jeff McClure and Eugene Zivkov for their dynamic discussions of vortices. I also thank John Kurelek for his tutelage in LaTeX. Thanks to Jia Cheng Hu for mentioning Pattern Recognition to me. Thanks to Chekema Prince, Jennifer Book, and Professor Sean Peterson for introducing me to running. February wasn't an ideal time to start, but it seemed to stick regardless.

Thanks are extended to friends outside of the office, both within the university and out in the wild world. Particular thanks go to Anik Islam and David (Yuk Hei) Wong for sharing the adventures of university life, and being models of dedication and perseverance.

Thanks go to my parents Robert and Carolyn Lambert, my three sisters Christine, Catherine and Laura, and the rest of my family. Your support, encouragement, and examples you lead are what have made it possible to reach this far in my formal education.

Thanks also to the Natural Sciences and Engineering Research Council of Canada as well as Bombardier Aerospace for funding this research, and to Stephen Colavincenzo and Guillaume Malaval for their supervision during the Industrial Postgraduate Scholarship placement.

Dedication

This thesis is dedicated to my parents Robert and Carolyn for their enduring support all of my life. The security you've offered and the opportunities you have made available have helped me to find a career path I'm passionate about and grow the perseverance to pursue it.

Table of Contents

List of Figures **ix**

Nomenclature **xvi**

1 Introduction **1**

2 Background **4**

2.1 Airfoils at Low Reynolds Numbers 4

2.1.1 Operation at Low Reynolds Numbers 4

2.1.2 Mean Laminar Separation Bubble 7

2.1.3 Time-varying Laminar Separation Bubble 10

2.2 Vortex Dynamics in Shear Flows 13

2.3 Surface Pressure Fluctuations for Flow Diagnostics 15

3 Experimental Method **18**

3.1 Experimental Setup 18

3.1.1 Wind Tunnel Facility 18

3.1.2 Airfoil Test Model 19

3.2 Measurement Techniques 20

3.2.1 Pressure Measurements 20

3.3 Flow Visualization 21

4 Flow Physics **25**
4.1 LSB Structure . . . 25
4.2 Pressure Fluctuations . . . 29
4.3 Vortex Merging . . . 37
4.4 Vortex Tracking . . . 41
4.4.1 Image-Based Tracking . . . 41
4.4.2 Tracking by Cross-Correlation . . . 45
4.4.3 Pattern Recognition . . . 49

5 Vortex Dynamics Characterization **52**
5.1 Flow Visualization . . . 52
5.2 Separation Bubble Characterization . . . 53
5.3 Vortex Merging Comparison . . . 84

6 Conclusions **90**
6.1 Flow Physics . . . 90
6.2 Vortex Dynamics Characterization . . . 92

7 Recommendations **96**

PERMISSIONS **98**

References **100**

APPENDICES **109**

A Experimental Uncertainty **110**
A.1 Uncertainty in Experimental Setup . . . 110
A.2 Uncertainty in Static Pressure Measurements . . . 111
A.3 Microphone Measurement Uncertainty . . . 112
A.4 Flow Visualization Uncertainty . . . 113
A.5 Vortex Tracking by Pressure Signals Uncertainty . . . 113

B Flow Visualization Intrusiveness **115**

List of Figures

2.1 Schematic representation of airfoil with laminar separation. Part a) shows no reattachment and a wide wake, while b) shows turbulent reattachment and a narrow wake. Image from Ref. [1]. 6

2.2 Horton's [2] representation of the mean laminar separation bubble. The boundary layer separates and reattaches over a reverse-flow vortex. 8

2.3 Shadowgraph of mixing layer between nitrogen and helium [3]. Disturbances are amplified into vortices. 11

2.4 Dye visualization of vortex merging in a free shear layer [4]. Velocity fluctuations are introduced at the first subharmonic of the vortex formation frequency. 14

3.1 Schematic of the University of Waterloo Adaptive-Wall Wind Tunnel, image from Boutilier [5]. 19

3.2 Airfoil model with chordwise static pressure taps and embedded microphones. 20

3.3 Schematic of flow visualization for flow around the airfoil 22

3.4 Schematic of setup for vertical separation bubble visualization. 23

3.5 Schematic of setup for horizontal separation bubble visualization. 24

4.1 Flow visualization around the airfoil. Flow is from left to right. The outline of the airfoil at the wind tunnel wall is the dashed line, the surface of the airfoil at the plane of the smoke is the solid line, and the dotted lines show the visual foreshortening of the airfoil. 26

4.2 Flow visualization within laminar separation bubble. The wire is located at $x/c = 0.2$ and the free stream is from left to right. Note that a reflection of the smoke is visible in the airfoil surface. 27

4.3 Mean surface pressure distribution on the airfoil. Estimated locations of mean separation (S), transition (T), and reattachment (R) are indicated by the corresponding letters, with an uncertainty of half of the pressure tap spacing. Note that the ordinate axis is reversed. 28

4.4 Time-averaged visualization of a separation bubble, with flow from left to right. 28

4.5 Sequence of separation bubble visualizations. The consecutive images are separated by 0.2 ms. The dotted lines connect the same vortices in the images, with the slope of the lines being indicative of convective speeds of the structures. 30

4.6 Sequence of top view bubble visualizations with flow from top to bottom. Time interval between images is 0.4 ms. 31

4.7 Development of surface pressure fluctuations along the separation bubble. . 32

4.8 Root-mean-square of surface pressure fluctuations along the separation bubble. The locations of mean separation, transition, and reattachment estimated from mean surface pressure distribution are shown by S, T, and R, respectively. 33

4.9 Spectra of surface pressure fluctuations along the airfoil. 34

4.10 Surface pressure fluctuations induced by shear layer vortex "V" convecting over the microphone indicated in red. A sequence of images in a), b), and c) are shown with their instantaneous pressure measurements in d). 35

4.11 Pressure field induced by a single ideal vortex. 36

4.12 Pressure field induced by a sequence of ideal vortices. 36

4.13 Visualization of vortex merging inside the separation bubble. The consecutive images are separated by 0.2 ms. The dotted lines connect the same vortices in the images, with the slope of the lines being indicative of convective speeds of the structures. 38

4.14 Surface pressure signals produced due to merging of two shear layer vortices. 39

4.15 Inviscid simulation of a pair of vortices of equal strength. Vortices rotate in a clock-wise direction, with a mean flow imposed from left to right. 40

4.16 Experimental streamwise velocity profile at $x/c = 0.24$. These measurements were performed by Kirk [6] using hot-wire anemometry. 41

4.17 Comparison of rates of change of convective velocities estimated at $x/c = 0.3$. The experimental results are based on Kirk [6] and the simulation data serves to approximate the effect of induced velocity. 42

4.18 Sample of vortex positions identified from flow visualization images. The centres are identified by fitting an ellipse to the crest that forms as well as the displacements of the smoke filament. Images are presented at intervals of 0.4 ms. 43

4.19 Vortex positions as identified from flow visualization images. 44

4.20 The positions of vortices above the chordline as identified from flow visualizations. The moving average is calculated over 75 vortex positions. 45

4.21 Schematic of vortex tracking method for two subsequent microphones. The vortices are detected upstream at Mic 1. A cross-correlation is performed between the two signals to determine the average speed and hence the time the vortex is expected to pass the downstream microphone. Windowed segments of the signals are cross-correlated to determine the positions of the individual vortices through time. 46

4.22 Example of typical vortex tracking between two microphones, showing a range of individual convective velocities. The normalized pressures are plotted through time, centered at the chord-wise position of the microphones. . 47

4.23 Schematic of vortex tracking along the separation bubble, showing tracking results. Merging is detected when two vortices upstream progress to a single vortex downstream, as at $t = 94.4$ ms and $x/c = 0.3$. 48

4.24 Positions of vortices as identified from flow visualizations at $AOA = 8°$ are compared with the positions identified from the cross-correlation of minima. 49

4.25 Sample of distributions of features for the detected minima. The four classes are shown as the smaller circles, while the averages are shown with the larger unfilled circles. 51

5.1 Sequence of separation bubble visualizations at $AOA = 0°$ with flow from left to right. Time interval between images is 1.25 ms. Dotted lines give an indication of the spacings and speeds of the vortices. 54

5.2 Sequence of separation bubble visualizations at $AOA = 5°$ with flow from left to right. Time interval between images is 1 ms. Dotted lines give an indication of the spacings and speeds of the vortices. 55

5.3 Sequence of separation bubble visualizations at $AOA = 8°$ with flow from left to right. Time interval between images is .6 ms. Dotted lines give an indication of the spacings and speeds of the vortices. 56

5.4 Sequence of separation bubble visualizations at $AOA = 10°$ with flow from left to right. Time interval between images is .4 ms. Dotted lines give an indication of the spacings and speeds of the vortices. 57

5.5 Mean surface pressure distributions for angles of attack of 0°, 5°, 8°, and 10°. The locations of mean Separation, Transition, and Reattachment are indicated by S, T, and R respectively. Note that the ordinate axis is reversed. 58

5.6 Variation with angle of attack of positions of mean separation, transition, and reattachment as identified from mean surface pressure measurements at $AOA = 0°$, 5°, 8°, and 10°. 59

5.7 Root-mean-square of pressure fluctuations for microphone signals plotted along the chord at $AOA = 5°$, 8°, and 10°. 61

5.8 Power spectral density of microphone pressure signals along the separation bubble at $AOA = 5°$, 8°, and 10°. 63

5.9 Root-mean-square of pressure fluctuations for bandpass-filtered signals plotted along the chord at $AOA = 5°$, 8°, and 10°. 64

5.10 Root-mean-square of pressure fluctuations for bandpass-filtered signals plotted along separation bubble length at $AOA = 5°$, 8°, and 10°. 64

5.11 Development of amplitudes of pressure minima along the airfoil at angles of attack of 5°, 8°, and 10°. 66

5.12 Development of amplitudes of pressure minima along normalized separation bubble length at angles of attack of 5°, 8°, and 10°. 67

5.13 Tracking of vortices and magnitudes of pressure minima along the separation bubble at $AOA = 5°$. A green circle indicates an increase in the magnitude of the minimum (more negative) while a red circle shows a decrease. The blue line exponentially interpolates where the pressure minima would reach a threshold value of $C_p = -0.025$. The percent of vortices whose magnitudes decrease from the upstream location is presented for $AOA = 5°$ in (b). . . 69

5.14 Tracking of vortices and magnitudes of pressure minima along the separation bubble at $AOA = 8°$. A green circle indicates an increase in the magnitude of the minimum (more negative) while a red circle shows a decrease. The blue line exponentially interpolates between the pressure minima to show where the pressure would reach a threshold value of $C_p = -0.025$. A summary of the percent of vortices whose magnitudes decrease from the upstream location along the separation bubble is presented for $AOA = 8°$ in (b). . . 70

5.15 Tracking of vortices and magnitudes of pressure minima along the separation bubble at $AOA = 10°$. A green circle indicates an increase in the magnitude of the minimum (more negative) while a red circle shows a decrease. The blue line exponentially interpolates between the pressure minima to show where the pressure would reach a threshold value of $C_p = -0.025$. A summary of the percent of vortices whose magnitudes decrease from the upstream location along the separation bubble is presented for $AOA = 10°$ in (b). 71

5.16 Summary of percent of vortices whose magnitudes decrease from the upstream location along the separation bubble, presented for $AOA = 5°$, $8°$, and $10°$. 72

5.17 Time intervals between consecutive vortices at the microphone locations (a-c) indicated by the white circles for an angle of attack of $5°$. The solid red lines on the distributions of the intervals indicate the average time interval and the dashed red lines indicate plus and minus the standard deviation. . 74

5.18 Time intervals between consecutive vortices at the microphone locations (a-c) indicated by the white circles for an angle of attack of $8°$. The solid red lines on the distributions of the intervals indicate the average time interval and the dashed red lines indicate plus and minus the standard deviation. . 74

5.19 Time intervals between consecutive vortices at the microphone locations (a-c) indicated by the white circles for an angle of attack of $10°$. The solid red lines on the distributions of the intervals indicate the average time interval and the dashed red lines indicate plus and minus the standard deviation. . 75

5.20 The development of the time interval distributions for $AOA = 5°$, $8°$, and $10°$. The average interval and standard deviations are normalized by the maximum value at each angle of attack. 76

5.21 The distributions of convective velocities for vortices at $AOA = 5°$. The velocities in a)-c) are calculated for the points indicated by white circles which mark the mid-point between consecutive microphones. The solid red lines show the average convective velocities of the vortices while the dashed red lines show plus and minus one standard deviation. 77

5.22 The distributions of convective velocities for vortices at $AOA = 8°$. The velocities in a)-c) are calculated for the points indicated by white circles which mark the mid-point between consecutive microphones. The solid red lines show the average convective velocities of the vortices while the dashed red lines show plus and minus one standard deviation. 78

5.23 The distributions of convective velocities for vortices at $AOA = 10°$. The velocities in a)-c) are calculated for the points indicated by white circles which mark the mid-point between consecutive microphones. The solid red lines show the average convective velocities of the vortices while the dashed red lines show plus and minus one standard deviation. 78

5.24 The distributions of convective velocities for vortices at $AOA = 5°$, 8°, and 10°, presented along the normalized bubble length. The bars indicate plus and minus one standard deviation. 79

5.25 For an angle of attack of 5°, microphone signals and their accompanying continuous wavelet transform are presented along the separation bubble. The microphone locations are indicated with the white dots and a)-c) markers. 81

5.26 For an angle of attack of 8°, microphone signals and their accompanying continuous wavelet transform are presented along the separation bubble. The microphone locations are indicated with the white dots and a)-c) markers. 82

5.27 For an angle of attack of 10°, microphone signals and their accompanying continuous wavelet transform are presented along the separation bubble. The microphone locations are indicated with the white dots and a)-c) markers. 83

5.28 Progression of percentage of merged vortices along the airfoil, for $AOA = 5°$, 8°, and 10°. 84

5.29 Progression of percentage of merged vortices along the normalized position within the separation bubble, for $AOA = 5°$, 8°, and 10°. 85

5.30 Time sequence of detected vortices at the most upstream location for angles of attack of 5°, 8°, and 10°. The symbols of the vortices indicate whether they merge downstream of their initial detection. 87

5.31 Intervals of vortices between merging events in Fig. 5.30a-5.30c. 88

5.32 Power spectra of the merging time sequences of over 200 vortices sampled in Fig. 5.30a-5.30c, interpolated for an even sampling rate. 89

B.1 Mean surface pressure distributions along the airfoil are presented for $AOA = 0°$, $5°$, $8°$, and $10°$ with and without the smoke wire in the separation bubble. Uncertainty is on the order of the symbol size. 116

B.2 Root-mean-square of pressure fluctuations along the airfoil are presented for $AOA = 5°$, $8°$, and $10°$ with and without the smoke wire in the separation bubble. 117

B.3 Pressure spectra along the airfoil are presented for $AOA = 5°$, with and without the smoke wire in the separation bubble. 118

B.4 Pressure spectra along the airfoil are presented for $AOA = 8°$, with and without the smoke wire in the separation bubble. 119

B.5 Pressure spectra along the airfoil are presented for $AOA = 10°$, with and without the smoke wire in the separation bubble. 120

Nomenclature

AOA	angle of attack
c	airfoil chord length [m]
C_p	coefficient of pressure for fluctuating pressures. $= \frac{p}{q_\infty}$
$\lvert C_{p,min}\rvert^{mic_i}$	magnitudes of pressure minima at a given microphone
C_p^{min}	coefficient of pressure for pressure minima. $= \frac{p}{q_\infty}$
C_p'	coefficient of pressure for the root-mean-square of fluctuating pressures. $= \frac{p_{rms}}{q_\infty}$
C_P	coefficient of pressure for mean pressures. $= \frac{P-P_0}{q_\infty}$
E_{pp}	power spectral density of pressure fluctuations [Pa^2/Hz]
f	frequency[Hz]
f_0	characteristic frequency of the amplified disturbances [Hz]
p	fluctuating surface pressure [Pa]
P	mean surface pressure [Pa]
P_0	reference pressure, measured at a reference port in the wind tunnel wall [Pa]
q_0	freestream dynamic pressure [Pa] $= 0.5\rho U_0^2$
R	location of mean reattachment, identified from surface pressure distributions
Re_c	chord-based Reynolds number, $= \frac{U_0 c}{\nu}$
S	location of mean separation, identified from surface pressure distributions
t	time [ms]
$t_n - t_{n-1}$	time interval between consecutive vortices [ms]
T	location of mean transition, identified from surface pressure distributions
U	streamwise velocity [m/s]
U_e	edge velocity [m/s] $= U_0(1 - C_P)^{1/2}$

U_0	free-stream velocity [m/s]
x	position along chord from leading edge [m]
y	position above airfoil surface [m]
Y	position above airfoil chord line [m]
z	position from airfoil mid-span [m]
ρ	density of air [kg/m^3]
ν	kinematic viscosity of air [m^2/s]

Chapter 1

Introduction

Low-Reynolds-Number airfoils are an area of great practical interest, due to their emergent applications in micro-air vehicles and small wind turbines [7]. At Reynolds numbers below around 500,000, airfoil performance is strongly impacted by the presence of the Laminar Separation Bubble (LSB) structure on the airfoil's suction side [8]. In this structure, the boundary layer separates, transitions to turbulent flow, and reattaches downstream. The localized separation changes the pressure distribution over the airfoil and tends to reduce lift and increase drag. Passive methods to contend with the LSB's negative impact include turbulators to transition the flow, and optimizing airfoil design to encourage transition in the LSB earlier along the airfoil [9]. Acoustic excitation and other forms of active control aim to delay separation and directly manipulate transition within the laminar separation bubble [10]. These active control methods necessitate some form of sensing capability to optimize the applied control.

At low Reynolds numbers, the boundary layer can remain laminar past the suction peak on the airfoil's suction side [11]. This laminar boundary encountering an adverse pressure gradient is susceptible to separation. As the boundary layer separates, it creates a separated shear layer [11]. This separated shear layer is sensitive to disturbances, which are amplified through the Kelvin-Helmholtz instability [12]. Previous experimental studies have found that these disturbances may roll up into vortices that convect along the airfoil [13]. The vortices that are formed within the laminar separation bubble play an important role in its characteristics. Vortical structures give shape to the development of unsteadiness in the LSB. Merging of these larger-scale vortices is important to mixing-layer growth in transitional and turbulent flows [4, 14]. If this transitional flow reattaches to the airfoil, then a turbulent boundary layer begins to redevelop and the stalled state is avoided [15]. These vortices also contribute to fluctuating loading on airfoils, which may induce vibra-

tions and control problems in flight vehicles [16]. Vortices passing over the trailing edge of airfoils can also create noise, which is a common concern for wind turbine installations [17]. Given the importance of vortices to the transition and reattachment in the LSB, and the impact of the LSB on airfoil performance, a non-intrusive method to quantify vortex activity would be of benefit in the understanding and application of low-Reynolds number airfoils.

The evolution of vortices within shear flows has been the subject of previous research, with their impact in LSBs the subject of further investigations. Recent investigations by Marxen et al. [18], and Burgmann and Schroeder [13] have probed the role of these vortices in the transition and reattachment processes in an LSB over a flat plate and airfoil. Marxen [19] found that it was the coherent structures and not just transition that play a large role in reattachment.

Previous investigations of laminar separation bubbles and other separating-reattaching flows have found that the flow development can be related to surface pressure fluctuations [1, 20]. Previous investigations of the LSB over a NACA 0025 airfoil have found that the frequencies of amplified disturbances from hot-wire velocity measurements are mirrored in the spectra measured with embedded microphones [1]. These microphone measurements have been further used to measure growth, convection rates, and frequencies of the disturbances[21]. Surface pressure fluctuations have also been used for conditional averaging of velocity measurements in the separating-reattaching flow downstream of a backward-facing step [22, 23, 24]. Averaging the velocities during a strong minimum showed the presence of vortices over the pressure sensor. Synchronized PIV and pressure measurements over a backward-facing step also relate pressure minima to the convection of vortical structures [25]. Recent visualizations of the separation bubble over a NACA 0018 showed the evolution of the disturbances into coherent vortices that convected along the separation bubble [6]. At certain angles of attack, the vortices were also observed to merge before breaking down. By directly tying the structures within the flow to surface pressure fluctuations, the activity of structures within laminar separation bubbles can be gleaned. The growth, interaction, and breakdown of individual vortices within LSBs over airfoils and their accompanying pressure signatures are not well-understood. An investigation into the relationship between flow structures in an LSB and surface pressure fluctuations can give the basis by which to develop arrays of embedded microphones into a tool for airfoil flow sensing and event tracking.

The focus of this investigation is the dynamics of the vortices that develop within the laminar separation bubble. Flow development is investigated over a NACA 0018 airfoil model with embedded microphones. The pressure signals were synchronized with high-speed separation bubble flow visualizations to relate pressure fluctuations to flow

structures. This relationship was employed to detect, track, and analyze the interactions between vortices formed within the LSB. The main objectives of this study are as follows:

1. Characterize surface pressure fluctuations and structures formed within the Laminar Separation Bubble by
   (a) performing high-speed flow visualizations of the separation bubble, synchronized with surface pressure fluctuation measurements
   (b) analyzing the pressure fluctuations and relating pressure signal features directly to the flow structures
2. Develop and validate models to build quantitative statistics on vortex dynamics using surface pressure fluctuations by
   (a) creating methods to track structures and distinguish events within the flow
   (b) applying these methods to quantify the activity of these structures under different conditions

This investigation is presented in the following chapters. A background on LSBs and the related fluid phenomena is presented in Chapter 2. The models, facilities, and experimental studies used in this investigation are described in Chapter 3. Chapter 4 describes the LSB, the structures that develop within the LSB and the pressure fluctuations associated with the structures. The changes in vortex dynamics with angle of attack are presented in Chapter 5. The conclusions and recommendations based on this work are presented in Chapters 6 and 7 respectively.

Chapter 2

Background

The main focus of this thesis is the study of the formation, evolution, and dynamics of coherent structures within the laminar separation bubble (LSB). Topics relevant to the discussion of the LSB and its main features are presented in the following sections. Section 2.1 outlines previous findings on the features and topology of LSBs. The related topic of dynamics of vortices within free shear layers is discussed in Section 2.2. Previous research on the use of surface pressure fluctuations for flow diagnostics is explored in Section 2.3, including the previous work performed on the experimental model used in this investigation.

2.1 Airfoils at Low Reynolds Numbers

2.1.1 Operation at Low Reynolds Numbers

Although airfoil performance is generally worse at lower Reynolds numbers, many engineering applications necessitate operation at these conditions [8]. Applications of low-Reynolds airfoils extend from small wind turbines to sailplanes and micro air vehicles, with different airfoil design requirements for each [26, 27]. The low speeds of unpowered sailplanes make them a natural area of interest, with a focus on high lift-to-drag performance and control [26]. Similar concerns exist for unmanned aerial vehicles, which must be able to carry their payload for sufficient time to complete their tasks, while having control systems that can accomodate the lift and stall characteristics of low-Re airfoils [16, 28]. With the continually growing emphasis on renewable energy, an area of application with great interest is small wind turbines [29]. In this application, the blades must operate

efficiently in the range of relatively low wind speeds they can encounter in the atmospheric boundary layer [30]. Wind turbines are also known to cause aerodynamic noise from vortices and turbulent boundaries passing over the blade's trailing edge [17]. Low-Reynolds number airfoils have thus been the focus of much research.

Airfoils at a chord Reynolds under around 500,000 operate in the low-Reynolds-number regime [10]. At these Reynolds numbers, the laminar boundary layer separates as it confronts an adverse pressure gradient past the suction peak on the airfoil's suction side. This separated flow is unstable to a range of disturbances and amplifies them to flow transition [12]. The increased momentum transfer within this transitioned flow can lead to flow reattachment if it happens early enough over the airfoil. Otherwise, the airfoil will remain stalled [8]. If the flow reattaches, it forms a redeveloping turbulent boundary layer [15]. This separating-reattaching structure is called a Laminar Separation Bubble (LSB). If the airfoil remains stalled, there is a large decrease in airfoil lift and increase in drag [8]. Schematic representations of the stalled and un-stalled states are shown in Fig. 2.1. While this stalled regime is important to the performance and application of low-Reynolds number airfoils, the flow regime where a separation bubble forms is the focus of this investigation.

The presence of the LSB has a more subtle impact on performance beyond determining airfoil stall. The stagnant fluid near the surface below the separated flow is accompanied by a pressure plateau that modifies the airfoil's pressure distribution from that expected for the inviscid case [15]. Early investigations [31, 32, 33] found that the location and extent of this pressure plateau that indicates the presence of this "bubble of laminar separation" [31] could have a large impact on the performance of the airfoil. As early as 1933 [34, 35], the effect of this "thin airfoil stall" was found to decrease the potential lift of airfoils. When the plateau in the pressure distribution occurs close to the suction peak, it reduces the magnitude of this peak and may reduce the overall lift that an airfoil produces [31]. Tani [15] also further distinguished between "short" and "long" LSBs. In short LSBs, transition and reattachment occur over a relatively short distance and they have a small impact on the overall pressure distribution compared to long LSBs. Experiments on a NACA 64A006 airfoil found that the bursting of the short bubbles to long bubbles produced an abrupt drop in the lift curve [32]. This is accompanied by a sharp increase in pressure and, hence, overall drag. The presence of the LSB also increases the boundary layer momentum thickness, which further increases theg likelihood of turbulent boundary layer separation at the airfoil's trailing edge [36]. However, the pressure plateau may also increase the lift of airfoils by extending the region with low pressure over a greater extent of the airfoil, and the lift slope of the airfoil may be steeper than predicted from thin-airfoil theory [37]. Boundary layer thickness and state also change the skin friction drag that the airfoil experiences. Overall, the effect of laminar separation and laminar separation bubbles tends

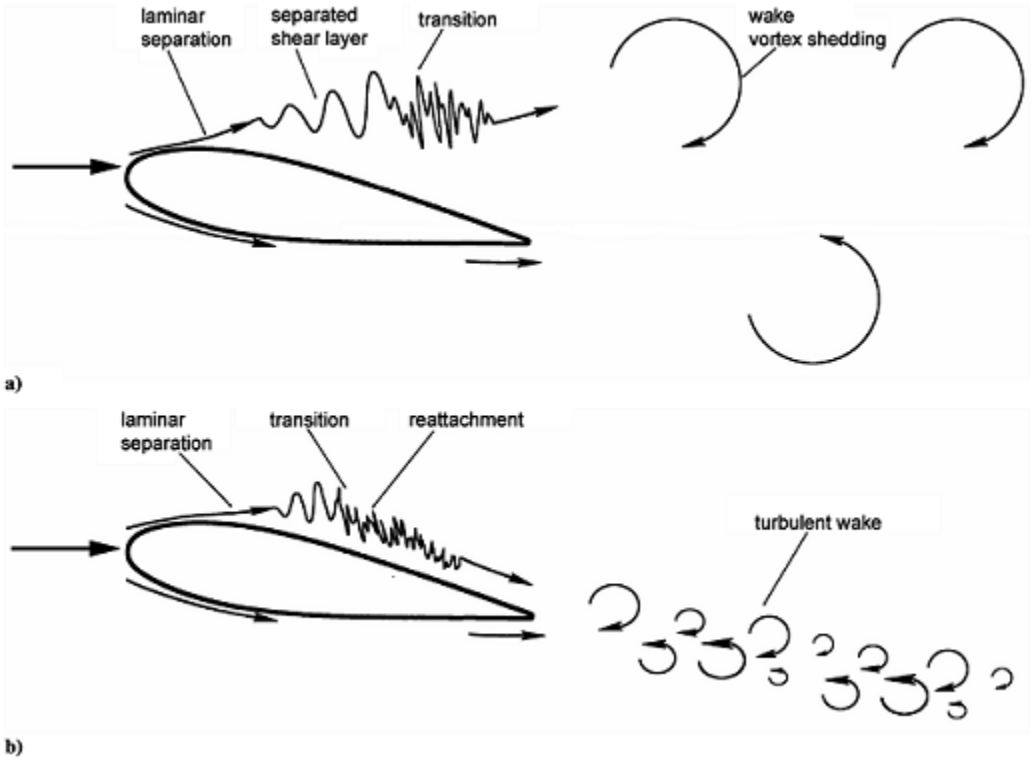

Figure 2.1: Schematic representation of airfoil with laminar separation. Part a) shows no reattachment and a wide wake, while b) shows turbulent reattachment and a narrow wake. Image from Ref. [1].

to limit the airfoil performance, particularly at lower Reynolds numbers.

LSB characteristics for a given airfoil primarily depend on the Reynolds number and angle of attack [38], but are sensitive to secondary factors. These secondary factors impact the disturbances which are amplified to transition, and transition is important to the formation of separation bubbles. Secondary factors include freestream turbulence level, acoustic and other freestream disturbances and surface roughnes [39]. The stalling of airfoils at lower Reynolds numbers is also known to suffer from hysteresis, where the state of stall or reattachment at a single angle of attack depends on whether the angle was approached from a stalled or attached flow state. At higher Reynolds numbers, the attached flow may develop to transition before encountering the adverse pressure gradient, which the turbulent boundary layer is better able to resist [8]. Airfoils with rough surfaces tend to promote boundary layer transition by introducing disturbances into the boundary layer

[39]. Surface roughness that induces boundary layer transition prevents the formation of the LSB, but the increased skin friction drag can reduce overall performance at higher Reynolds numbers [39]. Since transition in the separated shear is due to the amplification of disturbances, the flow is sensitive to different disturbances [40]. High free-stream turbulence intensities can prompt transition in the attached boundary layer [41]. The initial disturbance level and frequencies in the separated shear layer also impacts the development required to reach transition. Increasing the freestream turbulence reduces the effect of hysteresis by promoting transition [40]. The sensitive nature of transition over airfoils at low Reynolds numbers and the impact on the measured airfoil performance requires careful experimentation to avoid introducing disturbances to the flow.

Given the sensitivity of airfoil performance to experimental conditions, there has also been research into how this can be beneficially exploited. A common method to increase performance over a certain operational range are roughness elements that trip the flow to transition [7, 10, 26, 27, 33]. Early experiments [33] used distributed surface roughness as well as a boundary layer trip wire to promote transition and found improved performance at Reynolds numbers between 28,000 and 168,000. Mueller [39] found that grit roughness near the leading edge of an airfoil promotes attachment and reduces the unexpected behaviour of thick symmetric airfoils at lower Reynolds number, where increasing the angle of attack reduced the lift. However, at higher Reynolds numbers, the increased momentum transfer within the turbulent boundary layer increases skin friction and encourages earlier trailing-edge separation which reduces lift. Experiments with acoustic excitation of the flow found that specific frequencies could cause the flow to transition, leading to an increase in the lift available [33, 39]. Other studies explored suction or blowing, and synthetic jets to control separation [42]. Suction and blowing manipulate boundary layer thickness to delay separation [43]. Synthetic jets have no net mass flow, but create vortical structures that increase momentum transfer in the boundary layer [44]. Plasma actuators are another recent method for controlling transition. For example, Dielectric Barrier Discharge plasma actuators use high-voltage AC electrodes to create body force on the particles. These plasma actuators can be used to impart momentum to the boundary layer and have been used to delay separation over a cylinder and suppress vortex shedding [45]. By closing the loop on these control methods, control strategies can be optimized to control airfoil performance characteristics.

2.1.2 Mean Laminar Separation Bubble

At flow conditions where a laminar separation bubble exists, its mean structure as introduced earlier is well-described by the picture presented in Fig. 2.2. Within the low-

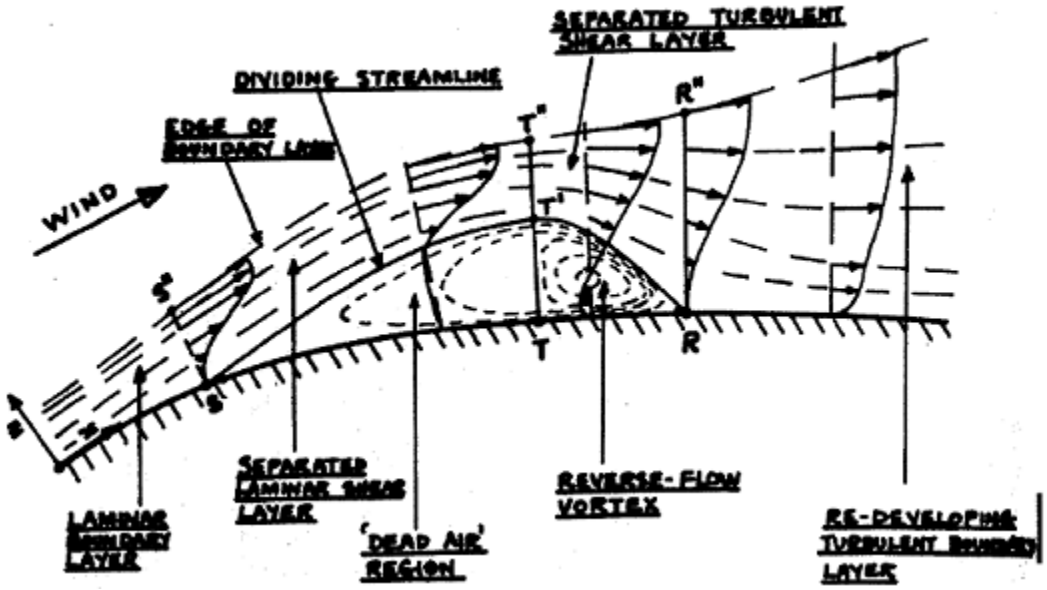

Figure 2.2: Horton's [2] representation of the mean laminar separation bubble. The boundary layer separates and reattaches over a reverse-flow vortex.

Reynolds number regime, there is insufficient flow development for the laminar boundary layer to transition while attached [41]. These laminar boundary layers are more prone to separation than turbulent boundary layers which have increased momentum transfer [46]. As the laminar boundary layer on the suction side of the airfoil encounters an adverse pressure gradient past the suction peak, the laminar boundary layer separates. When this boundary layer separates it forms a separated shear layer with reverse flow near the airfoil's surface. The inflected velocity profile of this separated flow is sensitive to disturbances, which are amplified through the Kelvin-Helmholtz instability [47]. The initial growth of these disturbances is well-described by linear stability theory, where the disturbances are amplified exponentially as they convect with the flow [12]. From the initial level of disturbances, the disturbances develop until they reach sufficient amplitude for their interactions to be nonlinear, and deviate from their exponential growth [48]. These disturbances have been observed to roll up into vortices before they break down to turbulence [49]. The increased momentum transfer in a turbulent shear layer accelerates the stagnant fluid under the separated shear layer and can lead the flow to reattach [15]. This forms an area of recirculating flow in the mean sense, whose upstream and downstream extents indicate the beginning and end of the laminar separation bubble.

Laminar Separation Bubbles also exist in simpler geometries that allow for easier study.

Flows over backward-facing steps [50, 51, 52], front-facing steps [53], blunt-edged splitters [22, 23, 24], splitters with fences [54], and flat plates with applied pressure gradients [11, 48, 55] show similar characteristics. In these geometries, sharp changes in geometry or applied pressure gradients cause the flow to separate. These flows typically exhibit the convective instability found in LSBs over airfoils, but depending on the strength of the reverse flow, they may exhibit a stationary or absolute instability [50, 56]. Momentum transfer within the separated shear layer leads it to reattach past separation and redevelop into a boundary layer. The control of location of separation as well as simplified geometries make these geometries well-suited to fundamental research while the insights gained from these separation bubbles can also be applied to the more-complicated airfoil geometries.

The locations of the time-averaged separation, transition, and reattachment help to indicate the impact of the separation bubble on the flow. Separation is indicated by the start of reversed flow at the airfoil's surface, and reattachment is where the mean reverse flow ends [2]. The point of transition can be defined as where the disturbances achieve the maximum growth rate [2], or where Reynolds stresses become substantial [57]. These points can be measured through direct velocity measurements within the LSB, such as hot-wires, Laser Doppler Velocimetry (LDV), and Particle Image Velocimetry. Hot-wires have the great advantage of excellent frequency response and spatial resolution for studying the growth of high-frequency disturbances [58]. Single-wire probes cannot distinguish between flow directions and are less accurate at the near-zero speeds like the recirculating region in the LSB, but are still useful for velocity profiles [59]. Split-film probes rectify this problem by resolving flow direction at the sacrifice of larger size and hence lower frequency response and have been used by Kiya and Sasaki in the separating-reattaching flow over a blunt-edged splitter to describe the direction of flow as it reattaches [24]. The requirement of physical probes being inserted within the flow raises the possibility of introducing disruptions to the mean flow [60]. LDA has also been used to make measurements within LSBs without causing physical disruptions, as well as resolving flow direction [61]. These measurements do require the presence of particles or seeding within the flow, which complicates LDA operation in field applications [62]. Both LDA and hot-wire measurements give point measurements of the flow, but can be conditionally averaged [24] or phase-locked [55] to gain velocity-field measurements. PIV has also been applied to LSB research to measure the flow field simultaneously [18, 44, 48, 63, 64]. Similar to LDV, PIV also requires seeding and illumination for imaging to capture the particles and measure the velocities [62]. Other qualitative measurements of separation include surface oil flows as well as tufts over the airfoils [9, 32]. By the direction and steadiness of the tufts, the state of the flow can be inferred, where unsteady motion indicates turbulence and tufts pointing upstream show flow separation. In oil flow visualizations, the reduced wall shear past separation creates

a region of undisturbed flow, while the high shear at reattachment shows a line with oil pushed upstream before the redeveloping flow [9]. These direct velocity measurements can be difficult to perform in the field.

The extents of the laminar separation bubble can be inferred from measurements other than direct velocity measurements . Separation, as measured with hot-wires [65], was found to correlate with the start of the plateau found in early experiments on airfoil pressure distributions. The end of this plateau and the beginning of the sharp pressure recovery at the end of the plateau was also related to sharp growth in turbulence intensity and broadband frequency spectra past this point. This sudden pressure recovery is used to mark mean transition. As the flow reattaches, the sharp pressure recovery returns to something closer to that expected for the inviscid pressure distribution. The end of the sharp pressure recovery is used to infer mean reattachment. These mean pressure measurements and methods are commonly used in investigations of separation bubbles [15, 38].

Development to transition within the separation bubble accompanies increases in the velocity fluctuations in the flow. Linear stability analysis uses the mean velocity profiles to predict the initial growth rates and spectra of disturbances [46, 63, 66]. This analysis predicts whether disturbances in the LSB are amplified convectively or if the flow is absolutely unstable and amplifies disturbances in place. The levels of growth rates and fluctuations within the flow have been used to indicate when the mean flow has transitioned [57]. The development of disturbances and the trajectory of the reattaching flow can be tracked using the Reynolds shear stresses and turbulent kinetic energy [52]. A Reynolds-stress threshold of 0.1% has been used to discern the location of transition [67]. These mean measurements match the mean structure described by Horton, with superimposed fluctuations that peak just upstream reattachment.

2.1.3 Time-varying Laminar Separation Bubble

Although the depiction of the time-averaged LSB as described by Horton is instructive, it does smear the features that evolve in time within the LSB. Measurements show that around the "point" of reattachment, there is a region where the flow is intermittently reversed [68]. Previous experiments found the earlier stages of Kelvin-Helmholtz disturbance development within the LSB bear a strong resemblance to that found within free shear layers [12]. Once the disturbances have reached sufficient amplitude, they begin to roll up into "cat's eye" vortices as illustrated in Fig. 2.3. In mild velocity gradients such as these free shear layers, disturbances are convectively amplified and travel at a rate around

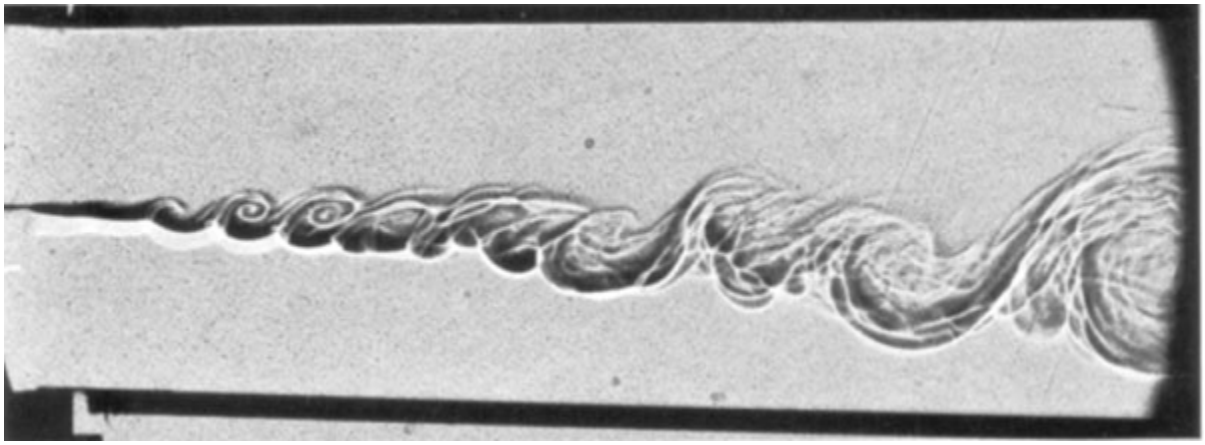

Figure 2.3: Shadowgraph of mixing layer between nitrogen and helium [3]. Disturbances are amplified into vortices.

the average of the velocity of the two fluid streams [47]. Winant and Browand [14] used dye flow visualizations to track the development of vortices within a free shear layer, and give form to the velocity fluctuations measured within their mixing layer. The evolution of disturbances into vortices has also been illustrated in other separating-reattaching flows over steps and splitters [24, 69, 70, 71, 72]. Visualizations of these vortices show their initial 2-D structure and eventual breakdown [70, 71]. Visualizations demonstrate that there is structure beneath the velocity fluctuations.

Recent experiments have found the evolution of vortical structures within laminar separation bubbles over airfoils as well as flat plates with applied pressure gradients[6, 13, 18, 44, 46, 55, 64, 73, 74, 75]. In these flows the separation region tends to be thin and hence more difficult to investigate [67]. The vortex dynamics are found to vary with geometry and any forcing, but tend to show an initial two-dimensional growth. An investigation with PIV [73] found vortices passing the airfoil's trailing edge to be responsible for tonal noise generated by a NACA 0018 airfoil. Extensive phase-averaged hot-wire investigations of a separation bubble over a flat plate with forced point disturbances were performed by Watmuff [55]. These measurements found that the disturbances follow the cat's-eye characteristic from free shear layers, and develop into vortex loops with a persistent identity past reattachment. Burgmann et al. [13, 64] used stereo scanning PIV to investigate the separation bubble over an SD 7003 airfoil. C-shaped vortices were found to evolve within the trailing edge of the separation bubble, with temporal variations in their strengths and shapes. The three-dimensional deformation of these vortices also leads to the development of streamwise-oriented screwdriver vortices. The dominant c-shaped vortices entrain fluid

into the separated shear layer as they develop. As the vortices evolve, they may also break down or burst once they have developed to sufficiently large scales. Scanning PIV was also used by Zhang et al. [44] to investigate the 3-D development of these vortices over an SD7003 airfoil at low Reynolds numbers. Their initial 2-D structure in the separated region remains present as the flow reattaches, but decreases in its spanwise coherence as the vortices stretch and tilt. Reducing the Reynolds number of the flow from 60,000 to 20,000 increases the size of the separation bubble and leads to dramatically larger vortices as well. These vortices are present just upstream of reattachment and discernable as well in the redeveloping flow. Marxen et al. [18] performed a paired DNS and experimental investigation on the LSB over a flat plate, with specific focus on vortex development and breakdown. Two-dimensional vortices develop from an absolute instability within this flow, but spanwise deformations also began to develop and led to vortex loops. This three-dimensionality was investigated by applying 3-D perturbations, with the same conclusion as Pauley [76] that three-dimensionality is significant in vortex breakdown. Two-dimensional simulations found that some of the vortices paired, although this was not replicated in 3-D simulations or experiments. Using a novel separation bubble flow visualization technique, Kirk [6] investigated the formation of vortices over a NACA 0018 airfoil. Using this visualization technique, he found that vortices were present towards reattachment in the separation bubble, and that under certain angles of attack they persisted for a sufficient period for them to interact along the stream and merge. These merges involved pairs as well as triplets in some cases before the structures underwent a three-dimensional breakdown. Vortices are common in these separation bubble flows, but have diverging characteristics towards breakdown.

Laminar separation bubbles may have their downstream extents vary in time, which is referred to as "bubble flapping" [70]. This lower-frequency variation is a common presence in separating flows over blunt geometries [22, 50, 70] as well as over airfoils [12, 74]. The cause of this temporal variation has also been attributed to several possible phenomena. Cherry et al. [70] investigated this low-frequency unsteadiness in the separated flow over a blunt-edged splitter. Velocity spectra measured along the separation bubble found two peaks in the spectra: a high-frequency peak early along the bubble and a lower-frequency component that dominated near reattachment. The low-frequency motion was found to scale with the bubble length, while the high-frequency component was related to shear-layer instabilities. Kiya and Sasaki [23] found a similar low-frequency unsteadiness on the flow over a blunt-edged splitter, and conjectured that it was due to a large-scale unsteadiness within the flow. They also found that the effect of the flapping was greatest near the point of initial separation. Flow visualizations from Kiya et al. and Cherry et al. illustrated that the variations in the position of the separated shear layer accompany the shedding of larger-

scale vortices. DNS of separation bubbles over flat plates also encountered the phenomenon of bubble flapping. A common practice in DNS studies is to force the initial disturbances within the boundary layer [77, 78]. After the initiation of the LSB and reattachment, the levels of disturbances may then be altered to determine the impact of the initial disturbance level on the flow development [46]. In DNS of a LSB over a NACA 0012 airfoil, Jones et al. found that when T-S waves are no longer forced, this leads to greater intermittency of fluctuations and frequencies amplified within the separation bubble. The LSB also sustains itself in the absence of the forced disturbances, however linear stability analysis suggested that there was not an absolute instability associated with the flow. Hain et al. [74] employed time-resolved PIV over an SD7003 airfoil at a Reynolds number of 66,000 and found bubble flapping under these conditions. They ascribed this flapping to temporal variations in the amplitude of the initial disturbances that arrive at the LSB. This could be due to the development of "wave packets" of Tollmien-Schlichting waves amplified in the attached boundary layer or the variation in incoming freestream disturbances. Depending on the level of reverse flow within the separation bubble [79], other investigations found that in addition to the high-frequency convective instability, there may also be a lower-frequency global instability. Hudy and Naguib [25] performed experiments on the flow over a backward-facing step using PIV. This experiment found that vorticity would accumulate and then be shed from the separation bubble. This was referred to as the "wake mode" of vortex shedding, which was found to be in contrast with the "shear layer mode" reported previously. Lee and Sung [50, 51] found both a convective and absolute instability within the flow over a backward-facing step with a turbulent boundary layer. These two modes contributed to the fluctuating flow behind the step, and create motion at the low and high-frequency time scales. The mechanism behind bubble flapping may thus vary depending on the conditions and geometry where the separation bubble is present.

2.2 Vortex Dynamics in Shear Flows

Coherent vortices play a fundamental role in the evolution of free shear layers [3, 4]. The early experiments of Winant and Browand [14] visualized coherent vortices in a free shear layer at lower and higher Reynolds numbers. They found that it was these coherent vortices that are the mechanism for large-scale momentum transfer in a mixing layer. Velocity measurements showed similar fluctuation profiles between these lower-Re flows and those at higher Reynolds numbers. As the shear layer developed, vortices emerged that would subsequently merge in pairs with twice the spacing of the original vortices. This merging process was found to entrain adjacent fluid from the lower- and higher-velocity streams

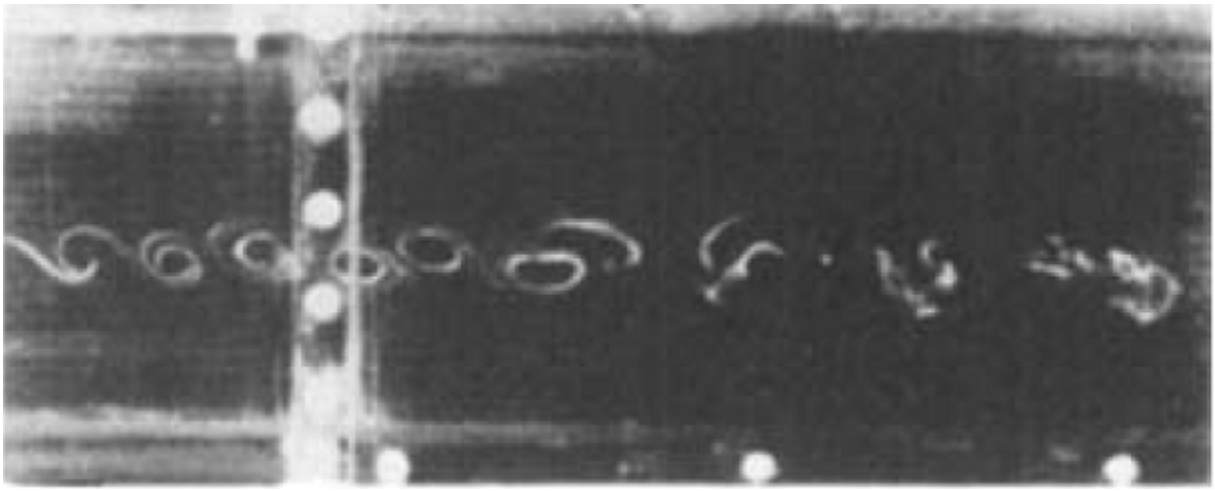

Figure 2.4: Dye visualization of vortex merging in a free shear layer [4]. Velocity fluctuations are introduced at the first subharmonic of the vortex formation frequency.

and result in increased mixing. The continued merging was attributed to the instability of a row of same-signed vortices to disturbances. Forcing disturbances of the most-amplified frequency also delayed vortex merging compared to the unforced case. Merging persisted until the vortices began to interact with the walls. This mixing follows the approximate wedge shape of the turbulent flow described in simple models of turbulent reattachment [80]. In the water tunnel experiment of Ho and Huang [4], the effect of forcing on vortex development and interaction was investigated. A sample image is shown in Fig. 2.4. When the forcing frequency is near the naturally-amplified frequency, then this is the frequency most apparent in the shear layer. At lower forcing frequencies, the amplified frequency returns to its naturally amplified frequency. Under no forcing, merging occurs randomly, but under different levels of forcing the merging can become more localized. Forcing near the most amplified frequency delays merging and reduces the spread of the shear layer across the flow. Lower subharmonics of this frequency promote merging of pairs as well as larger numbers of vortices depending on the frequency. Increased merging also accompanies greater cross-stream mixing. With the picture of turbulence as vortices of a range of scales interacting, vortex merging gives structure to the growth of mixing layers [81].

The merging of vortices follows a few stages from initial interaction to the completion of merging [82, 83]. Initially the vortices undergo a diffusive growth of their cores [82]. Without this viscous effect, the pairs of vortices would simply circle continually [84]. Experimental and numerical studies have found that this orbiting state persists until the size

of the vortex cores exceeds a critical proportion(≈ 0.3) of the vortex spacing [84]. Once the vortex cores attain the critical diameter in this viscous phase, it moves onto the convective stages. In this stage, the vortices approach each other, become deformed, and their vorticity fields become conjoined, and entrain much of the fluid around the two vortices [85]. Cerretelli further divides this stage into a second diffusive stage, where the two vortex cores achieve zero spacing [82]. In the final stage of vortex merging, the swirling deformed arms of the vortices disappear as the cores diffuse and achieve an axisymmetric vortex core. In the free shear layer, this process of merging repeats as the shear layer progresses and the vortices cascade to larger scales [3].

In shear flows near walls, the vortex dynamics are modified by the presence of that physical barrier. Roos and Kegelman investigated these structures downstream of a backward-facing step [86]. This investigation used a smoke-wire visualization just downstream of the step's edge to show the formation of two-dimensional vortices. These vortices intermittently merge before reattachment, but show a strong interaction with the wall that leads to breakdown. This merging is demonstrated by the shift in the spectral peaks of velocity measurements from that of the amplified disturbances to its subharmonic. Forcing was applied and found to make vortex formation more regular in the case of laminar separation, and reduce reattachment length in the case of a turbulent boundary layer. Merging did not persist past reattachment. Troutt et al. [87] used a rake of hot-wire probes to investigate the coherent vortical structures downstream of a backward-facing step with an initially turbulent boundary layer. These hot-wires were placed toward the edge of the mixing layer to predominately capture the effects of the large-scale structures. The peak in coherence across the span shifts from the initial Strouhal number of the amplified disturbances to its subharmonic as the flow progresses towards reattachment. This indicates the development of spanwise-oriented structures that merge before reattachment. As the vortices merge, spanwise correlation lengths also decrease, and continue to decrease past merging. Troutt at al. infer that the reduction of Reynolds stresses near reattachment is due to the cessation of merging. Reattachment inhibits vortex pairing and decreases spanwise coherence.

2.3 Surface Pressure Fluctuations for Flow Diagnostics

In applications where direct velocity measurements within a fluid are impractical, pressure measurements are commonly used to gain insight into the flow. Turbulent boundary layers are a common subject of investigation via surface pressure fluctuation measurements

in attached flow. Palumbo [88] used measurements of fluctuating surface pressure made on the turbulent boundary layer over an airplane's fuselage. Cross-correlations of filtered and windowed segments of signals allowed Palumbo to determine correlation lengths, convection velocities, and rates of decay of the different scales of structure. Embedded pressure sensors permit these flow measurements to be made in the challenging environment of a plane in flight. The lateral line organ on fish allows them to detect pressure gradients associated with structures in the flow [89, 90, 91]. Measurements of the neural response from goldfish's lateral line paired with PIV show that these natural sensors respond to flow structures such as vortices within the flow [89, 90]. These sensors allow fish to navigate in murky water [91], and discern wake patterns between objects of different size, similar to the structures produced by different sizes of fish [92]. These measurements at the boundaries of flows give insight into nearby flow structures.

Within separating and reattaching flows, measurements of surface pressure fluctuations have been related to the conditions of the flow. Similarities are found between several geometries with separating and reattaching flows: thin airfoils, forward-facing steps, backward-facing steps, fences, and sharp-edged diffusers [93]. Within these flows, the pressure fluctuations tended to increase to a maximum upstream of reattachment. Investigations over blunt-edged splitters were performed by Cherry et al. [70] and Kiya and Sasaki [22, 23, 24] using measurements of surface pressure and velocity fluctuations to investigate the irregular aspects of the flow. The spectra of the pressure fluctuations capture velocity fluctuations associated with vortex formation as well as shear layer flapping motions. Flow visualizations over this blunt-edged splitter geometry show the initial formation of laminar vortical structures that later become turbulent [23, 70]. When Cherry et al. combined their flow visualization with synchronized pressure fluctuation records, they found that the passage of vortices over their pressure taps corresponded to local minima in the pressure signals. These structures and the pressure signals are pseudoperiodic, and both vary through cycles of greater and smaller activity. Kiya and Sasaki used strong peaks in the pressure signals to conditionally average split-film probe velocity measurements. A low-pressure excursion was related to the presence of a vortical structure over the pressure sensor, with maxima between vortices. Cross-correlations between surface pressure and streamwise velocity fluctuations show that below the mean height of the vortex cores, there is a positive correlation between them, and a negative correlation above the center. For vertical fluctuations, there is an opposite trend with weaker correlation. This is due to the passage of the vortices inducing positive and negative velocity fluctuations above and below its cores respectively. The growth and convective velocities of disturbances were related to measurements past a backward-facing step in a PIV and pressure fluctuation study by Hudy, Naguib and Humphreys [25]. This found a stationary accumulation of vorticity

that was then shed. The cross-correlation showed the change of the average convection rates of the vortices as they were shed. The pressure fluctuations at the surface are shown to reflect the adjacent flow in these flows even with separation between the walls and the phenomena.

Surface pressure fluctuations have been measured on flows over airfoils to investigate these fluctuations in more complex geometries. Paterson et al. [94] used embedded microphones to investigate noise generated by airfoils. These sensors could measure whether the flow was laminar or turbulent from the spectra of the pressure signals, and relate the tonal noise to vortex shedding from the airfoil. Further experiments were performed by Yarusevych to investigate stalled and un-stalled flow over a NACA 0025 airfoil. Both the distance from the surface and intensity of the velocity fluctuations gave insight into whether the flow reattached past separation [1, 20]. The spectra of the surface pressure fluctuations indicated the same fundamental frequency of shear layer growth as hot-wire measurements, as well as shifts to subharmonics that are associated with vortex merging [95]. Measurements of surface pressure fluctuations have been extended to track amplification, maximum fluctuating surface pressure, and mean convective velocities of disturbances [20, 38]. These investigations demonstrate the ability of surface pressure fluctuations to track the mean development and convection of disturbances. While the average effect of vorticess is shown by mean statistics on pressure fluctuations, the effect of individual vortices has yet to be explored. Investigation of the intermittency and variability of vortex activity would give further insight into laminar separation bubble dynamics and develop a framework for understanding the effects of control strategies.

Chapter 3

Experimental Method

Laminar separation bubble dynamics over an airfoil were experimentally investigated in a wind tunnel facility. A combination of Reynolds number and angles of attack were selected to investigate the LSB over a range of lengths and positions over the airfoil. The selection of Reynolds number must provide a sufficiently high dynamic pressure to reduce experimental uncertainty while being sufficiently low to facilitate smoke-wire visualizations. This facility and the airfoil model have previously been characterized by Gerakopulos [96], Boutilier [5], and Kirk [6]. As this configuration is well-developed and understood, the previous experiments give a strong foundation to build on. The experimental facility, model, and techniques are outlined below.

3.1 Experimental Setup

3.1.1 Wind Tunnel Facility

Experiments were performed in the University of Waterloo Adaptive-Wall Wind Tunnel. This facility was commissioned in the 1960s, but has undergone a series of upgrades while maintaining the same basic layout. Affectionately called "Big Blue", it is an open-return, suction-type wind tunnel, and is presented in Fig. 3.1. Speed control for the original DC fan motor is provided by a variac that controls a DC generator. In the 1990s, the test section was upgraded with adaptive walls. The test section is nominally 0.6m wide by 0.9m tall and 6m long, and the upper and lower walls of the test section can be moved to reduce the effect of the boundaries on flow development. Inflatable seals along the edges of these walls seal

the seam between the movable and solid walls. The roof and floor are each equipped with 48 jacks to adjust the profile of the walls. These are accompanied by pressure taps to record the pressures for wall adaptation strategies. A mechanical Scanivalve system connects the pressure taps to Lucas Schaevitz P3061-2WD pressure transducers for measurement. The test section is fed from a 9:1 rectangular contraction with filleted corners. Upstream of the settling chamber and contraction there are four screens and a honeycomb for flow conditioning. At the conditions investigated, the turbulence intensity is less than 0.2%. Flow uniformity at the location of the model is $\pm 0.6\%$. A correlation between the pressure drop over the contraction and the flow velocity is used to measure flow velocity. This pressure drop is measured with an inclined manometer with a resolution of 1.25 Pa, for an uncertainty in flow velocity of 2%.

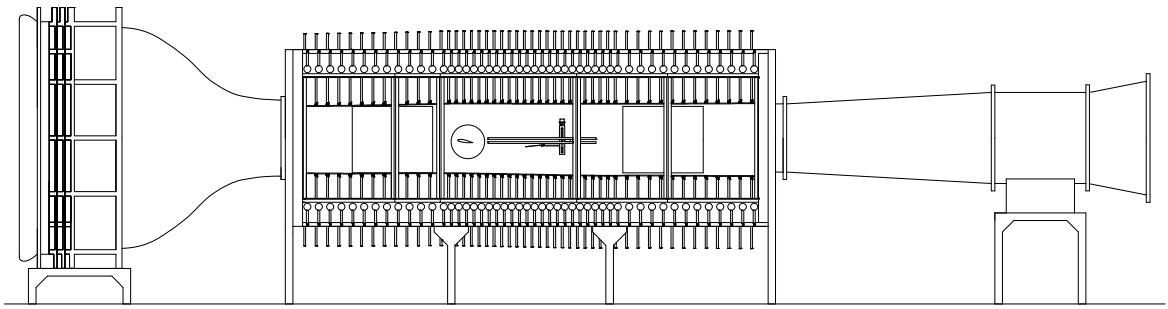

Figure 3.1: Schematic of the University of Waterloo Adaptive-Wall Wind Tunnel, image from Boutilier [5].

For the experiments reported here, the walls were set to a geometrically straight configuration. Investigations by Boutilier [5] found that wall adaptation predominantly affected wake development rather than flow over the model. Test section buoyancy is also not of concern since force measurements are not perfomed in this instance.

3.1.2 Airfoil Test Model

The airfoil model used in these experiments is an aluminum NACA 0018 airfoil model, depicted in Fig. 7. This model was designed and built by Ryan Gerakopulos and the flow around it has been studied by Gerakopulos [97] as well as Boutilier [5] and Kirk [6]. The model has a chord of 200 mm and a span of 600 mm. This airfoil spans the test section of the wind tunnel, with end caps to seal the ends against the side of the wind tunnel. The model is equipped with pressure taps and embedded microphones to measure mean and

fluctuating pressures. The airfoil was anodized and polished using the techniques described by Gerakopulos [97]. For the angles investigated, the solid blockage based on frontal area is less than 5%.

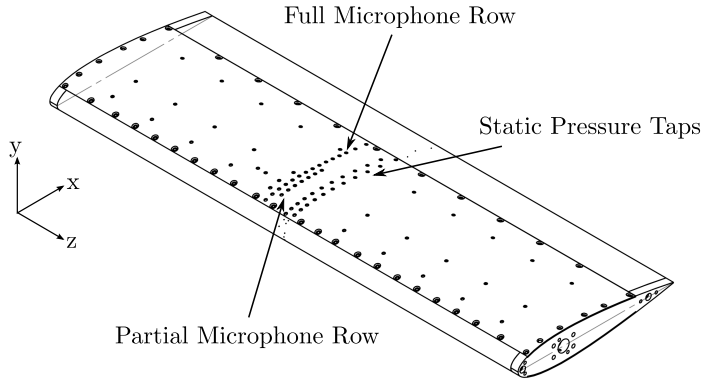

Figure 3.2: Airfoil model with chordwise static pressure taps and embedded microphones.

3.2 Measurement Techniques

3.2.1 Pressure Measurements

An array of pressure taps allow for mean as well as fluctuating pressure measurements. Ninety-five 0.4mm pressure taps were drilled in the airfoil for static pressure measurements. Sixty-five taps were located in a chord-wise plane near the airfoil's centre to measure the pressure profile around the wing. The remaining thirty pressure taps were distributed across the span of the airfoil to verify spanwise flow uniformity. These pressure taps were connected to a mechanical Scanivalve multiplexer via 0.8mm diameter tubing. Pressures were measured relative to a reference pressure tap on the test section wall. The outputs from a pair of Lucas Schaevitz PW3061-2WD pressure transducers were recorded with a National Instruments PCI 6259 data acquisition card. The pressure transducers were calibrated with a Druck DPI 610 pressure calibratos and used a linear fit, for an uncertainty of 1.6% of dynamic pressure. At the start of each set of measurements, the zero-pressure voltage offset was recorded and subtracted from the subsequent measurements. A LabVIEW VI coordinated the measurements with the operation of the Scanivalve system to record all of the pressure taps.

Fluctuating pressure measurements were measured using embedded microphones. The system of microphones and pre-amplifiers was embedded within the airfoil. Twenty-five Panasonic WM-62C back electret microphones were embedded beneath the surface of the airfoil under 0.8mm pressure taps. These microphones were individually calibrated against a reference microphone in an anechoic chamber, and found to have a linear response up to 2000 Hz. Twenty-two of the microphones were oriented along the span, while the remaining three were aligned across the span. The chord-wise microphones were staggered in two rows along the skin of the airfoil, with one partial row of seven and the other row of fifteen covering the full length from $x/c = 0.08$ to $x/c = 0.73$. The partial row increased the spatial resolution between $x/c = 0.15$ and $x/c = 0.41$. Signals from the amplifiers were carried from the airfoil through 1m Belden coaxial cables and further to the data acquisition with 5m Belden coaxial cables. Up to 8 voltages were recorded simultaneously using a National Instruments PCI-4472 data acquisition card. A linear relationship between voltage and pressure was applied from the individual calibrations. Measurements were conducted using a program created in LabVIEW.

3.3 Flow Visualization

Flow visualizations were performed using a smoke-wire technique. These visualizations were performed for the flow around the model, a vertical plane of the separation bubble, and a horizontal plane. A smoke fluid of 30% glycerine and 70% distilled water was applied to the wire using a cotton swab. Opening the door on the side of the wind tunnel is necessary to apply the smoke solution to the smoke-wire, and may disrupt the flow over the airfoil. Following the recommendations of Boutilier [5], after the door was opened the flow was allowed to recover for 30 seconds before images were captured. The wires were nichrome, 0.1mm in diameter. A variac was used to control the AC voltage used for electric heating of the wire. Illumination was provided by a laser light sheet to illuminate a plane of the smoke. The frequency of the Photonics Industries DM20-527 Nd:YLF laser was matched to the speed of image acquisition to provide a single image. Each visualization required its own setup, with the individual configurations shown in Figs. 3.3-3.5. The laser was mounted outside of the test section on a motorized vertical traverse. A mirror was mounted on the wind tunnel traverse's sting, along with the light sheet optics on a pivot. This setup allowed the light sheet to be precisely adjusted depending on the lighting required by the different visualizations performed. A Nikon D300 digital SLR camera was used for high-resolution still images. It was controlled remotely using Nikon's Camera Control Pro software, and could record at up to 8 frames per second at full resolution. High-speed

images were captured with a Photron Fastcam SA4 at up to 1024x768 pixels and 5000 or 7500 fps. The camera was controlled through Photron FASTCAM Viewer software, with the camera frequency synchronized with the laser. Closeup images were taken with a Nikkor 105mm macro lens while images with a larger field of view used a Nikkor 18-70mm zoom lens. The specific details of the different setups are described below.

Upstream flow visualizations were performed with the vertical wire 20 cm upstream of the model, as in Fig. 3.3. The smoke wire was attached to the roof and floor of the test section. A spring and weight provided tension at the lower mount as the wire expanded with heating. The laser light sheet was aligned with the wire with the optics 1.5m downstream of the model. Full laser illumination was used with the voltage at the hot-wire set for the smoke to last for half a second. The camera was set up within the laser curtains and aligned past the airfoil's trailing edge. Images were captured with the laser curtains drawn and the lab lights off. These images were post-processed using Adobe Photoshop and GIMP.

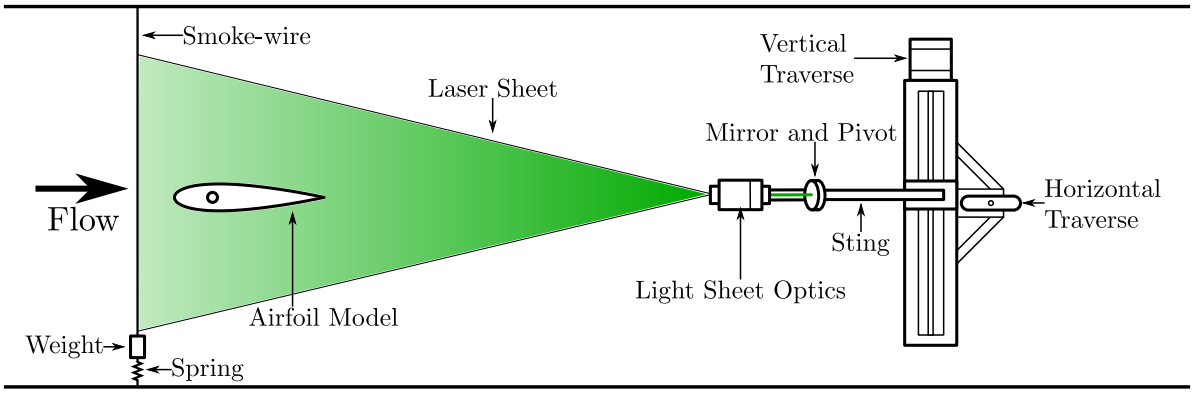

Figure 3.3: Schematic of flow visualization for flow around the airfoil

For separation bubble visualizations, the wire was placed along the span of the wing within the separation bubble, as indicated in Fig. 3.4. The position was set based on the location of the separation bubble from pressure measurements over the airfoil. The wire was attached to the airfoil with two insulated aluminum brackets and the wire height was adjusted using electrical tape shims. The laser illuminated a vertical plane over the airfoil. The high-speed camera was focused on the plane of the laser, and an image of a scale was captured. The height of the smoke-wire was gradually increased until it was on the edge of the shear layer, as shown in the high-speed video recordings. These visualizations were performed simultaneously with microphone recordings sampled at 40 kHz. Five

data acquisition channels were connected to microphones in the relevant range. Three of the channels from the NI PCI-4472 recorded the laser sync, the camera shutter, and the recording trigger signal to synchronize the images with the pressure measurements.

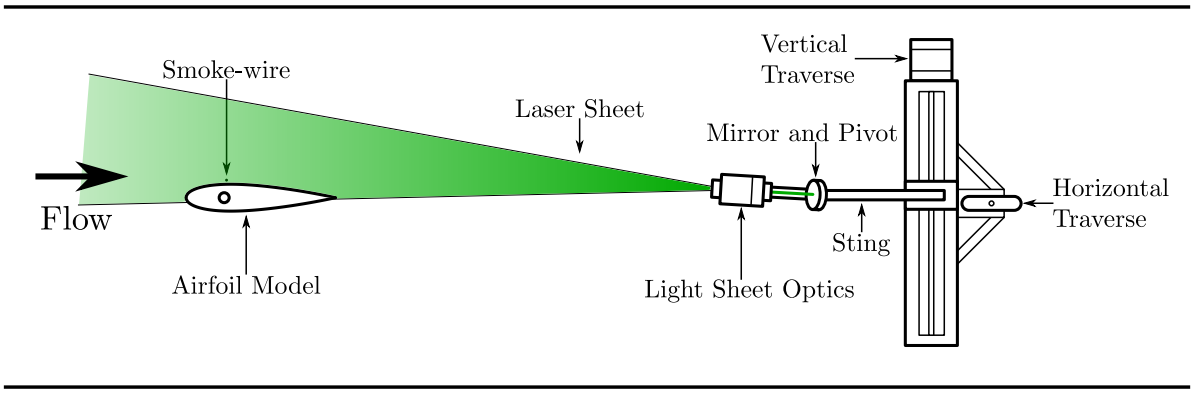

Figure 3.4: Schematic of setup for vertical separation bubble visualization.

In span-wise visualizations, the laser was aligned with the wire along the span of the airfoil, as shown in Fig. 3.5. The same wire heights and positions as the vertical LSB visualizations were used. The angle and height of the light sheet over the airfoil surface was adjusted to optimize illumination of the smoke. The cameras were mounted on a tripod to the side of the test section. A mirror was mounted at an angle to the roof of the test section to let the camera view the top of the airfoil. An image of a ruled reference over the airfoil was captured for the scale. A picture with the laser illuminating the airfoil surface showed the locations of the microphone ports. The same method for image and signal synchronization was used as in the vertical visualization.

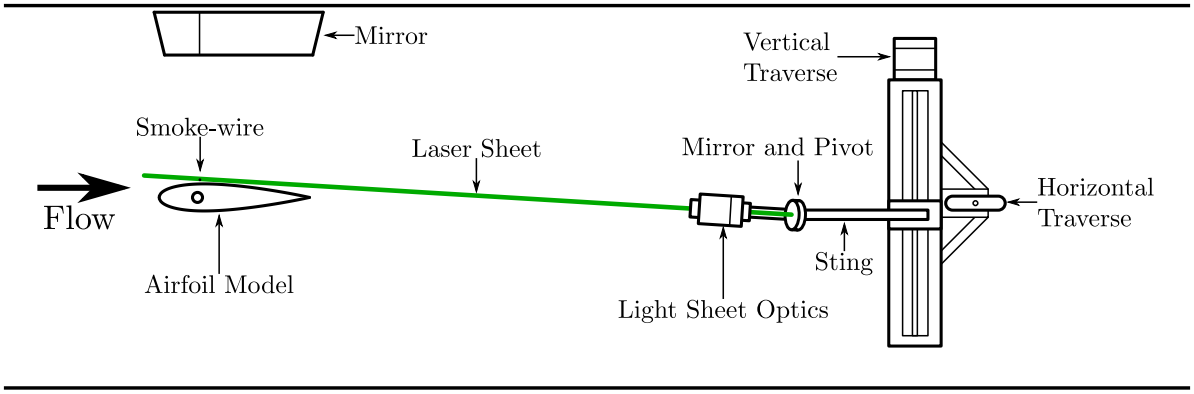

Figure 3.5: Schematic of setup for horizontal separation bubble visualization.

Chapter 4

Flow Physics

In this chapter, the flow structures and the related pressure fluctuations are characterized and linked. In Section 4.1, the mean and instantaneous structure of the LSB within the flow is presented. The visualized flow is compared with the measured mean pressure measurements. Section 4.2 reports on the development of pressure fluctuations along the airfoil. The link between pressure fluctuations and flow structures is developed and substantiated. The effect of vortex merging is explored in Section 4.3. The impact of merging on pressure signals is investigated, and the factors that impact merging are compared using a simplified model. The relationship between flow structures and pressure signals is used in Section 4.4 to track vortices based on measured pressure signals.

4.1 LSB Structure

All the results presented in this chapter were obtained at an angle of attack of 8° and $Re_c = 100{,}000$. A flow visualization image in Fig. 4.1 depicts flow development over the airfoil at the conditions investigated with the smoke-wire arranged as in Fig. 3.3. The streaklines introduced upstream show the flow generally following the shape of the airfoil. These streaklines become more spread out as the flow slows towards the stagnation point at the airfoil's leading edge. Past the leading edge, the streaklines over the airfoil's suction side become more compressed as the flow accelerates over the airfoil. Downstream of the airfoil, a relatively narrow wake is formed, indicating that the airfoil operates at the pre-stall condition expected for this angle of attack and Reynolds number [38]. Nevertheless, a closer inspection of the results over the suction side suggests that the streaklines are notably displaced from the airfoil surface downstream of $x/c = 0.15$, and the streakline nearest to

the suction surface shows the development of unsteadiness at and beyond $x/c = 0.4$. The emergence of the unsteadiness suggests that there is activity within the near-wall flow that is not visualized with the streaklines.

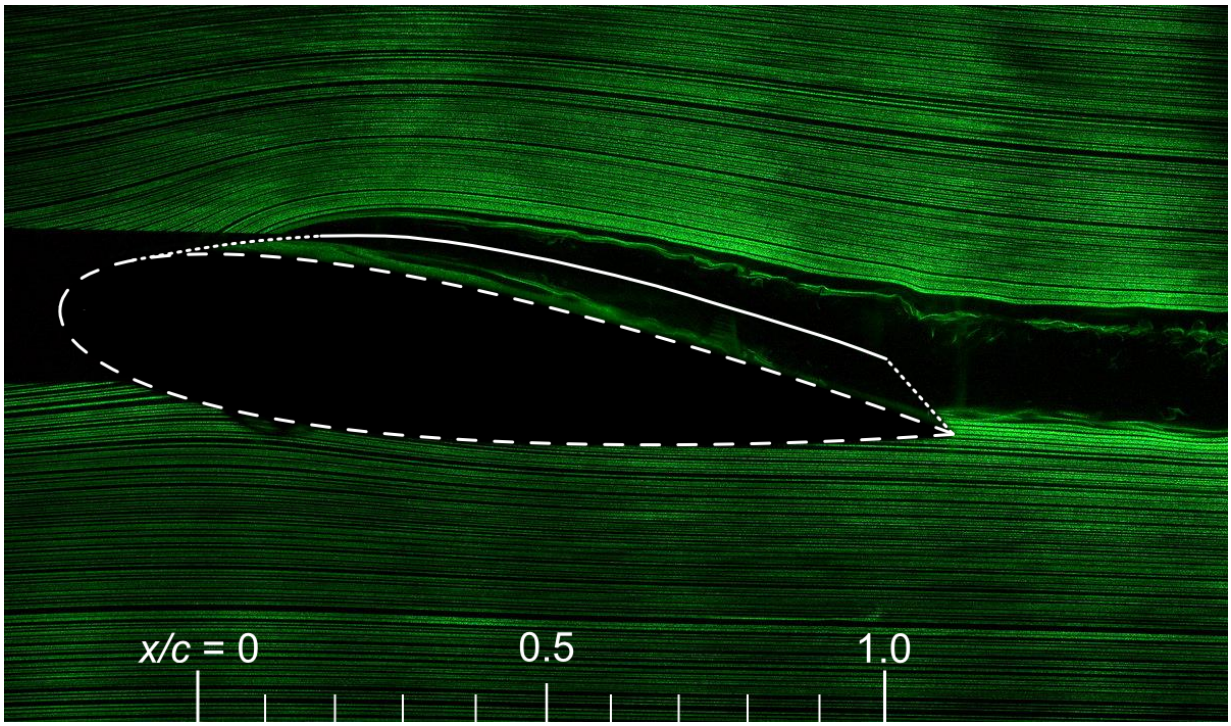

Figure 4.1: Flow visualization around the airfoil. Flow is from left to right. The outline of the airfoil at the wind tunnel wall is the dashed line, the surface of the airfoil at the plane of the smoke is the solid line, and the dotted lines show the visual foreshortening of the airfoil.

To investigate the unsteadiness near the airfoil surface, the smoke wire was placed inside the region of interest as shown in Fig. 3.4. The resulting flow visualization is shown in Fig. 4.2. The smoke introduced from the hot-wire in this image marks the fluid in the separation bubble, and reveals the development of flow structures within the separation bubble. The image shows that the smoke is being carried primarily in the streamwise direction, but a portion of the smoke is carried upstream from the wire. The smoke being carried upstream identifies the presence and the upstream extent of the reverse flow region near the wall. Downstream of the smoke wire, disturbances develop within the separated shear layer and form vortical structures. Further downstream, the structures lose coherence and break down to smaller scales indicative of transition to turbulence. As these turbulent

structures break down, the smoke mixes with the adjacent fluid. This depiction of local flow separation followed by transition and increased mixing follows the trends expected for an LSB [2].

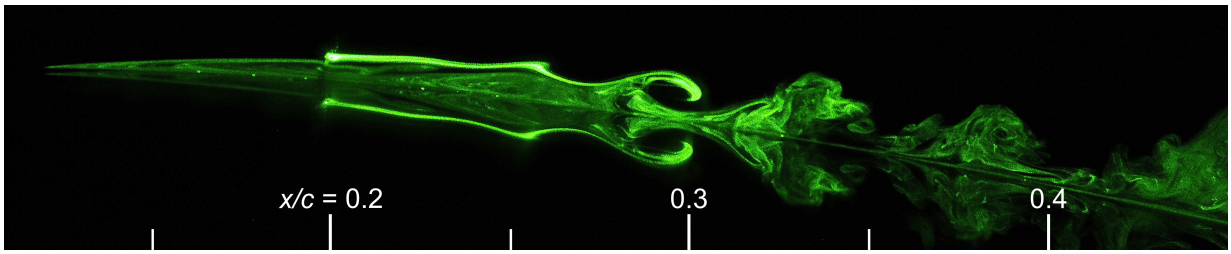

Figure 4.2: Flow visualization within laminar separation bubble. The wire is located at $x/c = 0.2$ and the free stream is from left to right. Note that a reflection of the smoke is visible in the airfoil surface.

The formation of an LSB on the suction side is confirmed by the mean surface pressure distribution shown in Fig. 4.3. This figure shows low pressure on the suction side as the flow accelerates over the airfoil surface, and a stagnation point on the airfoil's pressure side. Past the suction peak there is a pressure plateau extending from $x/c = 0.13$ to $x/c = 0.28$, which is indicative of the near-stagnant flow within the laminar separation bubble [11]. The pressure plateau is followed by a rapid pressure recovery caused by an increase in momentum transfer, and this recovery is commonly used to identify the location of transition to turbulence. The mean separation, transition, and reattachment points were estimated using the methodology described in Ref. [38] and are labeled in Fig. 4.3 as S, T, and R, respectively.

To facilitate a comparison of the classical, time-averaged picture of the laminar separation bubble [2] and current flow visualization results, an average of the high-speed image sequences was computed. The result is presented in Fig. 4.4. The locations of mean separation, transition, and reattachment identified from the pressure distribution are indicated in the image. The smoke-wire was placed at the edge of the reverse-flow region, so the smoke is entrained upstream as well as downstream. The upstream extent of the time-averaged bubble agrees with the estimated separation location from the pressure distribution. Moreover, a more precise location of boundary layer separation could be achieved by extending the dividing streamline visualized by the edge of the smoke to the airfoil surface. The smoke that is carried downstream forms a steady streakline up to $x/c = 0.25$. The minimal smoke diffusion downstream of the smoke-wire indicates that the initial flow development is free of significant disturbances. However, as shear layer disturbances grow, the diffusion of the smoke increases with increasing downstream

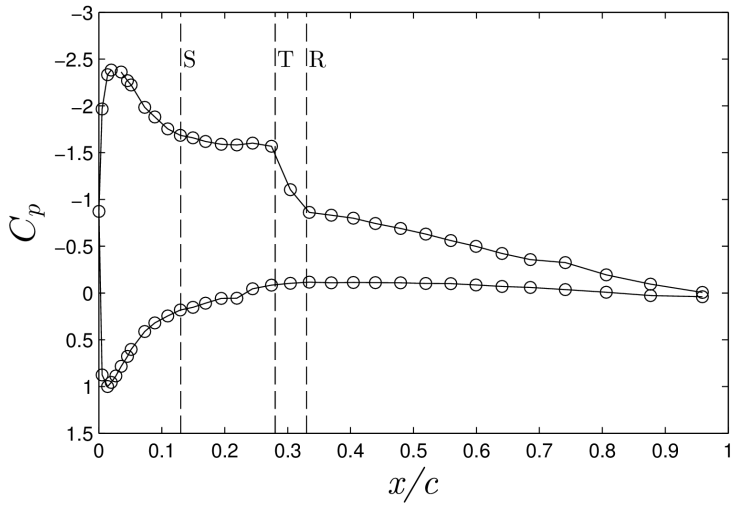

Figure 4.3: Mean surface pressure distribution on the airfoil. Estimated locations of mean separation (S), transition (T), and reattachment (R) are indicated by the corresponding letters, with an uncertainty of half of the pressure tap spacing. Note that the ordinate axis is reversed.

distance, with the mean streakline no longer identifiable in the vicinity of the estimated transition location. Following transition, the dispersed smoke moves towards the airfoil surface upstream of the estimated reattachment location and continues to disperse past reattachment. On the whole, the overall time-averaged outline of the bubble agrees with that reported in previous studies. [2, 11, 74]

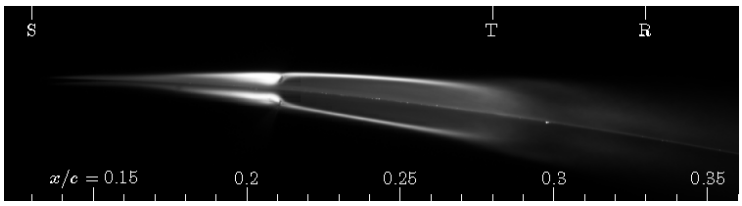

Figure 4.4: Time-averaged visualization of a separation bubble, with flow from left to right.

A sequence of high-speed flow visualization images in Fig. 4.5 illustrates the evolution of disturbances in the separated shear layer. In this sequence, the streakline introduced by the smoke-wire in the fore portion of the separation bubble shows disturbances developing as they travel with the flow. The streakline initially shows no oscillations, indicative of laminar flow development. However, small amplitude oscillations become visible at $x/c = 0.23$ and

their amplitude grows as disturbances propagate downstream. This leads to shear layer roll-up at approximately $x/c = 0.26$. The images show that the roll-up location varies from cycle to cycle, and so does the spacing between the subsequent vortices. The dotted lines in Fig. 4.5, that follow the positions of the vortices, illustrate the similar downstream velocities of these structures. As the vortices pass the mean transition location, notable unsteadiness of smoke filaments develops in the vortex cores. The structures begin to break down at approximately $x/c = 0.30$, with the location of vortex breakdown varying from cycle to cycle. These visualization sequences illustrate the periodic, time-varying development of structures that lead to transition within the separation bubble.

Since previous results indicate that transition is a strongly three-dimensional phenomenon [98, 78], the structures that develop are shown in a spanwise visualization in Fig. 4.6, using the layout shown in Fig. 3.5. In this view, the disturbances initially show a two-dimensional characteristic but become increasingly three-dimensional along the airfoil. Up to $x/c = 0.26$, the disturbances are two-dimensional, but past this point roll-up does not progress uniformly across the span. The chord-wise positions of the cores of the vortices locally become slightly skewed across the span around $x/c = 0.3$, and may even be overtaken by the upstream vortices, as in Fig. 4.6c) at $x/c = 0.25$. As the vortices break down towards $x/c = 0.34$, the chordwise position of their cores shows further variation across the span and the smoke diffuses into smaller features. Nevertheless, there is still evidence of the initial larger-scale spanwise structures up to $x/c = 0.4$, where the smoke creates bands across the airfoil's span. This shows that while the flow is initially two-dimensional, there are limitations to how far across the span local measurements are representative of the flow. Hence, for the purposes of this analysis, chord-wise measurements of the local fluctuating quantities are assumed to only capture the flow conditions in the wall-normal plane along the span where they are performed.

4.2 Pressure Fluctuations

The development of disturbances within the flow can be quantified by surface pressure signals from the embedded microphones shown in Fig. 4.7. Gerakopulos and Yarusevych [20] performed a direct comparison of surface pressure fluctuations and separated shear layer velocity measurements to relate the disturbances in the flow to the pressure fluctuations measured at the surface. The surface pressure fluctuations were shown to reflect the development of shear layer disturbances in the later part of the initial exponential amplification region, once disturbances begin to produce measurable surface pressure fluctuations. In Fig. 4.7 at $x/c = 0.21$, the amplitude of fluctuations is minimal and the pressure signal

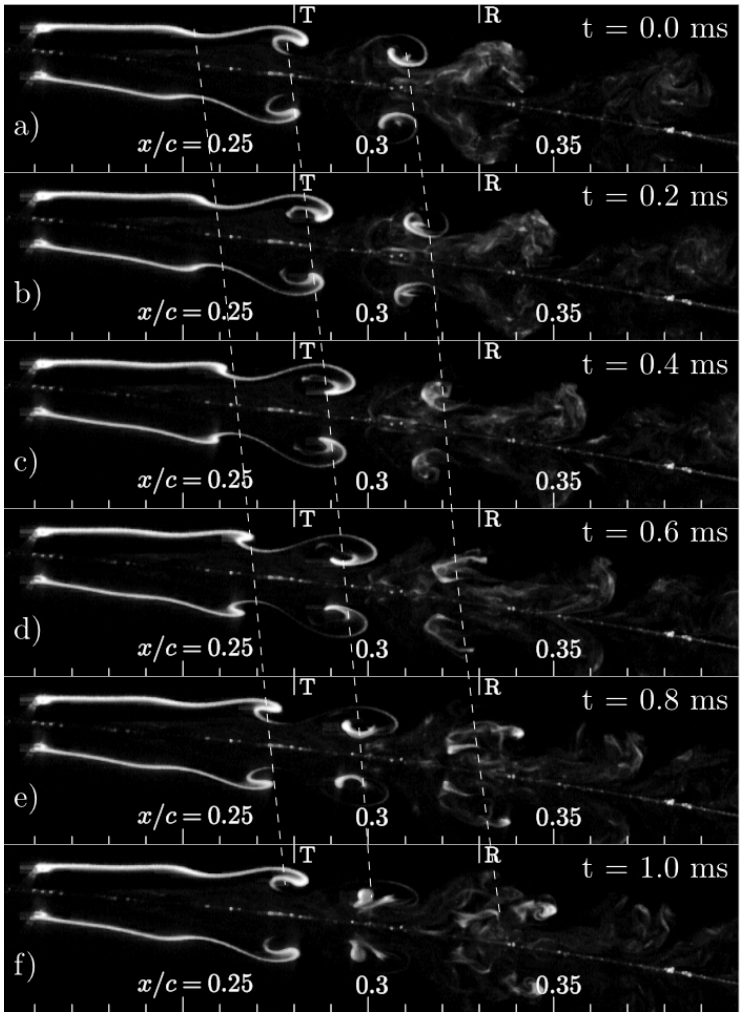

Figure 4.5: Sequence of separation bubble visualizations. The consecutive images are separated by 0.2 ms. The dotted lines connect the same vortices in the images, with the slope of the lines being indicative of convective speeds of the structures.

is nearly steady. Periodic pressure fluctuations begin to emerge at $x/c = 0.23$ and become prominent at $x/c = 0.26$, where the vortices begin to roll up (Fig. 4.5). At $x/c = 0.28$, the pressure fluctuations continue to grow, but a lower-frequency component emerges in the signal. Past $x/c = 0.3$, higher-frequency activity also emerges intermittently, and the overall periodicity of the signal diminishes. From Fig. 4.7, it can be seen that this corresponds to the region where structures begin to break down. In brief, the comparison between the

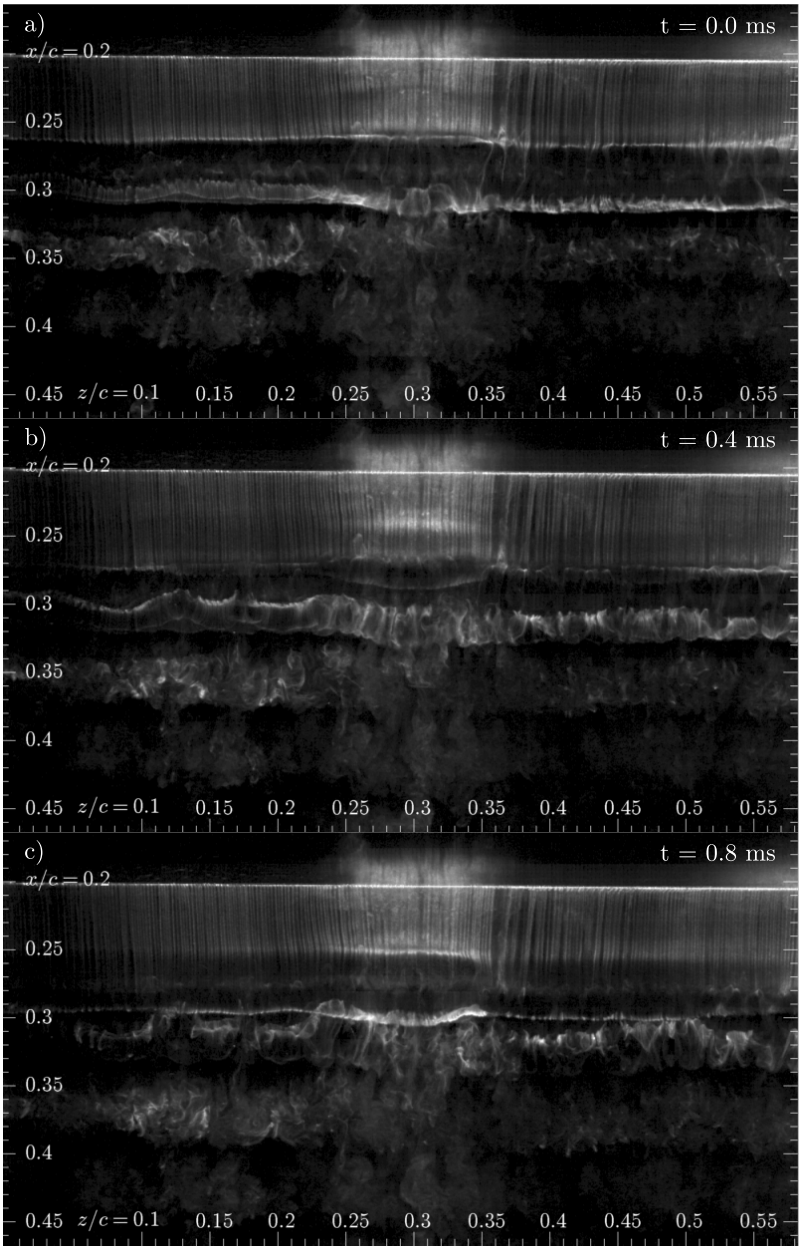

Figure 4.6: Sequence of top view bubble visualizations with flow from top to bottom. Time interval between images is 0.4 ms.

pressure signals and visualizations show that the microphone signals reflect the changes in amplitude and periodicity of disturbances in the flow.

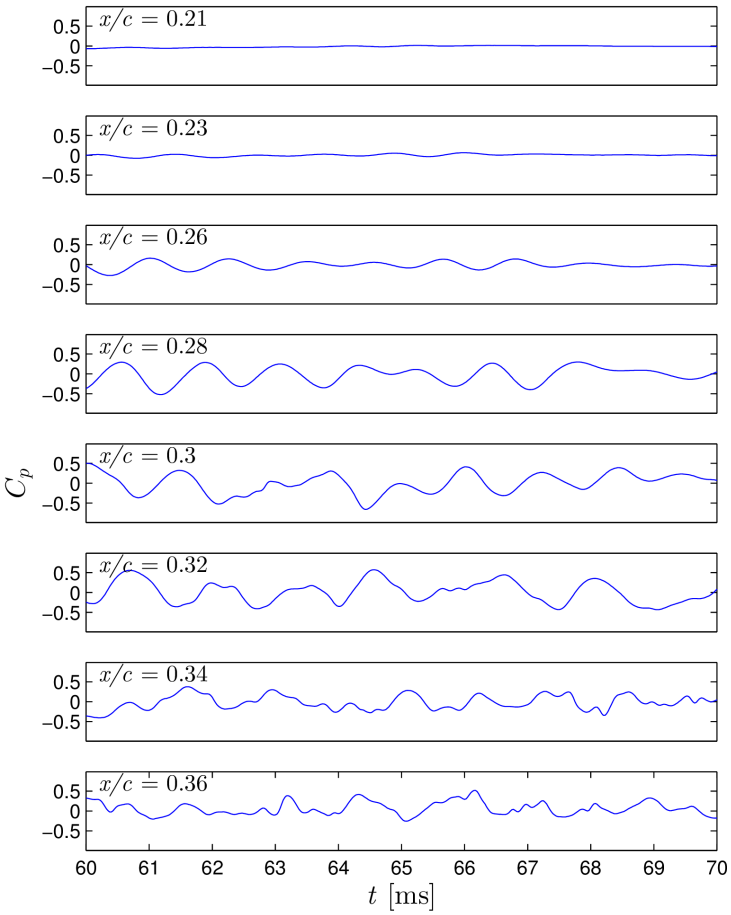

Figure 4.7: Development of surface pressure fluctuations along the separation bubble.

The streamwise growth in amplitude of surface pressure fluctuations is depicted in Fig. 4.8. The growth and then decay of fluctuations along the airfoil chord is illustrated in this figure. The amplitude growth is nearly exponential for $0.23 \leq x/c \leq 0.28$, as predicted by linear stability theory. Past roll-up and near mean transition at $x/c = 0.28$, the growth of disturbance amplitude is reduced, which is characteristic of the later stages of transition [93]. The peak in disturbance amplitude is reached at $x/c = 0.3$, upstream of mean reattachment, and the amplitude gradually decreases downstream. The streamwise location of the peak amplitude of pressure fluctuations corresponds to the location beyond

which vortex breakdown is observed in Fig. 4.8. Again, the development of the magnitude of pressure fluctuations reflects the flow structures developing and then decaying along the airfoil.

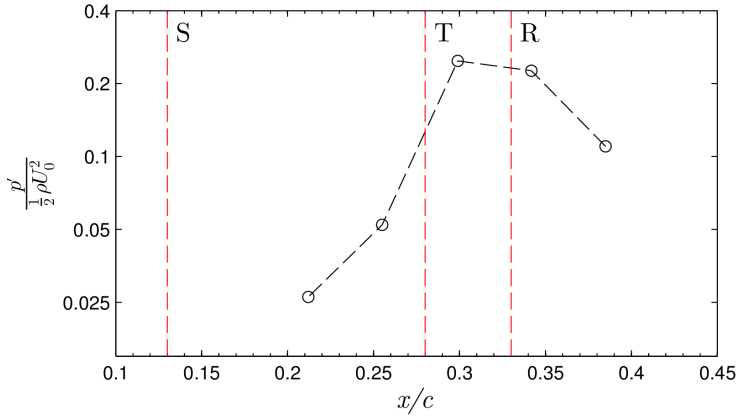

Figure 4.8: Root-mean-square of surface pressure fluctuations along the separation bubble. The locations of mean separation, transition, and reattachment estimated from mean surface pressure distribution are shown by S, T, and R, respectively.

To investigate periodicity in the surface pressure fluctuations, the frequency content of the signals along the separation bubble was analyzed via the power spectra shown in Fig. 4.9. In these spectra, a band of frequencies grows and then spreads as the flow develops along the chord. At $x/c = 0.21$, a frequency band of amplified disturbances can be identified centered at $f_0 = 900Hz$. The energy associated with the band of unstable frequencies grows as disturbances develop downstream to $x/c = 0.3$, which is also accompanied by the appearance of a first harmonic in the spectrum. Within $0.3 \leq x/c \leq 0.34$, the energy content associated with the amplified wave packet broadens over a wider range of frequencies, marking the last stages of transition. Comparing these results with the flow visualization images in Fig. 4.5, it can be inferred that the frequency of the dominant pressure fluctuations is associated with the periodic shedding of shear layer vortices. The broadening of the energy content associated with these structures occurs in the same region where vortex break down is identified in the visualization images (see e.g. $0.3 \leq x/c \leq 0.34$ in Fig. 4.5). Downstream of $x/c = 0.34$, broad spectra are observed in Fig. 4.9, with minor peaks persisting in the frequency range of the most amplified disturbances. These peaks reflect the acoustic resonances of the test section across the 0.6 m and 0.9 m directions.

The results discussed so far show that pressure fluctuations reflect the development of disturbances and the associated coherent structures in the separated shear layer. To

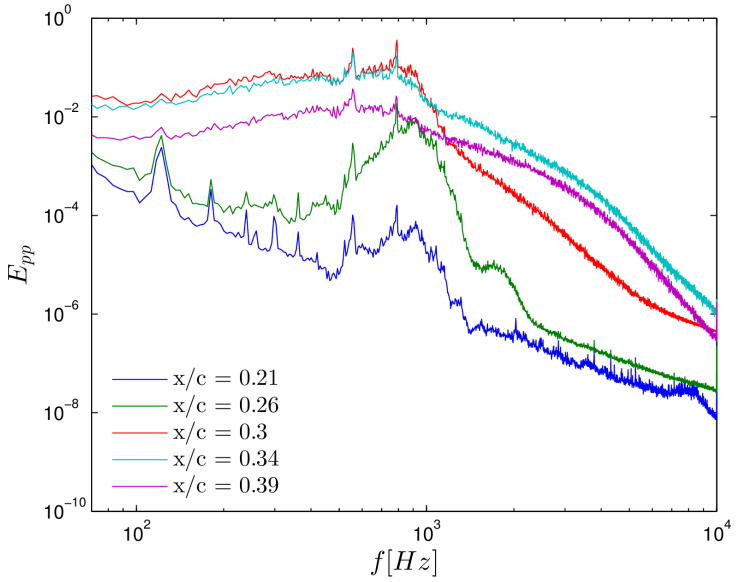

Figure 4.9: Spectra of surface pressure fluctuations along the airfoil.

be able to gain further insight into the development of shear layer vortices in the aft portion of the separation bubble, it is of interest to establish a direct correlation between the passage of these structures and the pressure fluctuations they induce on the surface. Figure 4.10 presents a sequence of flow visualization images synchronized with the pressure signal at a microphone port marked with a red dot. A vortex V is captured passing over the microphone port. As the vortex approaches the microphone port (Fig. 4.10a), the flow impinging on the surface leads to an increase in surface pressure to a maximum in the pressure signal. When the vortex is above the microphone port (Fig. 4.10b), a pressure minimum is attained in the signal. The pressure begins to recover as the vortex continues to move downstream (Fig. 4.10c) and subsequent vortices straddle the microphone. Thus, a train of shear layer vortices induces periodic surface pressure fluctuations at a given microphone location, as seen in Fig. 4.7.

It is instructive to substantiate the link between vortices and pressure minima from the comparison of flow visualizations and pressure signals with a simplified model. First, an inviscid model of the passage of a single vortex over a surface is constructed using a mirror pair of opposite-signed irrotational vortices. The simulated pressure signature is obtained by calculating pressure variation along the dividing streamline using Bernoulli's equation, and the results are shown in Fig. 4.11. For this model, the distance between the vortex and the wall is estimated from flow visualizations, and the strength of the vortices is selected

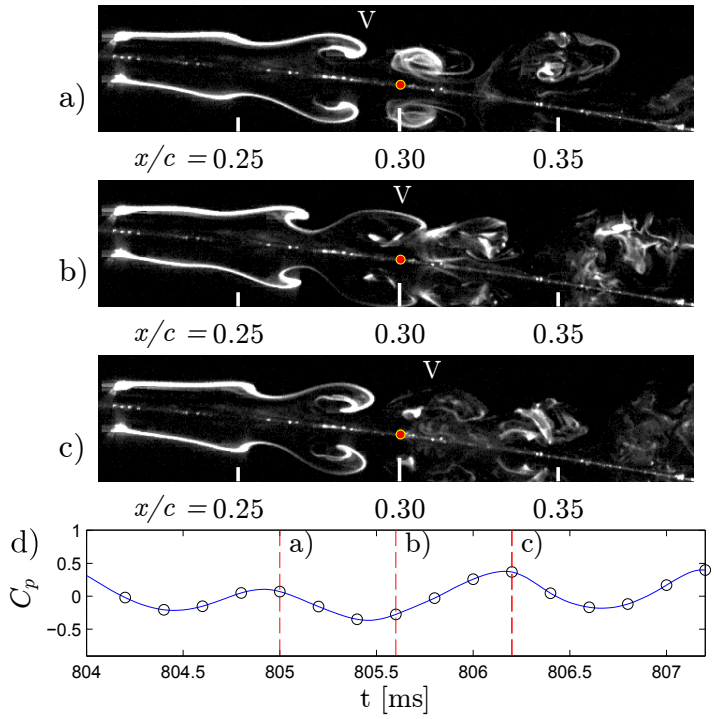

Figure 4.10: Surface pressure fluctuations induced by shear layer vortex "V" convecting over the microphone indicated in red. A sequence of images in a), b), and c) are shown with their instantaneous pressure measurements in d).

such that the magnitudes of the resulting surface pressure fluctuations approximate those measured experimentally. The results presented in Fig. 4.11a show that the region of low pressure surrounding the vortex core extends to the wall, leading to a pronounced surface pressure minimum (Fig. 4.11b). The model can be extended to a train of vortices, whose streamwise and wall normal spacing are set based on experimental flow visualization. The results of this model are shown in Fig. 4.12 with the mean pressure subtracted as is the case with microphone measurements. These results demonstrate that a train of shear layer vortices induces periodic surface pressure variations, with local pressure maxima attained between the neighboring vortices and pressure minima corresponding to the streamwise location of each vortex. The results of the model in Fig. 4.12 are in good agreement with experimental observation (Fig. 4.10). Thus, the surface pressure fluctuations can be used to detect the streamwise position of vortices downstream of their formation, enabling the quantification of essential elements of vortex dynamics based solely on surface pressure measurements with the microphone array.

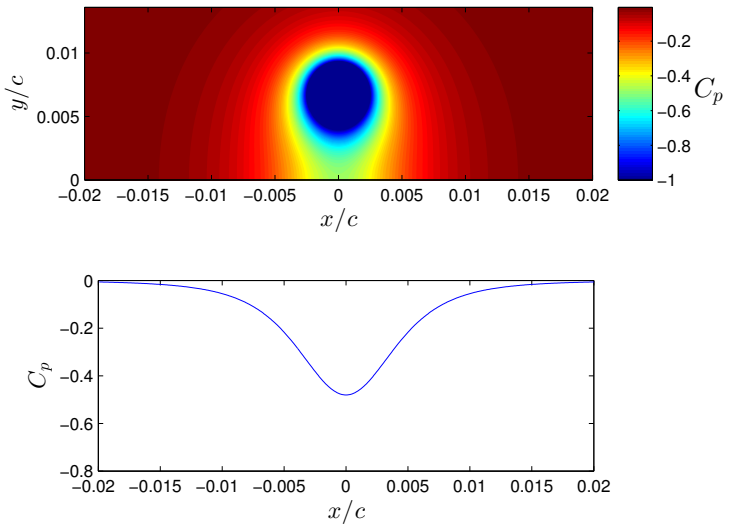

Figure 4.11: Pressure field induced by a single ideal vortex.

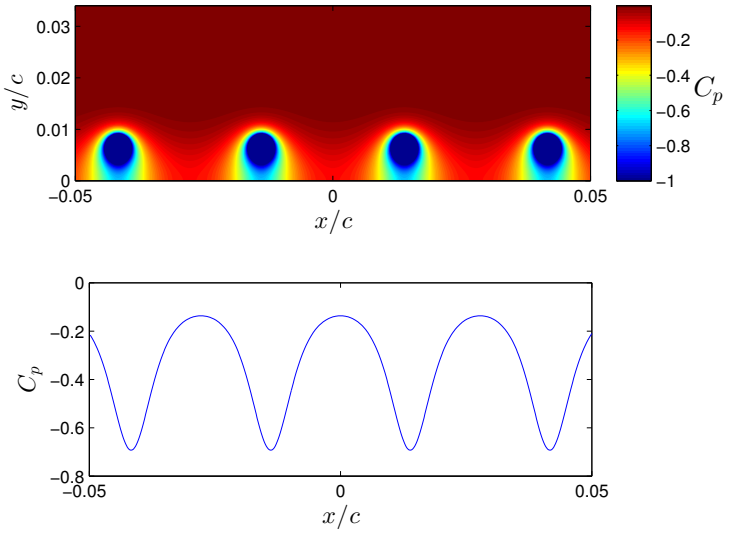

Figure 4.12: Pressure field induced by a sequence of ideal vortices.

4.3 Vortex Merging

A detailed analysis of flow visualization sequences showed that within the periodic vortex shedding, some shear layer vortices may merge in the separation bubble, as illustrated in Fig. 4.13. The images capture a vortex merging phenomenon occurring at approximately $x/c = 0.30$. The vortex located just upstream of $x/c = 0.30$ in Fig. 4.13a is captured merging with the following vortex, which is forming at approximately $x/c = 0.27$ in Fig. 4.13a. It can be seen that the leading vortex is located closer to the wall and, as suggested by the slopes of the dashed lines connecting the same vortex cores in the images, its convective velocity is lower than that of the upstream vortex (Figs. 4.13a-b). The leading vortex gradually slows down and becomes nearly stationary, while the following vortex moves away from the surface and begins to overtake the leading vortex (Figs. 4.13b-c). The vortices begin to orbit as they approach each other (Fig. 4.13d-e) and the cores eventually merge (Fig. 4.13f). The observed vortex dynamics correspond to the four stages of vortex merging defined by Meunier [83] where vortices approach, orbit, and eventually merge.

A vortex merging event with the corresponding surface pressure signals is shown in Fig. 4.14. The results show that the occurrence of vortex merging causes a distinct change to the otherwise periodic pattern of surface pressure fluctuations seen in experimental results in Fig. 4.10 and that predicted by the simplified model in Fig. 4.12. Specifically, when vortex V1 passes over the microphone port, no distinct surface pressure minimum is attained, which is attributed to the close proximity of the upstream vortex V2 (Fig. 4.14a). As the vortices begin to orbit and merge over the microphone port, they instead produce a single minimum in the surface pressure signal at that location (Fig. 4.14b). Once the pair have passed the microphone port (Fig. 4.14c), the surface pressure begins to recover, resuming the periodic trend expected for the continuous vortex street passing over the surface (e.g., Fig. 4.12). The pressure signal reflects the two minima in the pressure signals approaching each other and becoming conjoined as the vortices merge together. The results suggest that, by detecting such events in surface pressure signals, the occurrence and location of vortex merging can be identified.

To model the initial vortex interaction during the merging process and the associated surface pressure response, an inviscid pair of co-rotating vortices were modeled near the wall in the presence of uniform free stream, with the velocity fields evaluated directly and the positions solved numerically. The vortices were assigned the same circulation and spacing as in the stationary vortex train simulation (Fig. 4.12). The results shown in Fig. 4.15 show that the vortices begin to orbit as they advect downstream. This orbiting is driven by the velocity induced by the vortices and their mirror pairs. Similar to the experimental observations, the leading vortex moves closer to the surface, while

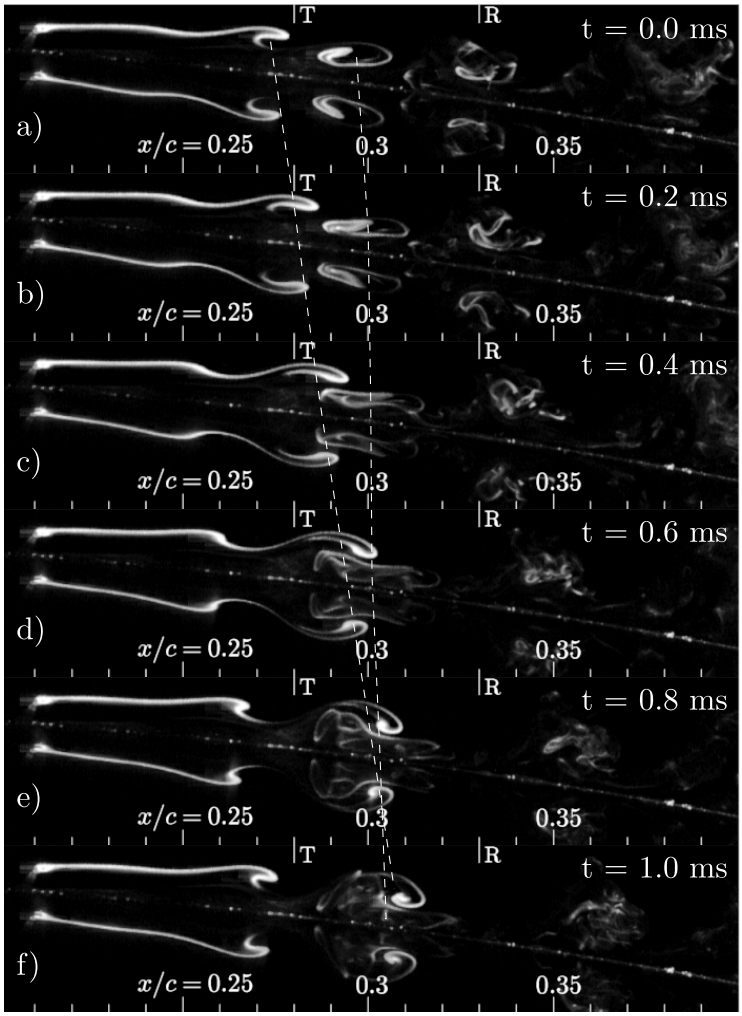

Figure 4.13: Visualization of vortex merging inside the separation bubble. The consecutive images are separated by 0.2 ms. The dotted lines connect the same vortices in the images, with the slope of the lines being indicative of convective speeds of the structures.

the following vortex moves away from the surface. As a result of the change of vortex positions relative to the wall, the convective velocity of the leading vortex decreases, while that of the following vortex increases. This is similar to the trend seen in visualization images in Fig. 4.13, however, in a separation bubble, the difference in relative convective velocity is exaggerated by the wall-normal velocity gradient. The model shows that the time history of surface pressure fluctuations features a single minimum for the pair of

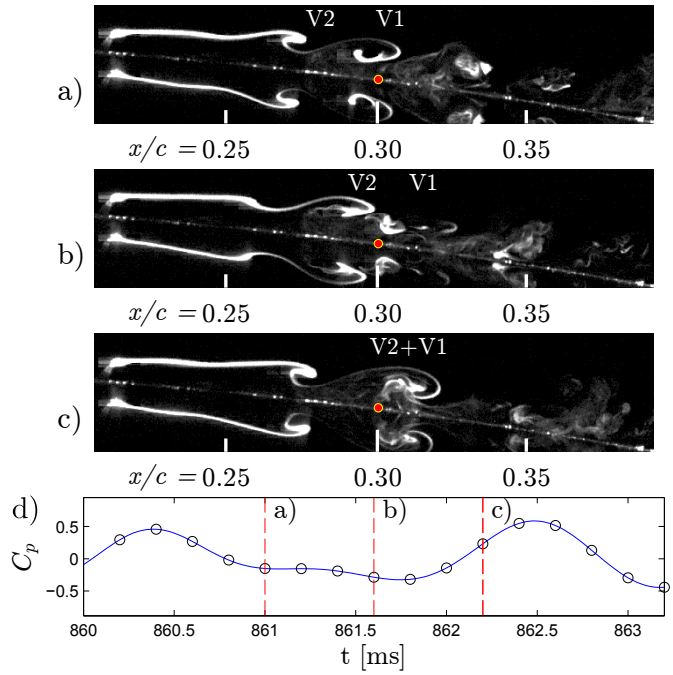

Figure 4.14: Surface pressure signals produced due to merging of two shear layer vortices.

vortices (Fig. 4.15), similar to the experimental observations (Fig. 4.14). The vortices are closest to each other when they are one above the other, and this proximity would promote merging in the viscous case. It should be noted that the location of the surface pressure minimum in the model corresponds to position of the leading vortex, while this occurs during the last stage of vortex merging in the experiment. This is attributed to the fact that the leading vortex undergoes significant deformation and begins to break down in experiments, while its circulation remains constant in simulations. Nevertheless, the results of the model confirm that the occurrence of vortex merging can be detected from the presence of a pair of minima upstream resulting in a single minimum in the surface pressure signal downstream.

Based on the comparison of the model and experimental results, it can be deduced that the merging process is driven by the differences in convective velocities of the two consecutive vortices. The fact that merging events are not observed regularly in the separation bubble suggests that they are the consequence of some perturbations in the vortex shedding process involving the spacing between the consecutive vortices and/or their strength. Once such a perturbation occurs, it develops into the orbiting motion of the two consecutive

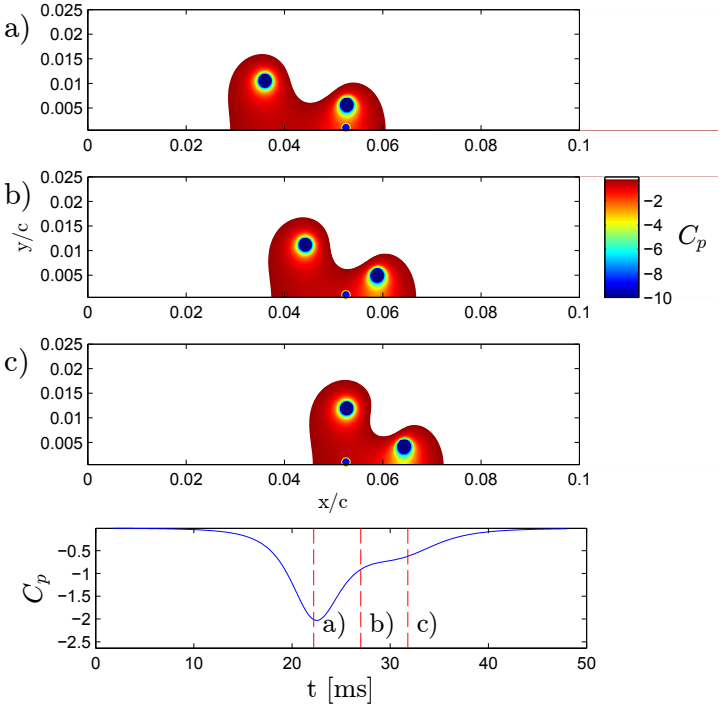

Figure 4.15: Inviscid simulation of a pair of vortices of equal strength. Vortices rotate in a clock-wise direction, with a mean flow imposed from left to right.

vortices. As mentioned earlier, the rate of change of convective velocity, which is driven purely by the effect of induced velocity in the model, is increased in real flow due to the substantial wall-normal velocity gradient within the separation bubble. The mean velocity profile at $x/c = 0.24$ is presented in Fig. 4.16 from the experimental velocity measurements by Kirk [6] for the same experimental facility, conditions, and airfoil geometry. The effects of mean velocity gradient and induced velocity on the rate of change of convective velocity with vertical distance from the wall are assessed in Fig. 4.17. From flow visualizations, the cores of the vortices are expected to be within $0.008 \leq y/c \leq 0.01$ at $x/c = 0.3$. For this vertical interval, the effect of induced velocity is estimated based on the model results, and is calculated as the rate of change in the convective velocity of a given vortex in the pair undergoing orbiting. It should be noted that in the real flow this effect is expected to be smaller than that in the inviscid model due to the significant temporal changes in the circulation of the vortices as well as other viscous effects. Comparing the results in Fig. 4.17, it can be seen that in the y/c range of the vortices, the rate of change in convective velocity due to the mean wall-normal velocity gradient is expected to be at least three times that

due to induced velocity. This is substantiated by the notable differences in the time scale associated with vortex orbiting captured in experiments (Fig. 4.14) and the model (Fig. 4.15), with the higher rate of orbiting motion seen in experiments. The implication here is that vortex merging in the separation bubble is likely caused by a perturbation in the initial relative position of two consecutive vortices, which gives rise to the strong relative motion of the structures. Based on previous investigations of vortex merging [82, 85], the merging of the cores then occurs once the vortex spacing reaches a critical fraction of the vortex core size.

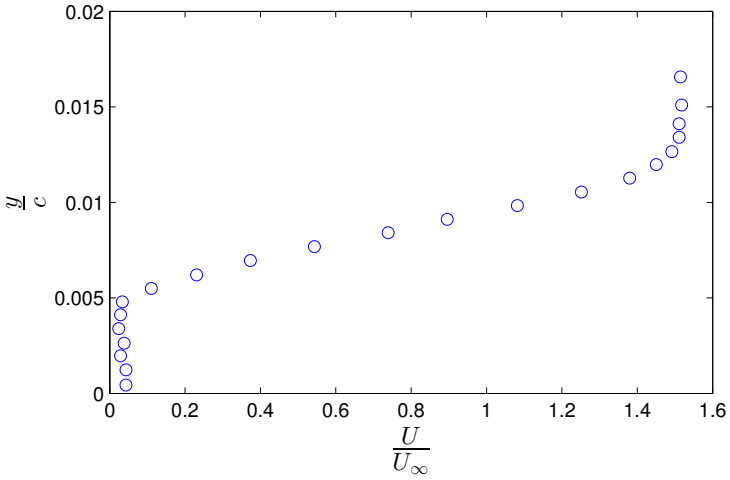

Figure 4.16: Experimental streamwise velocity profile at $x/c = 0.24$. These measurements were performed by Kirk [6] using hot-wire anemometry.

4.4 Vortex Tracking

4.4.1 Image-Based Tracking

The time-resolved nature of the acquired flow visualization images allows quantitative measures of the vortex dynamics to be extracted from the images. An example flow visualization sequence with the identified vortex cores is shown in Fig. 4.18. As the vortices develop, their structure is ill-suited for tracking when the vortices are emerging and breaking down. To facilitate tracking, an ellipse is fit to the features of the vortices. When the wave begins to emerge, the core is identified as the centre of the ellipse fit to the

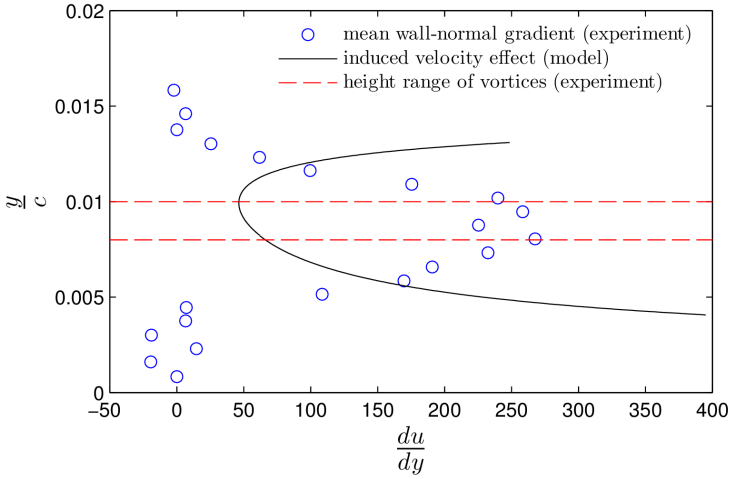

Figure 4.17: Comparison of rates of change of convective velocities estimated at $x/c = 0.3$. The experimental results are based on Kirk [6] and the simulation data serves to approximate the effect of induced velocity.

emerging crest and trough in the smoke filament. As the structure continues to roll up, the ellipse is fit to the emerging structure. Using this method, the structures were tracked between approximately $x/c = 0.24$ and 0.32, with an estimated uncertainty of 0.004 x/c.

The results of a segment of visual vortex tracking are shown in Fig. 4.19. In this figure, the positions of the vortices along the airfoil are tracked through time. These measurements show the downstream advection of vortices, as well as evidence of vortex merging. The slopes of the lines show the downstream velocities of the vortices. These vortices show similar speeds, aside from immediately before merging. Before a merging event, the downstream vortex slows drastically and is overtaken by the following vortex, as exhibited in the typical merges in Fig. 4.13 at $t = 813$ ms and 817 ms. These pairs of vortices that merge tend to have an initially smaller separation. The vortices become less suitable for tracking where they begin to lose coherence at around $x/c = 0.29$, with most having begun to break down by mean reattachment near $x/c = 0.32$. The visual tracking of vortices provides a reference for the development of vortex identification methods using embedded microphones.

The vertical positions of the vortices are expected to impact the magnitudes of the pressure signals produced [70]. The vertical positions of the vortices above the chordline are plotted in Fig. 4.20 along with a moving average of the positions. In the vicinity of $x/c = 0.25$ where vortices are forming, the vortex positions show a smaller range.

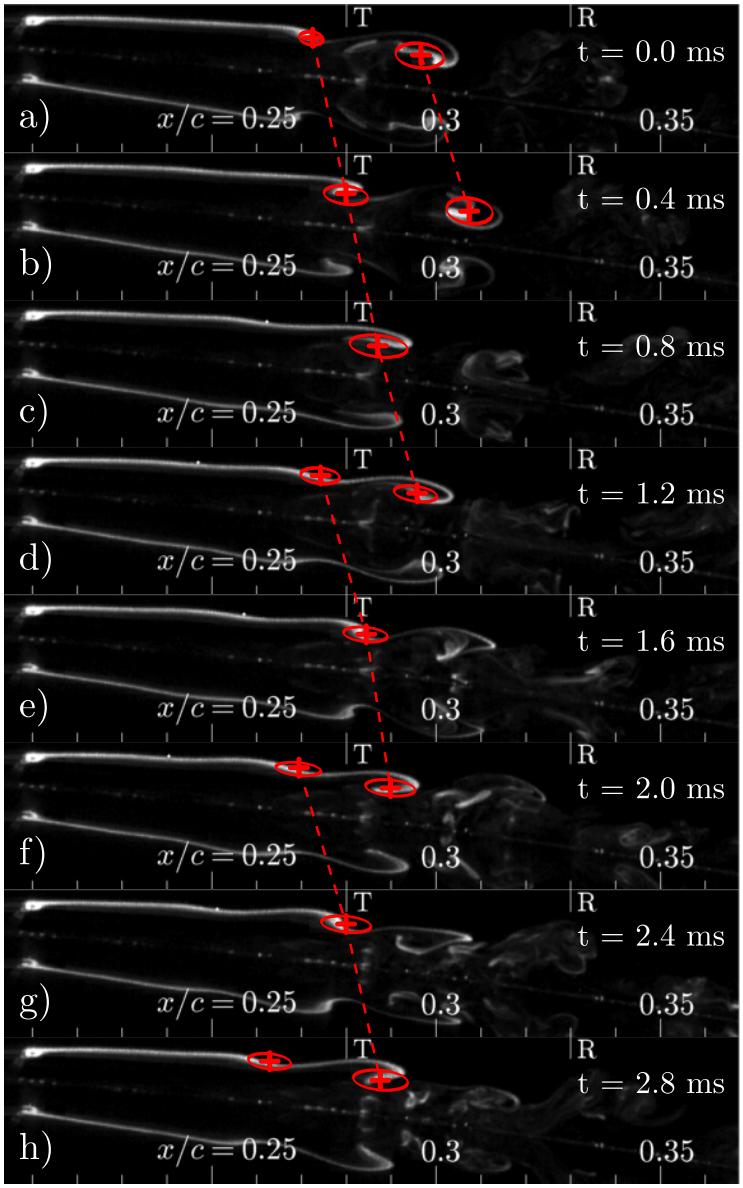

Figure 4.18: Sample of vortex positions identified from flow visualization images. The centres are identified by fitting an ellipse to the crest that forms as well as the displacements of the smoke filament. Images are presented at intervals of 0.4 ms.

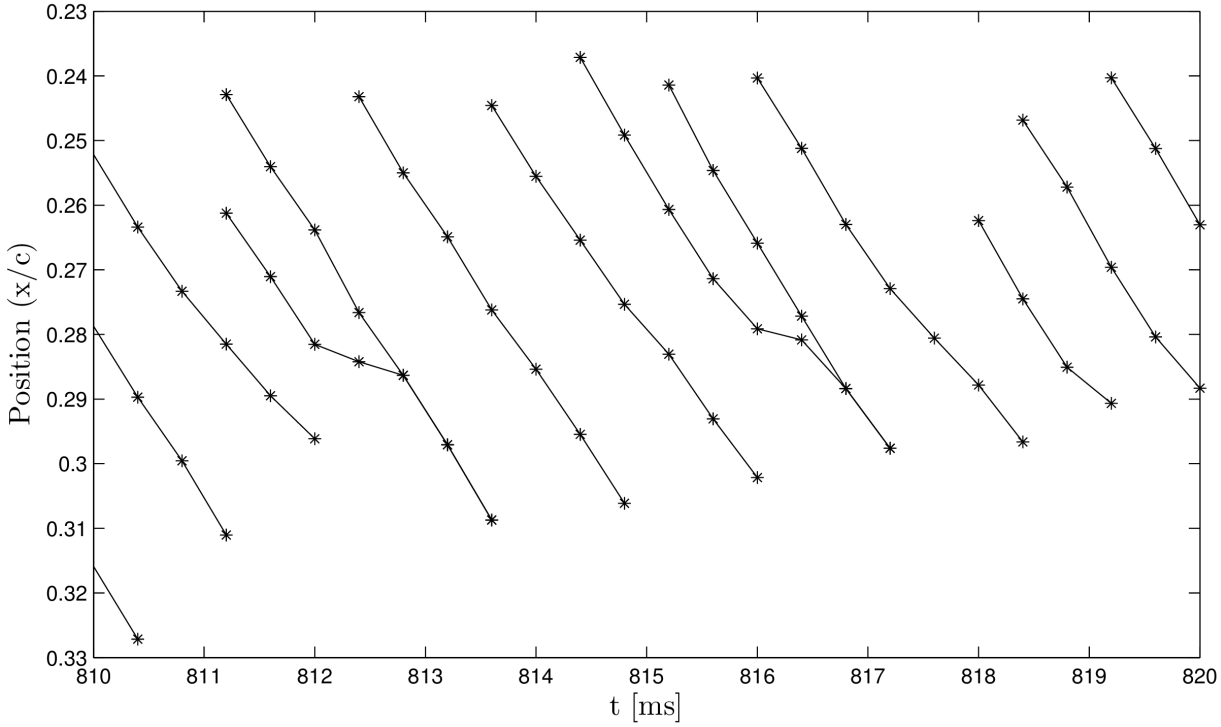

Figure 4.19: Vortex positions as identified from flow visualization images.

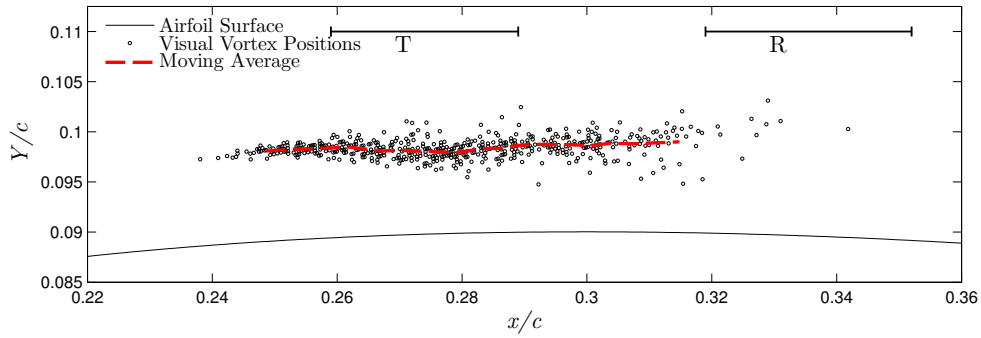

Figure 4.20: The positions of vortices above the chordline as identified from flow visualizations. The moving average is calculated over 75 vortex positions.

Downstream, the vertical positions have greater variation as the vortices are displaced towards and away from the wall as part of the merging process. The overall trajectory of the vortices is also curved due to the flow separating and reattaching. The heights reach a local minimum at mean transition from static pressure measurements ($x/c = 0.28$). This agrees with the time-averaged visualization image in Fig. 4.4 where the main smoke filament deflectd towards the wall at mean reattachment. Boundary layer growth then increases the heights of the vortices until they lose coherence. The closer vortices are to the surface the larger the pressure minimum they induce, so the variation in heights will impact the measured strengths of the vortices shown subsequently in Section 5.2.

4.4.2 Tracking by Cross-Correlation

To quantitatively characterize the development of individual vortices forming in the separation bubble, each vortex structure can be identified and tracked using surface pressure signals. To isolate vortex activity, the pressure signals were band-pass filtered from 550 to 1450 Hz post-acquisition using a non-causal filter with zero phase lag. A schematic of the employed vortex tracking method is shown in Fig. 4.21. To track the vortices between two neighboring pressure sensors, the mean time lag between the corresponding signals is first calculated using the cross-correlation applied to the entire length of sampled signals. For each detected minimum in surface pressure at an upstream station, the mean lag is used to predict the time at which the corresponding minimum should appear in the signal at the downstream station. Signal segments around the minimum at the upstream microphone and the time of its anticipated occurrence in the signal from the downstream sensor are windowed with a Hamming window of length $4/(3 * f_0)$, where

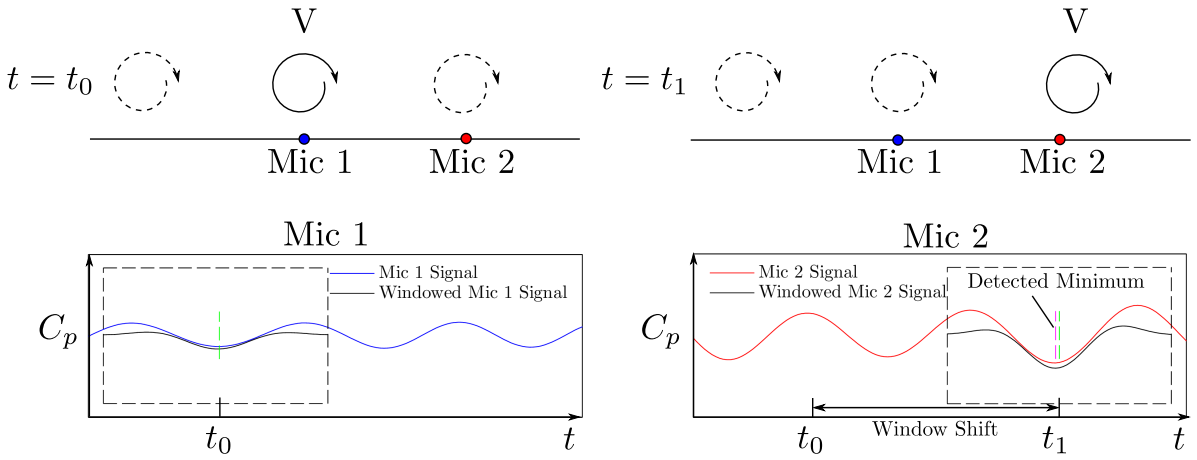

Figure 4.21: Schematic of vortex tracking method for two subsequent microphones. The vortices are detected upstream at Mic 1. A cross-correlation is performed between the two signals to determine the average speed and hence the time the vortex is expected to pass the downstream microphone. Windowed segments of the signals are cross-correlated to determine the positions of the individual vortices through time.

f_0 is the mean vortex shedding frequency (900 Hz). The windowed signal segments are then cross-correlated to identify the precise time of occurrence of the matching pressure minimum at the downstream measurement location. For added robustness, the minima are also detected downstream and cross-correlated with the upstream microphone signals. Any discrepancies or non-physical detections are removed by comparing the upstream and downstream tracking results. By repeating this process, vortex tracking can be performed between pairs of microphones (Fig. 4.22) and then stitched together for arrays of microphones (Fig. 4.23). As a result, individual vortices can be tracked through the separation bubble.

The results of the tracking algorithm are illustrated in Fig. 4.24. From the time that the disturbances are initially detected at $x/c = 0.21$, the minima they induce are tied to the minima detected at the downstream microphones. A comparison between the vortices identified from microphone signals and visualizations shows good agreement between the two in positions and behaviour. The first three cases correspond to three consecutive vortices that convect separately along the chord without merging. However, the fourth and fifth as well as sixth and seventh structures do merge. These vortices are initially closer-spaced than the other vortices that did not merge, and draw closer as they

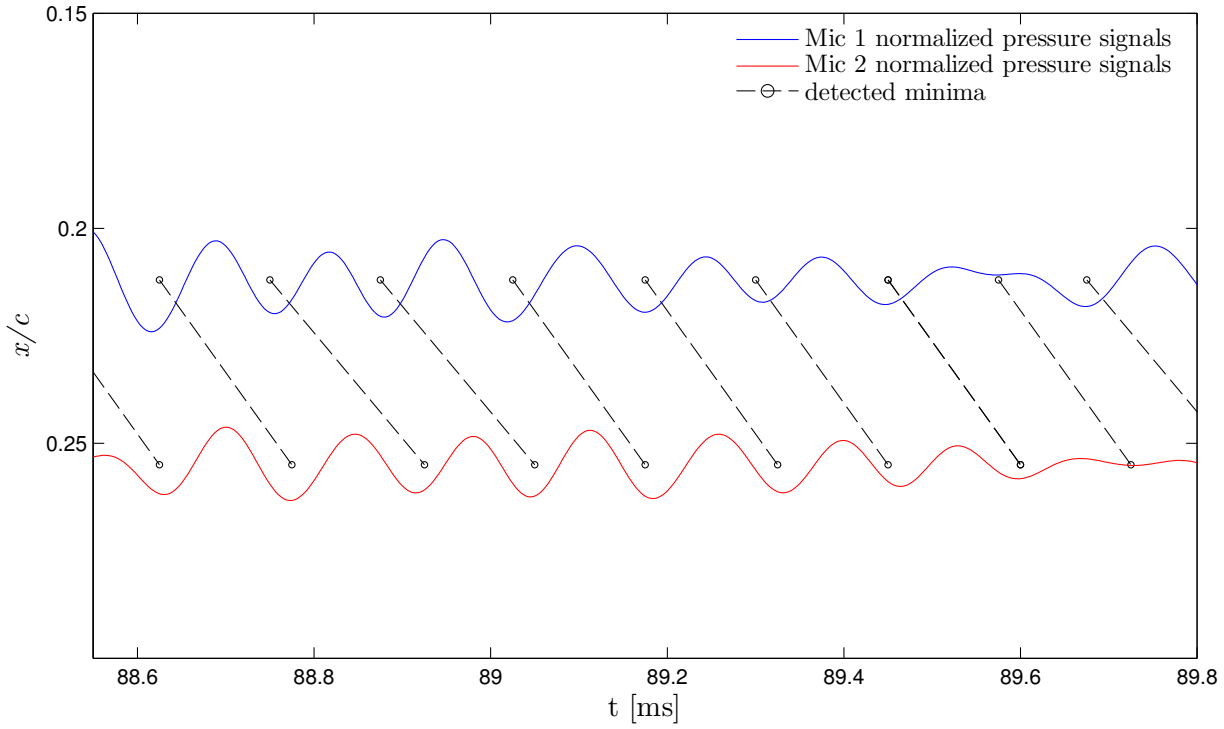

Figure 4.22: Example of typical vortex tracking between two microphones, showing a range of individual convective velocities. The normalized pressures are plotted through time, centered at the chord-wise position of the microphones.

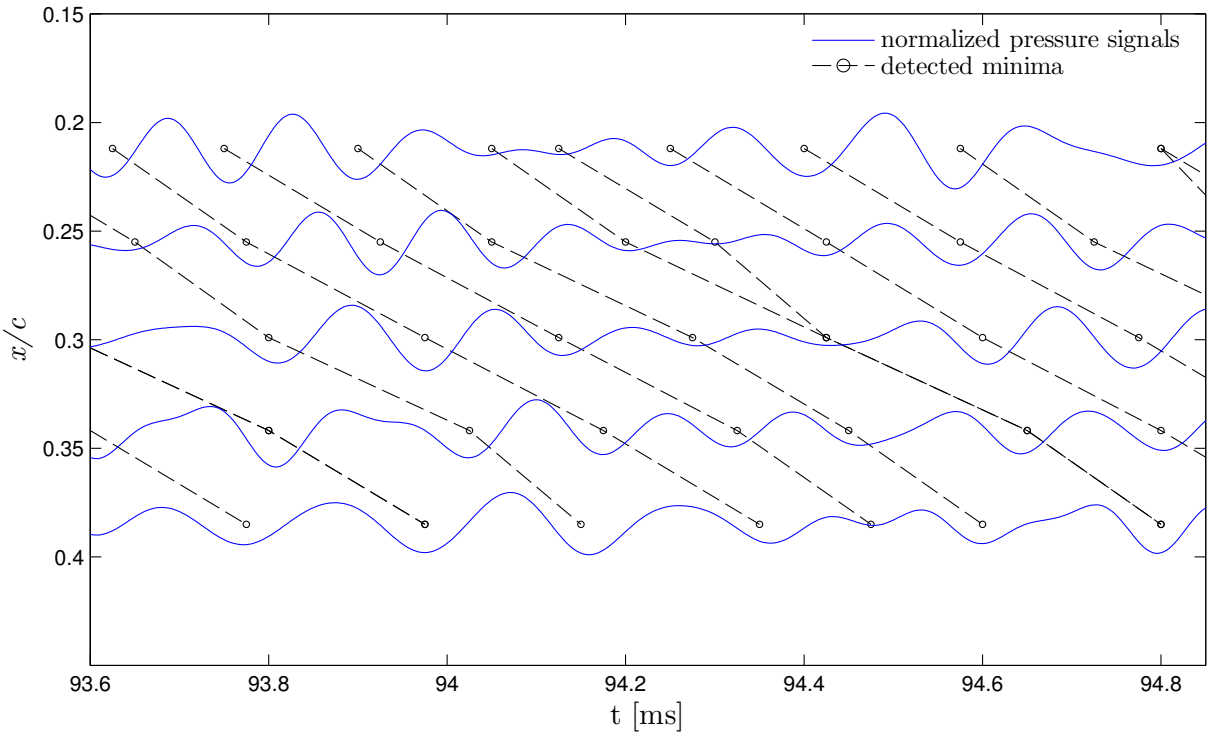

Figure 4.23: Schematic of vortex tracking along the separation bubble, showing tracking results. Merging is detected when two vortices upstream progress to a single vortex downstream, as at $t = 94.4$ ms and $x/c = 0.3$.

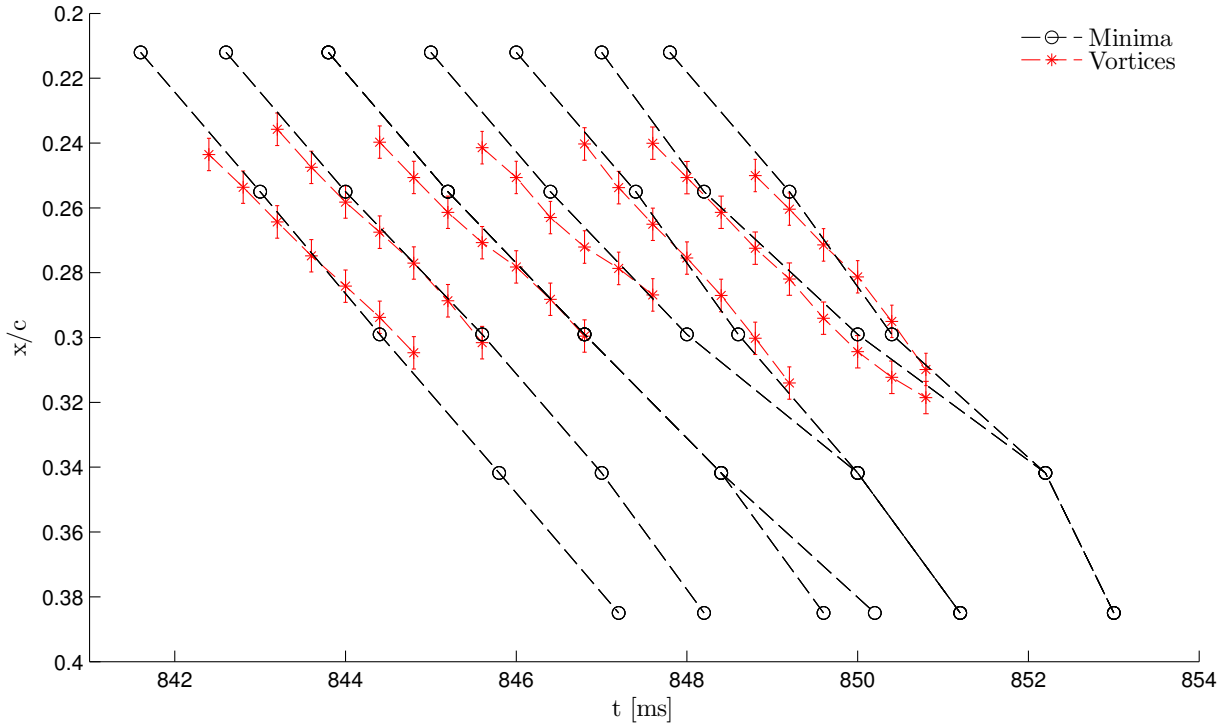

Figure 4.24: Positions of vortices as identified from flow visualizations at $AOA = 8°$ are compared with the positions identified from the cross-correlation of minima.

approach $x/c = 0.34$, where they merge, which is in the range of merging observed in the flow visualization. The fourth vortex initially has a similar if slightly lower speed to the preceding vortices, but it slows appreciably between $x/c = 0.3$ and 0.34, while the fifth vortex maintains a relatively constant speed. This slowing leading to a merge matches the flow visualization (Fig. 4.13) as well as the simulation (Fig. 4.15). The agreement between pressure minima tracking and visual tracking gives confidence in using the minima tracking to resolve properties of the vortices.

4.4.3 Pattern Recognition

When looking to classify events, pattern recognition can be used if there is a set of training data to "teach" the pattern recognition algorithm. In this case, the desire is to use the flow visualization of structures to tie the events in the flow to the measured pressure signals. This allows the use of an algorithm that categorizes events in the flow based on

their associated features in the pressure signals. The detected minima are classified as follows: Background, Vortex, Merged Vortex, and Breakdown. Features of the pressure signals are selected based on the characteristic of events seen from the flow visualizations. The features selected include the following: magnitude of minima, interval to preceding and following minima and maxima, and magnitude of adjacent maxima. These seven features aim to capture the changes in the signal shape that accompany vortex roll-up as well as merging, as shown in Fig 4.14. The distribution of properties of a selected pair of features is shown in Fig. 4.25. Based on an assumed gaussian distribution within each feature, the probabilities of an event belonging to each class is calculated. The event is then assigned to the class that it most closely resembles. However, there is significant overlap of the features between the classes, where the growth and then decay of the vortices makes the magnitudes and time intervals similar between the earlier and later stages of vortex development. For example, as vortices break down they produce more closely-spaced minima, similar to vortices approaching each other during merging. Additionally since this is a case of an unforced separation bubble, there is a range of disturbances introduced to the flow, so the change of intervals as vortices merge is comparable to two initially closely-spaced disturbances. Hence, given the requirement of training data as well as the moderate accuracy of the technique, pattern recognition has a limited usefulness for the less-regular vortex dynamics in this unforced transitioning flow and was not pursued for this investigation.

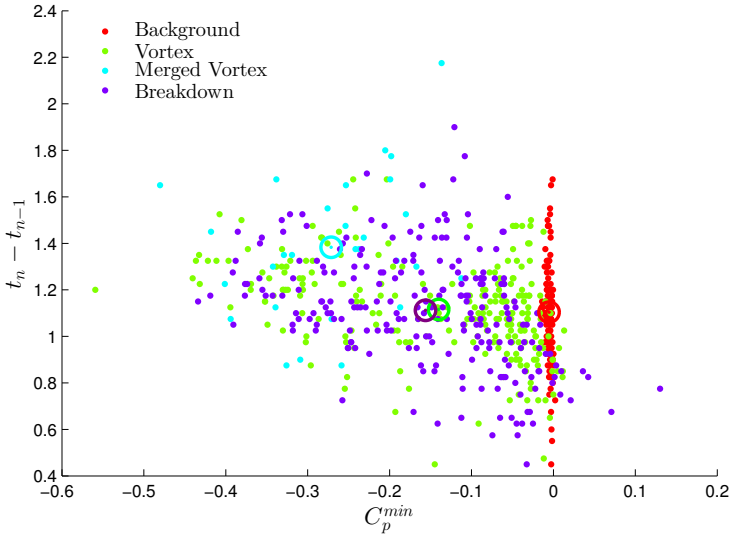

Figure 4.25: Sample of distributions of features for the detected minima. The four classes are shown as the smaller circles, while the averages are shown with the larger unfilled circles.

Chapter 5

Vortex Dynamics Characterization

From the relationship between the vortices and surface pressure signals established for $AOA = 8°$ in Chapter 4, a technique was developed to track the vortices based on the measurements of fluctuating surface pressure. These techniques capture the formation, evolution, and dynamics of coherent structures within the Laminar Separation Bubble (LSB), which is the main focus of this work. These techniques were applied to other angles of attack. Flow visualizations for angles of attack of 0°, 5°, 8°, and 10° are investivated in Section 5.1. In Section 5.2, the properties of vortex development for $AOA = 5°$, 8°, and 10° are investigated using microphones to see how they change with angle of attack. It should be noted that $AOA = 0°$ is not included in this section due to the separation bubble being outside the range of the embedded microphones. Vortex merging was quantified using the cross-correlation vortex tracking algorithm in Section 5.3. These measurements illustrate how vortex dynamics change in the separation bubble with increasing angle of attack.

5.1 Flow Visualization

The flow visualizations at different angles of attack aim to quantify changes in vortex activity with respect to angle of attack. The visualizations give a reference on the vortex dynamics for comparison with the vortex tracking techniques.

Flow visualization sequences at $AOA = 0°$, 5°, 8°, and 10° are presented in Figs 5.1-5.4. In these image sequences, the smoke filaments exhibit unsteadiness developing as they are carried with the flow. Vortices form for all the cases examined, with characteristic wavelengths decreasing with increasing angles of attack. At all of these angles, merging

occurs. When merging occurs, it increases the spacing between the merged structure and theupstream vortex. The vortices begin to break down past mean transition, and form small-scale structures as the smoke diffuses past mean reattachment.

As the angle of attack is increased, the separation bubble moves upstream. The location where vortices begin to roll up advances from $x/c = 0.75$ at $AOA = 0°$ to $x/c = 0.39$ at $AOA = 5°$, $x/c = 0.26$ at $AOA = 8°$, and $x/c = 0.18$ at $AOA = 10°$, with unsteadiness beginning to emerge around one vortex wavelength upstream of the roll-up. The wavelength of the emerging vortices decreases with increasing angle of attack from a spacing of approximately $x/c = 0.05$ at $AOA = 0°$ to $x/c = 0.04$ at $AOA = 5°$, $x/c = 0.03$ at $AOA = 8°$, and $x/c = 0.02$ at $AOA = 10°$. Vortices are shed at approximately $f = 350Hz$ at $AOA = 0°$, $f = 650Hz$ at $AOA = 5°$, $f = 1000Hz$ at $AOA = 8°$, and $f = 1150Hz$ at $AOA = 10°$. The vortices that develop from the shear layer may merge as they approach reattachment. At $AOA = 0°$, the vortices undergo persistent merging, where typically a smaller vortex (Fig. 5.1c at $x/c = 0.80$) is overtaken by a larger vortex (Fig. 5.1c at $x/c = 0.76$) and the pair merge (Fig. 5.1d at $x/c = 0.80$). Since the airfoil is symmetrical, it is speculated that the merging could be impacted by feedback from the LSB on the opposite side [98]. At $AOA = 5°$ (Fig 5.2), merging is less regular than at $AOA = 0°$. Some merging occurs past $x/c = 0.45$ (Fig. 5.2c), which can involve pairs or triplets of vortices. More vortices merge at $AOA = 8°$ than $AOA = 5°$, with examples shown in Fig. 5.2b and e. At $AOA = 10°$ in Fig. 5.4, merging occurs more persistently than $AOA = 8°$ but more chaotically than at $AOA = 0°$. In all of these cases the vortices begin to break down towards mean reattachment, breaking the structures down to smaller scales. Overall, as the angle of attack increases, the structures exhibit smaller scales and faster development along the flow, as well as more variation in the dynamics from cycle to cycle.

5.2 Separation Bubble Characterization

The mean surface pressures distributions at the angles of attack studied are presented in Fig. 5.5. At all AOA, the pressure distributions on the suction side exhibit a pressure plateau past the suction peak, which indicates the presence of an LSB. The suction side pressures return to near $C_P = 0$, which suggests there isn't turbulent separation at the trailing edge. As the angle of attack is increased , the separation bubble advances upstream as the suction peak increases and results in a greater adverse pressure gradient. The magnitude of the surface pressure minimum increases from $C_P = -0.7$ at $AOA = 0°$ to $C_P = -1.8$ at $AOA = 5°$, $C_P = -2.4$ at $AOA = 8°$, and $C_P = -2.8$ at $AOA = 10°$. Separation moves upstream from $x/c = 0.52$ at $AOA = 0°$ to $x/c = 0.24$ at $AOA = 5°$,

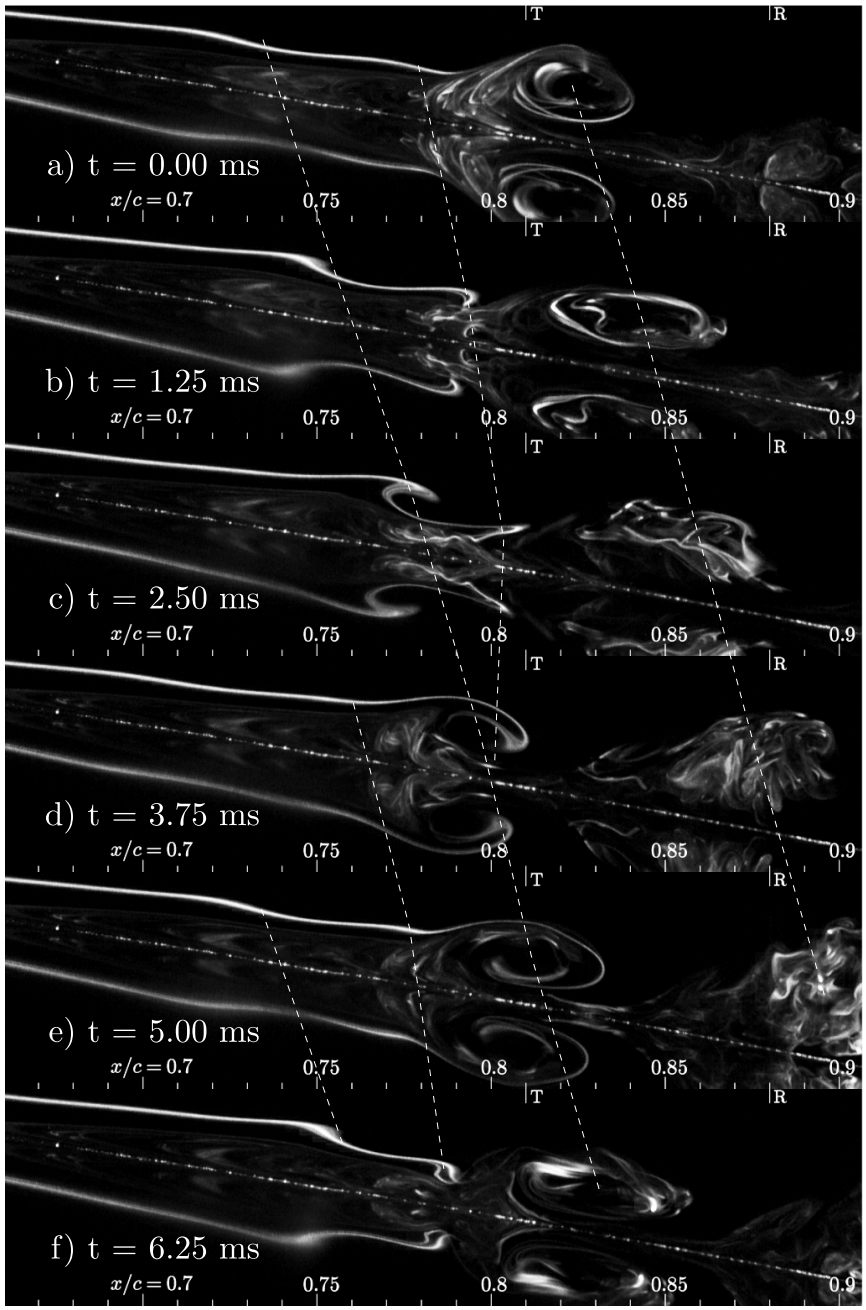

Figure 5.1: Sequence of separation bubble visualizations at $AOA = 0°$ with flow from left to right. Time interval between images is 1.25 ms. Dotted lines give an indication of the spacings and speeds of the vortices.

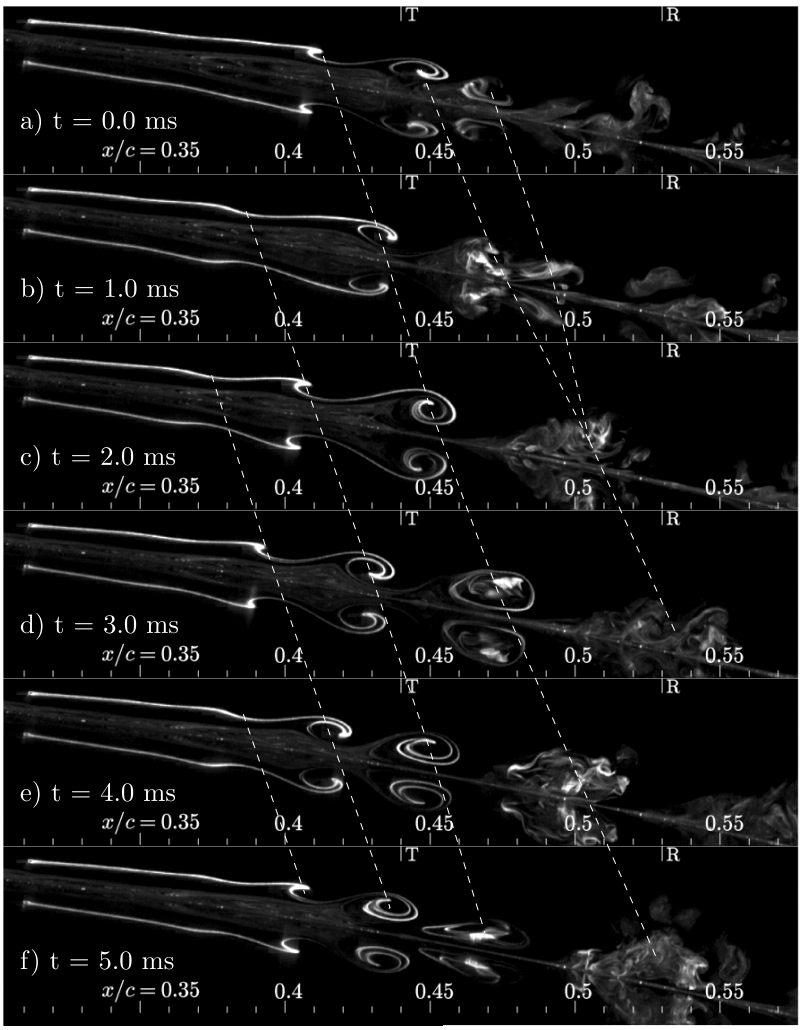

Figure 5.2: Sequence of separation bubble visualizations at $AOA = 5°$ with flow from left to right. Time interval between images is 1 ms. Dotted lines give an indication of the spacings and speeds of the vortices.

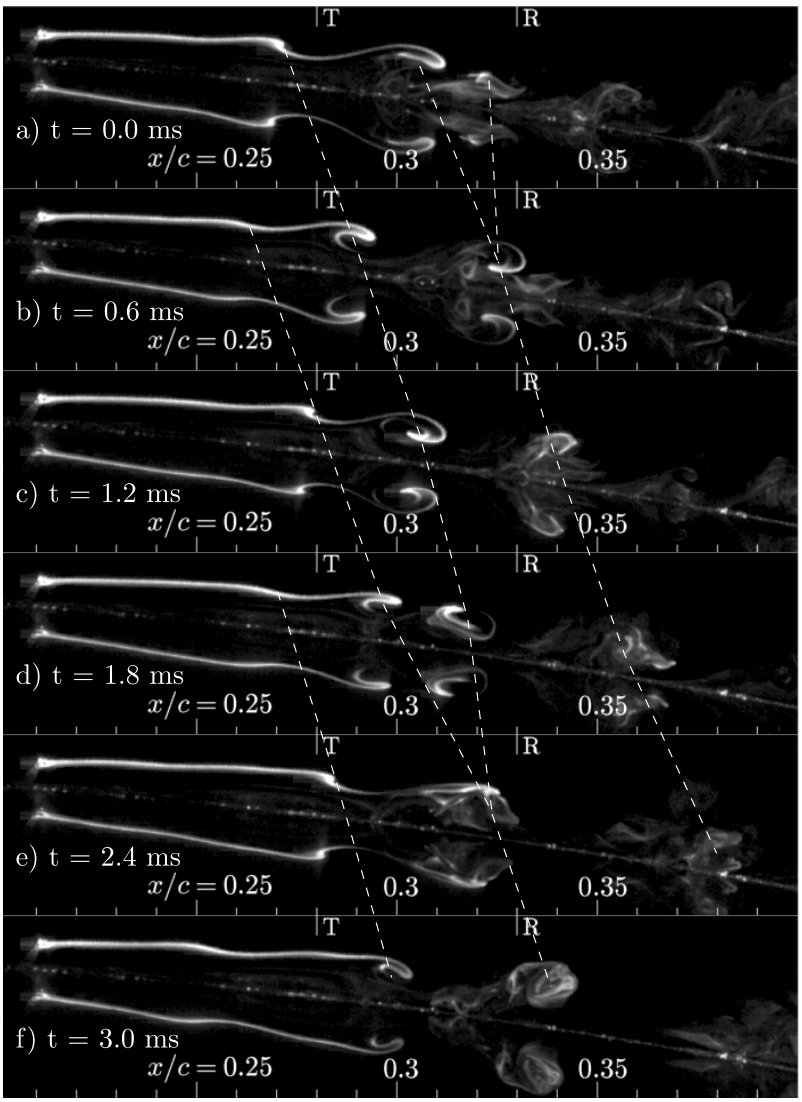

Figure 5.3: Sequence of separation bubble visualizations at $AOA = 8°$ with flow from left to right. Time interval between images is .6 ms. Dotted lines give an indication of the spacings and speeds of the vortices.

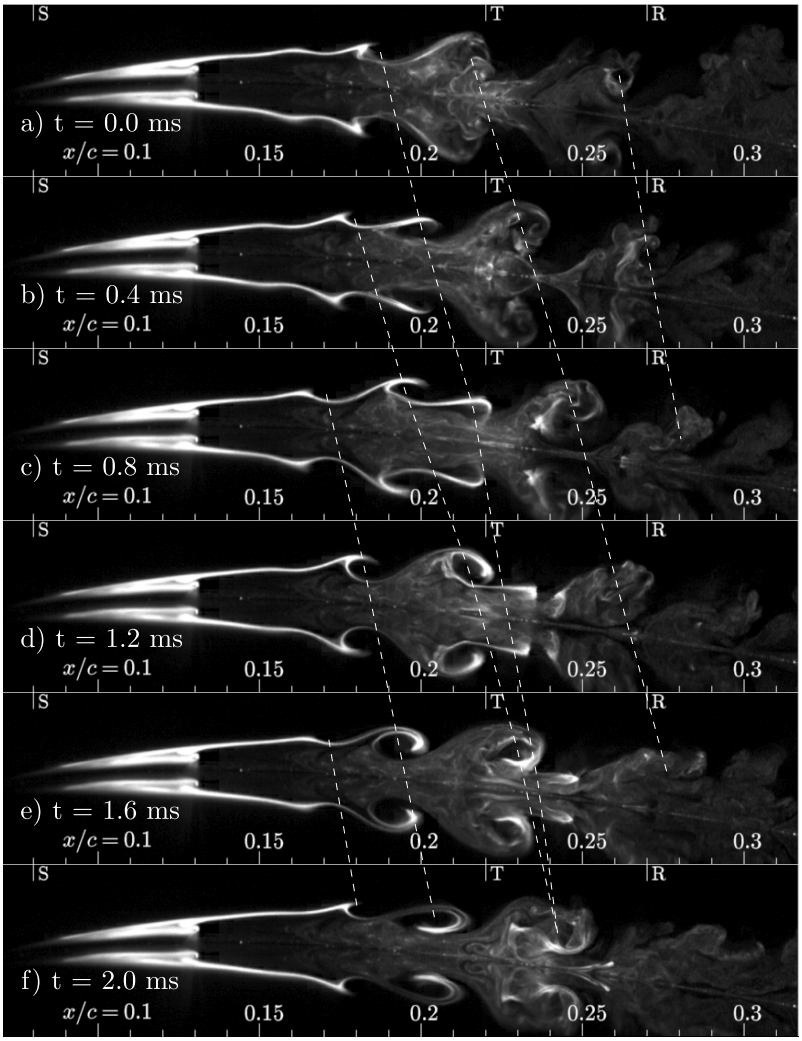

Figure 5.4: Sequence of separation bubble visualizations at $AOA = 10°$ with flow from left to right. Time interval between images is .4 ms. Dotted lines give an indication of the spacings and speeds of the vortices.

$x/c = 0.13$ at $AOA = 8°$, and $x/c = 0.09$ at $AOA = 10°$. At these angles of attack the airfoil also exhibits slight adverse pressure gradients on its pressure side as well. The more negative coefficients of pressure at the locations of the bubble at greater angles of attack mean that there are greater local velocities at the separation bubbles. There are also larger pressure recoveries at reattachment for the greater angles of attack.

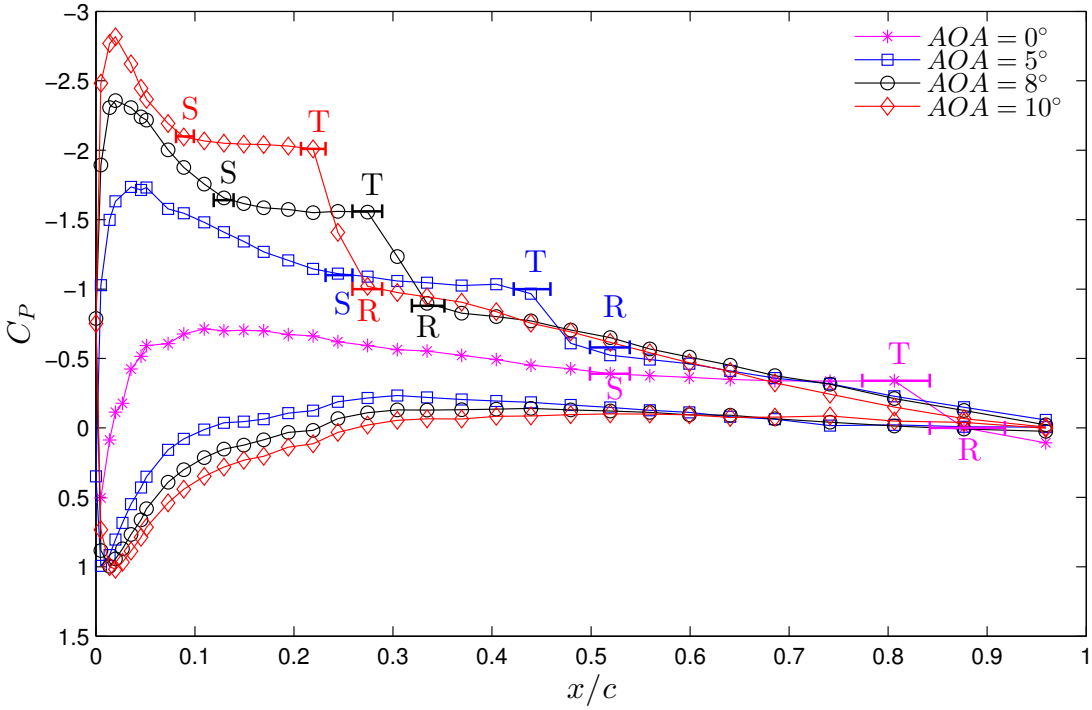

Figure 5.5: Mean surface pressure distributions for angles of attack of 0°, 5°, 8°, and 10°. The locations of mean Separation, Transition, and Reattachment are indicated by S, T, and R respectively. Note that the ordinate axis is reversed.

The progression with angle of attack of the locations of mean separation, transition, and reattachment is summarized in Fig. 5.6. The results show that the separation bubble advances upstream and becomes shorter with increasing angle of attack, as expected for similar low-Re flows over airfoils [65]. While separation moves upstream at greater angles of attack, transition and reattachment also move upstream by a greater amount than separation. Boutilier and Yarusevych [38] found greater spatial amplification rates at greater angles of attack which is mirrored in the faster development of the vortices at larger AOA in Figs. 5.2 to 5.4. While the bubble length decreases overall, the distance between transi-

tion and reattachment remains similar between the angles. From the plots of the pressure distribution in Fig. 5.5, the higher angles of attack have a larger pressure recovery past transition, which would require greater levels of mixing to cause reattachment. However, the distance between transition and reattachment only varies within the resolution of the static pressure taps. The greater mixing required for reattachment at the higher angles of attack is shown by the increases in vortex merging found in the flow visualizations in Figs. 5.3 and 5.4. The distance between transition and reattachment may remain unchanged between AOA due to the increased momentum transfer being balanced with larger pressure recoveries. Separation, Transition, and Reattachment move upstream at greater rate at lower AOA than higher AOA. For similar geometries, previous investigations of the change in extents of the laminar separation bubble with angle of attack show the shrinking of the laminar separation bubble with increasing angle of attack [97, 99]. At the lower AOA investigated by Gerakopulos [97] for a NACA 0018 airfoil and Lee & Gerontakos [99] for a NACA 0012 airfoil, the locations of S, T, and R move upstream at a greater rate than at higher AOA. This can be explained by the shape of the mean pressure curves, where at smaller AOA the pressure recovery is much more gradual at separation than it is at greater AOA. At the larger AOA studied, the development of momentum transfer within the flow supports a greater pressure recovery over a shorter LSB than at lower AOA.

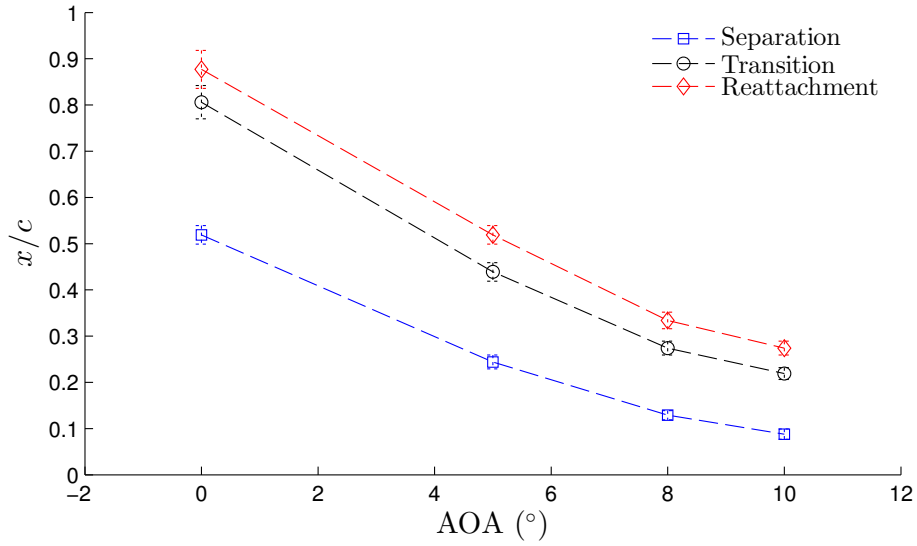

Figure 5.6: Variation with angle of attack of positions of mean separation, transition, and reattachment as identified from mean surface pressure measurements at $AOA = 0°$, 5°, 8°, and 10°.

The root-mean-square of pressure fluctuations is presented for $AOA = 5°$, $AOA = 8°$, and $AOA = 10°$ in Figs. 5.7a-5.7c. As seen in Fig. 4.8, the pressure fluctuations grow to a maximum past mean transition and reduce towards mean reattachment. The farthest measurements upstream are within the level of noise of $C_{p'} = 0.025$ and hence do not show the expected early exponential growth. The rms levels rise to around $C_{p'} = 0.2$ in all of these cases before decreasing. From the visualizations in Figs. 5.2-5.4, vortices have begun to roll up before the fluctuating pressures reach $C_{p'} = 0.1$. As discussed previously, roll-up occurs at $x/c = 0.39$ at $AOA = 5°$, $x/c = 0.26$ at $AOA = 8°$, and $x/c = 0.18$ at $AOA = 10°$. The decreases in fluctuating pressures correspond to the vortices beginning to break down upstream of reattachment.

The development of the frequency components of fluctuations is shown in the power spectra in Figs. 5.8a, 5.8b, and 5.8c for angles of attack of 5°, 8°, and 10°. At all of these angles of attack, energy content is amplified in a frequency band, grows at lower frequencies, and progresses into a broadband spectrum indicative of turbulent flow. In all of these cases, there is an initial amplification of a band of disturbances at the upstream locations. This band encompasses the vortex shedding frequencies identified from flow visualizations. Since it is a band rather than a distinct peak, the range of frequencies corresponds to the range of wavelengths seen in the flow visualizations. The center of this band increases from $f \approx 600Hz$ at $AOA = 5°$ to $f \approx 900Hz$ at $AOA = 8°$ and $f \approx 1150Hz$ at $AOA = 10°$. The growth in frequency content is mostly within this band earlier along the separation bubble until the vortices start rolling up, but the frequency begins to spread past mean transition at $x/c = 0.44$, 0.27, 0.22 at $AOA = 5°$, 8°, and 10° respectively. The energy content at frequencies lower than the amplified band then grow at lower frequencies due to the merging of vortices in the vicinity of transition. This low-frequency growth accompanies growth at higher frequencies as the vortices break down to smaller scales near reattachment. Past reattachment ($x/c = 0.52$, 0.33, 0.27 at $AOA = 5°$, 8°, and 10° respectively) the spectra begin to lose energy within the frequencies of the initially amplified band of disturbances. This is also where the rms of the pressure spectra decreases in Figs. 5.7a-5.7c. It should be noted that at the most upstream locations the spectra indicate some peaks at frequencies due to 60 Hz electrical noise as well as harmonics of the acoustic resonances of the height and width of the test section ($f \approx 190Hz$ and $f \approx 280Hz$). The electical noise is covered as the signal amplitudes increase. However, the harmonics of $190Hz$ and $280Hz$ that occur within the amplified frequency bands do grow and impact the shape of the frequency spectra, such as $f \approx 570Hz$ in 5.8a. However, this does not have a dominant impact on the emerging frequencies or the vortex-shedding frequencies observed.

The microphone signals were bandpass filtered around the amplified band of frequencies

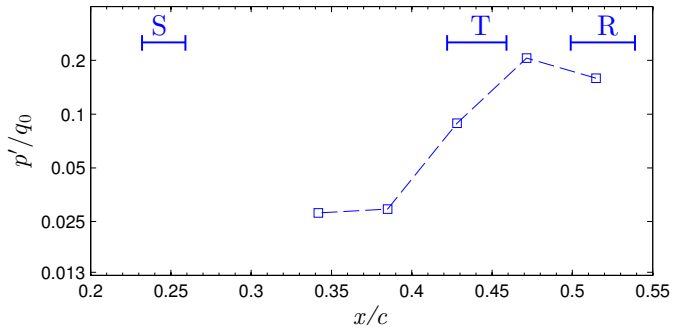

(a) $AOA = 5°$

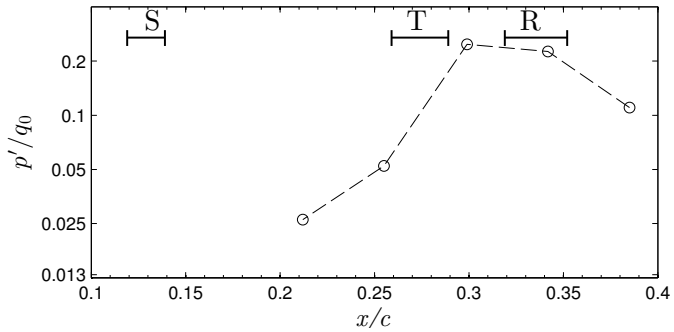

(b) $AOA = 8°$

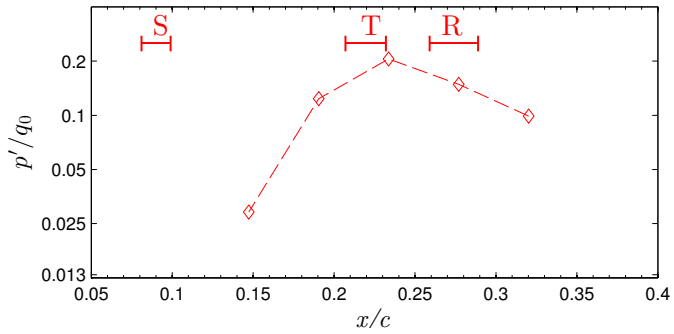

(c) $AOA = 10°$

Figure 5.7: Root-mean-square of pressure fluctuations for microphone signals plotted along the chord at $AOA = 5°$, $8°$, and $10°$.

to isolate activity associated with vortices. A non-causal filter with zero phase lag was applied to the microphone signals, with the pass width set to the band of frequencies identified from the first microphone where the rms increases past the level of the background

noise. These bands are $450 \leq f \leq 850Hz$ at $AOA = 5°$, $600 \leq f \leq 1250Hz$ at $AOA = 8°$, and $700 \leq f \leq 1650Hz$ at $AOA = 10°$, with a passband ripple of less than $0.5dB$. The rms of these filtered pressure fluctuations are presented in Fig. 5.9. The results show the initial nearly exponential growth in the earlier portions of the separation bubble that is masked by noise in Figs. 5.7a-5.7c. The increase in slope of the maximum growth in rms with angle of attack indicates that there is an increase in the spatial growth rate with increasing AOA. This matches the faster development of vortices seen in the flow visualizations (Figs. 5.2-5.4). The rms of pressure fluctuations is plotted along normalized separation bubble length in Fig. 5.10. On this semi-logarithmic scale, all of the angles of attack have a similar slope of rms of pressure fluctuations with respect to separation bubble length before transition. This indicates similar exponential growth rates when normalized by the bubble length. Downstream of transition, the growth rate diminishes but the levels continue to grow to a peak at around 80% of the separation bubble length. As seen in the unfiltered results, the rms of fluctuations decreases towards reattachment as the vortices begin to break down.

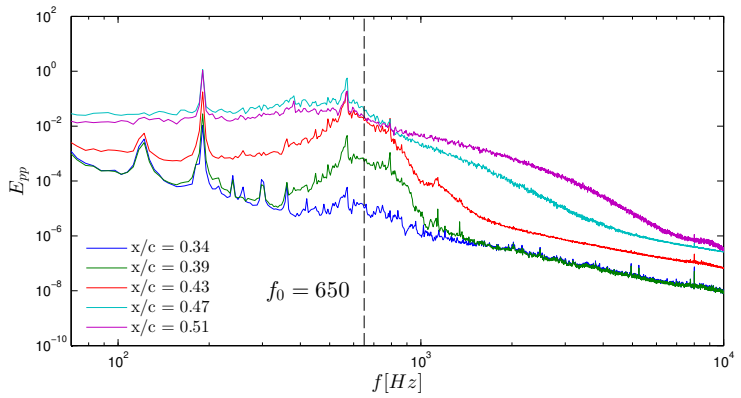

(a) $AOA = 5°$

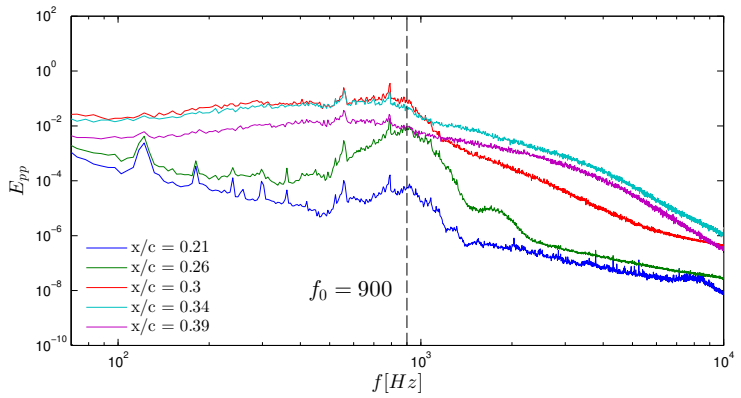

(b) $AOA = 8°$

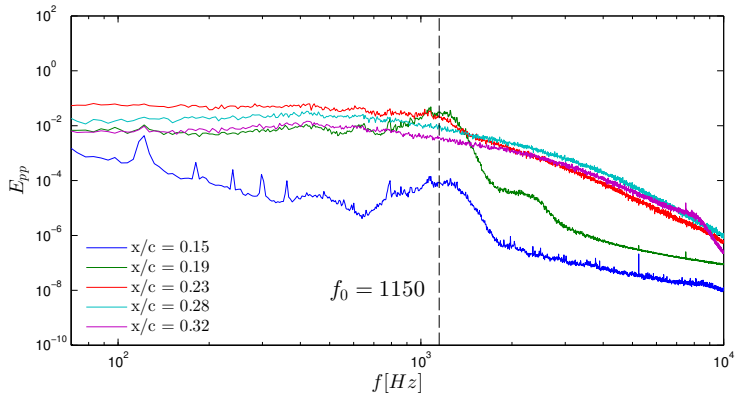

(c) $AOA = 10°$

Figure 5.8: Power spectral density of microphone pressure signals along the separation bubble at $AOA = 5°$, $8°$, and $10°$.

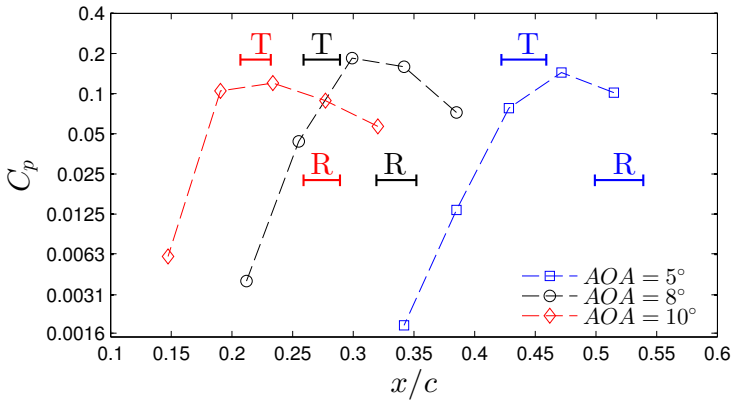

Figure 5.9: Root-mean-square of pressure fluctuations for bandpass-filtered signals plotted along the chord at $AOA = 5°$, $8°$, and $10°$.

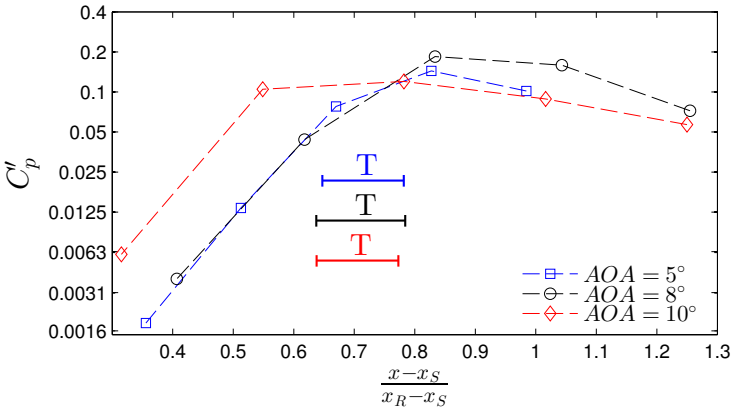

Figure 5.10: Root-mean-square of pressure fluctuations for bandpass-filtered signals plotted along separation bubble length at $AOA = 5°$, $8°$, and $10°$.

The development of the magnitudes of pressure minima along the airfoil is presented in Fig. 5.11, and plotted along the separation bubble length in Fig. 5.12, where the bars represent plus and minus one standard deviation of the pressure magnitudes. Since the magnitude of the pressure fluctuations depends both on the strength of the structures and their proximity to the surface, the variation of the magnitude of the minima reflects the combined effect of the changes in vortex height and strength along the separation bubble. The growth and then decay of the minima reflects a trend comparable to the trends in C_p' in Figs. 5.9-5.10, where there is a region of exponential growth, followed by reduced growth, and then decay. The standard deviation of the minima is approximately half of the mean magnitude of the minima. At $AOA = 5°$, the mean magnitude of the minima develops to a maximum magnitude at $x/c = 0.47$, which is downstream of mean transition. The location of the largest magnitude of minima and standard deviation varies from the microphone just downstream of transition at $AOA = 5°$ and $10°$ to the vicinity of reattachment at $AOA = 8°$. The growth rate shown in Fig. 5.12 is very similar between $AOA = 5°$, $8°$ and $AOA = 10°$, and these growth rates all begin to decrease at approximately $C_p' = 0.1$. The decreased growth at $AOA = 10°$ may be a result of the increased levels of vortex merging being the cause of growth in fluctuating pressure at this angle. Nevertheless, the peaks in the magnitudes of the minima come upstream of reattachment in spite of the vortices being expected to be closest to the surface at reattachment. This suggests that roll-up has completed as the vortices have pinched off from the shear layer upstream of reattachment.

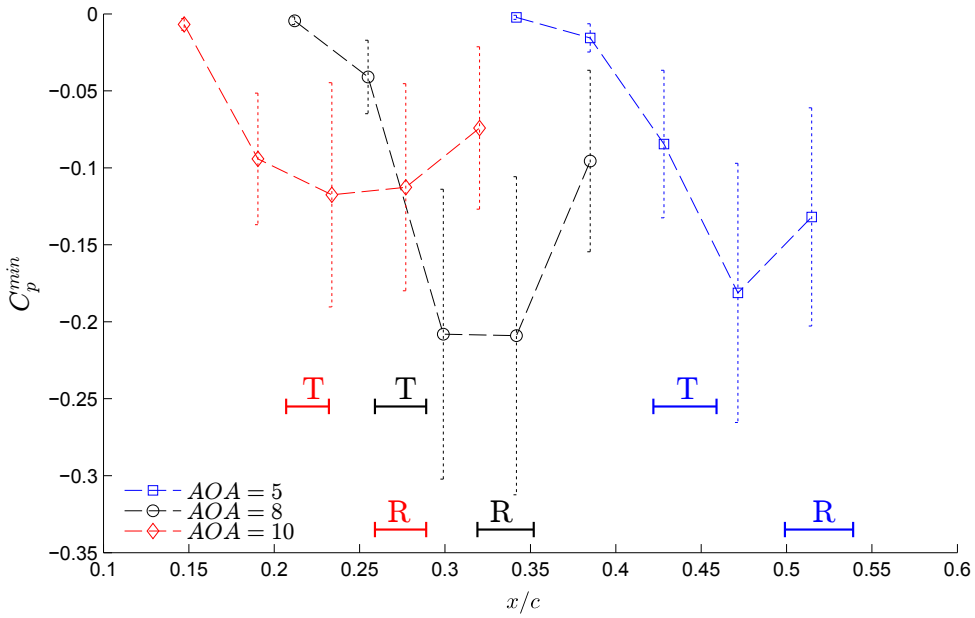

Figure 5.11: Development of amplitudes of pressure minima along the airfoil at angles of attack of 5°, 8°, and 10°.

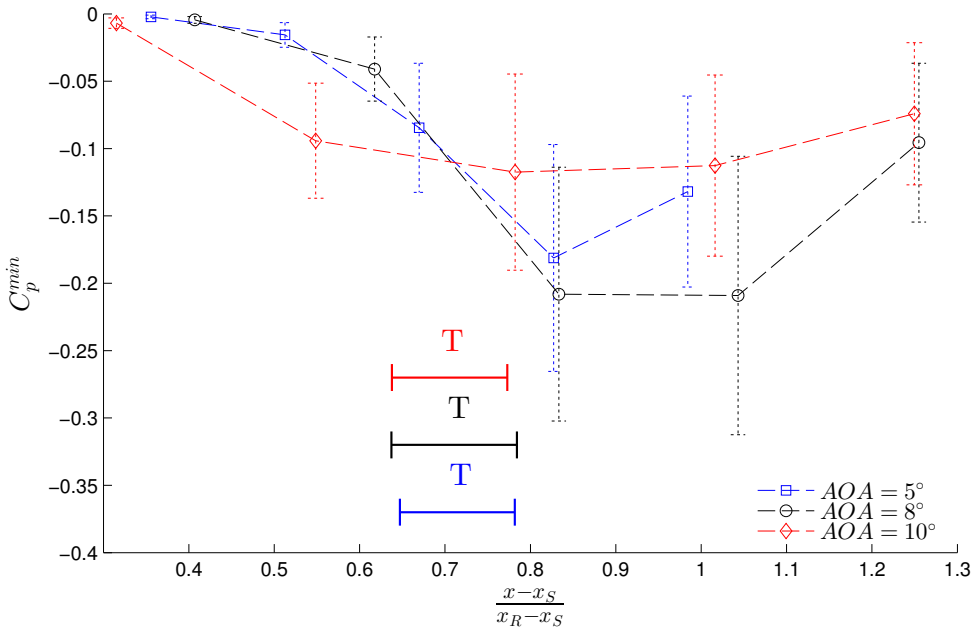

Figure 5.12: Development of amplitudes of pressure minima along normalized separation bubble length at angles of attack of 5°, 8°, and 10°.

The temporal variation in magnitudes of minima produced by individual vortices is shown in Figs. 5.13a-5.15a for $AOA = 5°$, $8°$, and $10°$. The red and green dots indicate that magnitude of the pressure minimum decreased or increased respectively from the minimum associated with the vortex upstream. The blue line exponentially interpolates the points between microphones where the magnitudes would cross $C_p = -0.025$. The threshold of $C_p = -0.025$ was chosen to best illustrate the temporal variation of the pressures. The variation in the position of the interpolated pressure for the tracked minima shows temporal changes in the development of disturbances. Additionally, the cases where merging occurs tend to be accompanied by the blue interpolation line moving further downstream, such as at $t = 364$ ms in Fig. 5.13a, $t = 748$ ms in Fig. 5.14a, and $t = 373$ ms in Fig. 5.15a. The delay in the interpolation location is speculated to be related to the vortices being displaced from the surface during merging, as seen in Fig. 4.13. For $AOA = 5°$ in Fig. 5.13b, the pressure magnitudes typically increase up to $x/c = 0.43$ or $x/c = 0.47$ which is downstream of transition. At $AOA = 8°$ (Fig. 5.14b) and $AOA = 10°$ (Fig. 5.15b) vortices also typically increase up to transition at $x/c = 0.33$ and $x/c = 0.27$ respectively. The trends for whether the individual magnitudes increase or decrease are plotted along the separation bubble length in Fig. 5.16. This shows that half of the pressure minima associated with the vortices have decreased by reattachment. The reduction in pressure magnitude indicates that vortices have completed roll-up, and have begun to break down as seen in the flow visualizations in Figs 5.2-5.4.

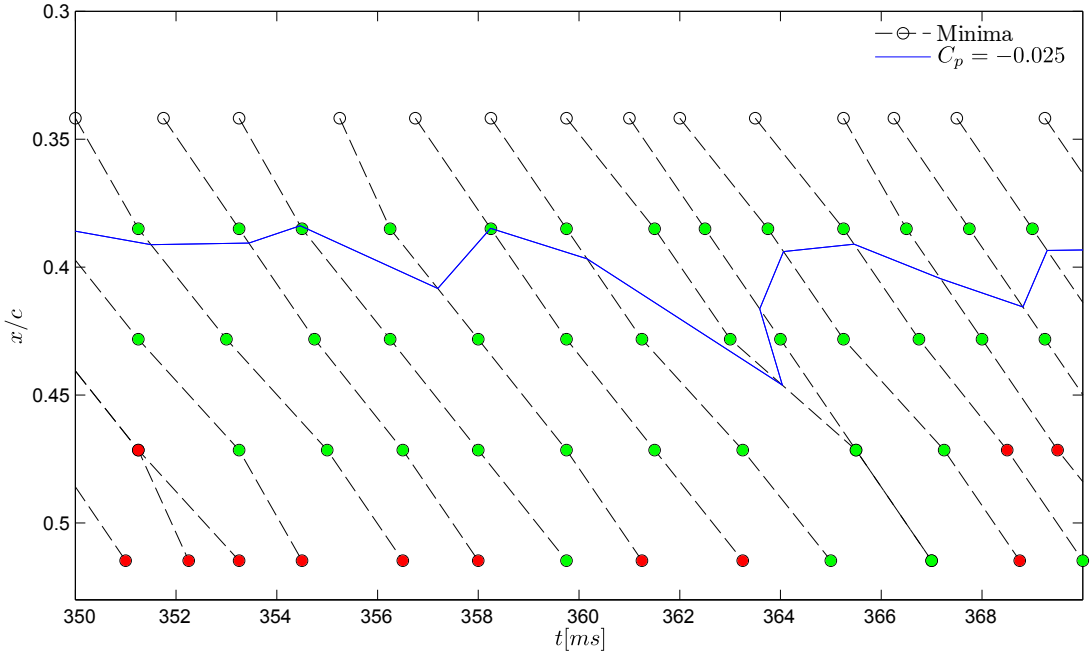

(a)

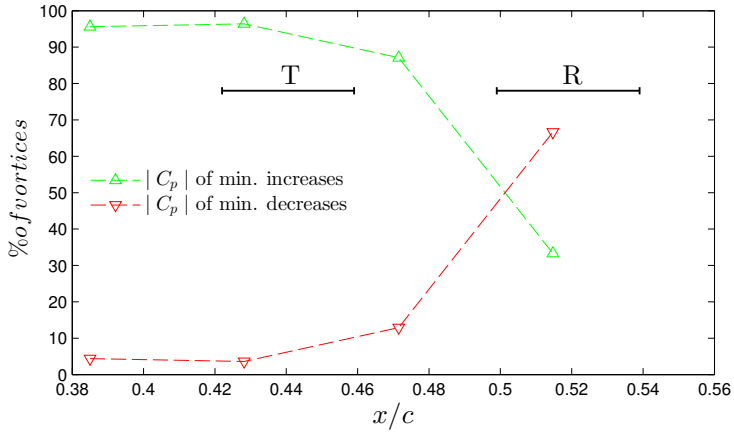

(b)

Figure 5.13: Tracking of vortices and magnitudes of pressure minima along the separation bubble at $AOA = 5°$. A green circle indicates an increase in the magnitude of the minimum (more negative) while a red circle shows a decrease. The blue line exponentially interpolates where the pressure minima would reach a threshold value of $C_p = -0.025$. The percent of vortices whose magnitudes decrease from the upstream location is presented for $AOA = 5°$ in (b).

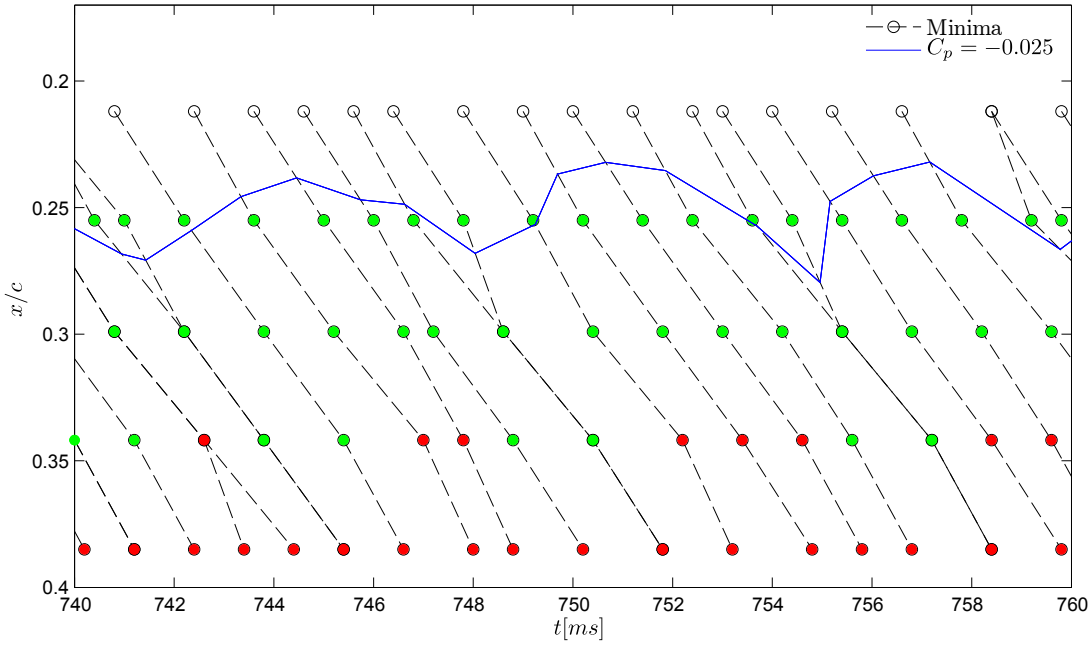

(a)

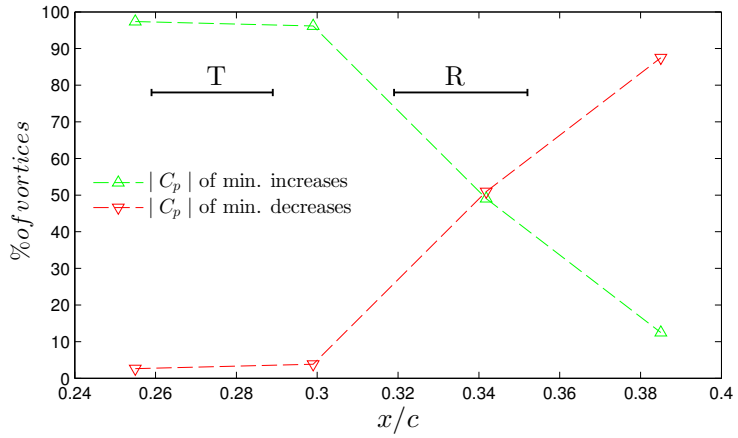

(b)

Figure 5.14: Tracking of vortices and magnitudes of pressure minima along the separation bubble at $AOA = 8°$. A green circle indicates an increase in the magnitude of the minimum (more negative) while a red circle shows a decrease. The blue line exponentially interpolates between the pressure minima to show where the pressure would reach a threshold value of $C_p = -0.025$. A summary of the percent of vortices whose magnitudes decrease from the upstream location along the separation bubble is presented for $AOA = 8°$ in (b).

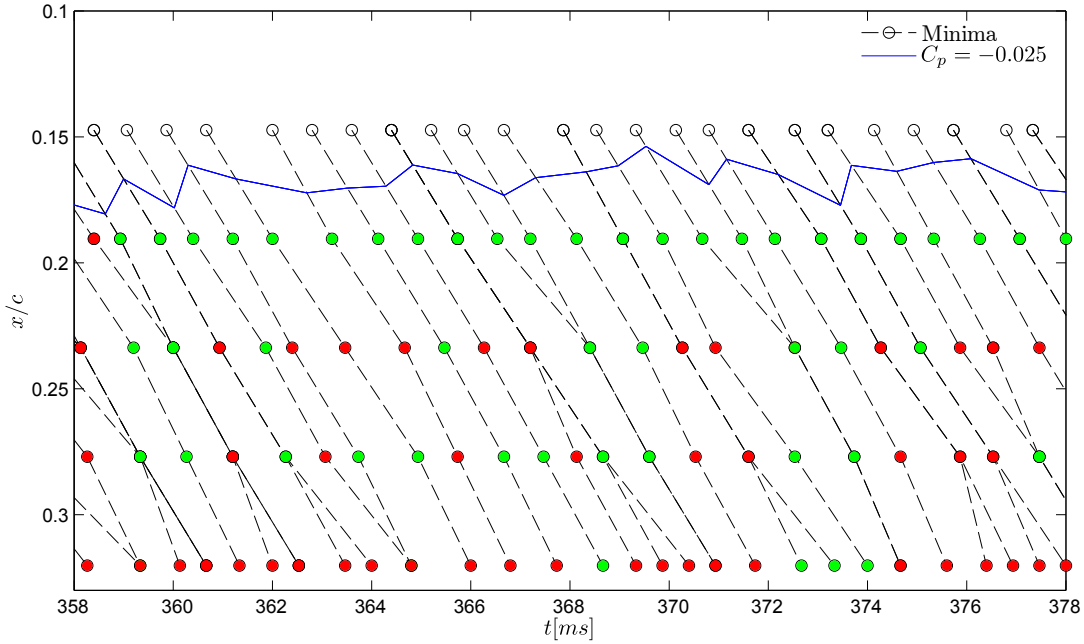

(a)

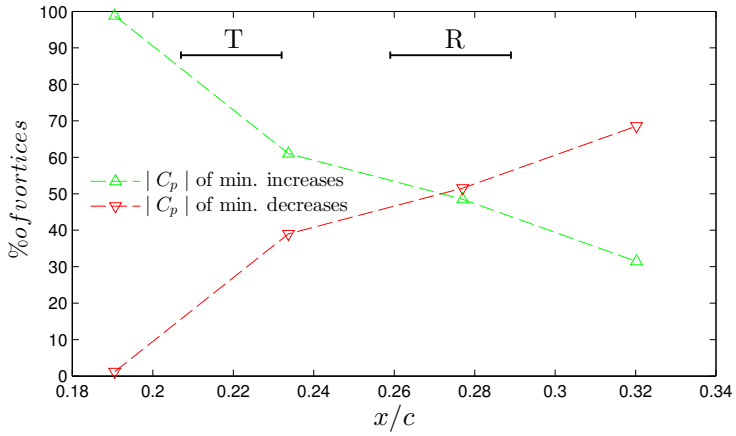

(b)

Figure 5.15: Tracking of vortices and magnitudes of pressure minima along the separation bubble at $AOA = 10°$. A green circle indicates an increase in the magnitude of the minimum (more negative) while a red circle shows a decrease. The blue line exponentially interpolates between the pressure minima to show where the pressure would reach a threshold value of $C_p = -0.025$. A summary of the percent of vortices whose magnitudes decrease from the upstream location along the separation bubble is presented for $AOA = 10°$ in (b).

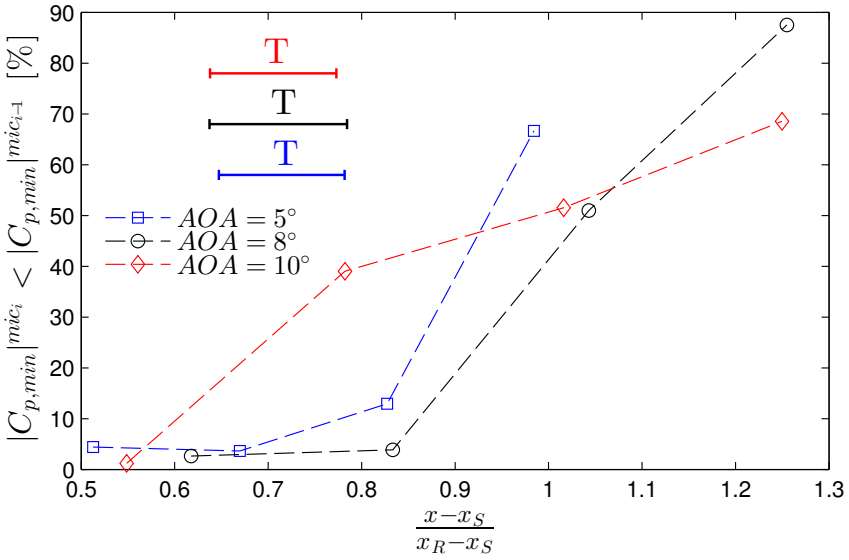

Figure 5.16: Summary of percent of vortices whose magnitudes decrease from the upstream location along the separation bubble, presented for $AOA = 5°$, $8°$, and $10°$.

The variation in vortex spacing between cycles is reflected in the time intervals between detected vortices, illustrated in Figs. 5.17-5.19 for $AOA = 5°, 8°$, and $10°$. These intervals tend to be closely-distributed where vortex rollers emerge, and become more broadly distributed as the structures interact. Where the vortices have begun to roll up (Figs. 5.17a,5.18a, and 5.19a) the intervals are normally distributed around 1.6 ms at $AOA = 5°$, 1.1 ms at $AOA = 8°$, and 0.8 ms at $AOA = 10°$. As the vortices progress along the separation bubble in Figs. 5.17b, 5.18b, and 5.19b, some may merge, which results in a shift of the distribution to longer intervals. The average interval also increases to 1.7 ms at $AOA = 5°$, 1.2 ms at $AOA = 8°$, and 0.9 ms at $AOA = 10°$. Past reattachment in Figs. 5.17c, 5.18c, and 5.19c, the effect of vortex merging is visible in the emergence of peaks at higher intervals between vortices. This second peak is visible as a hump in the distribution at $t = 2.0$ ms, in Fig. 5.17c at $AOA = 5°$, and the hump becomes more prevalent at larger AOA. There is a pronounced hump at $t = 1.4$ ms at $AOA = 8°$ in Fig. 5.18c, and at $t = 1.2$ ms at $AOA = 10°$ in Fig. 5.19c. The average intervals at these locations decrease to 1.6 ms at $AOA = 5°$, 1.1 ms at $AOA = 8°$, and 0.8 ms at $AOA = 10°$. The decrease in the average interval is due to the breakdown of the vortices resulting in more structures at smaller length scales and thus, higher frequencies. The changes in the distribution of intervals along the normalized separation bubble length are presented in Fig. 5.20. The time intervals and standard deviations are normalized by the respective maximum values at each angle of attack. At all of the angles studied, the standard deviation is greatest near mean transition, around 0.8 of the separation bubble length. Decreases in kurtosis indicate a flatter distribution produced by the bi-modal distribution caused by vortex merging. Positive skewness shows an increase in the distributions towards the tails at higher time intervals. Kurtosis and skewness decrease past mean transition which indicates the greatest impact of merging on the distribution before breakdown reduces the average interval. The double peaks in the intervals are reduced past reattachment where the proximity of the wall inhibits the cross-stream motion that accompanies vortex merging [87].

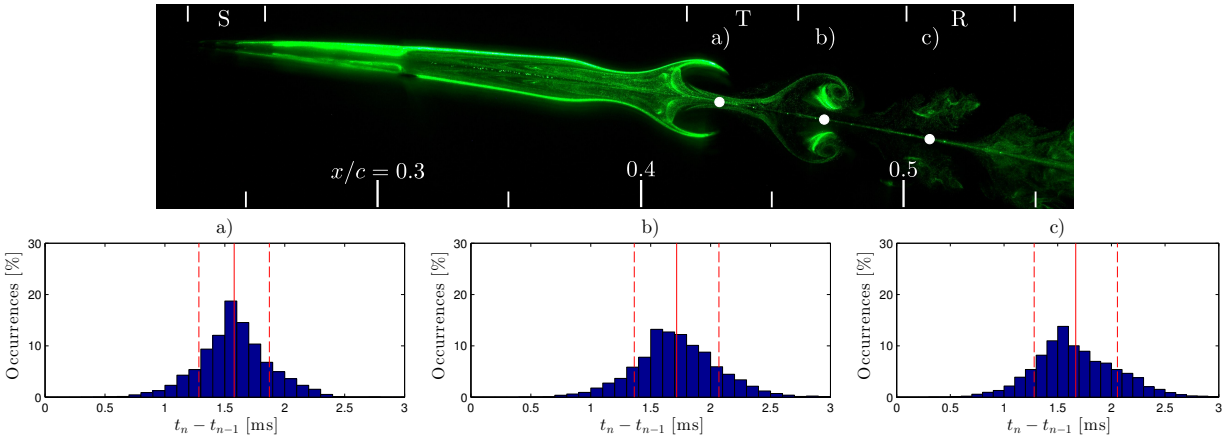

Figure 5.17: Time intervals between consecutive vortices at the microphone locations (a-c) indicated by the white circles for an angle of attack of 5°. The solid red lines on the distributions of the intervals indicate the average time interval and the dashed red lines indicate plus and minus the standard deviation.

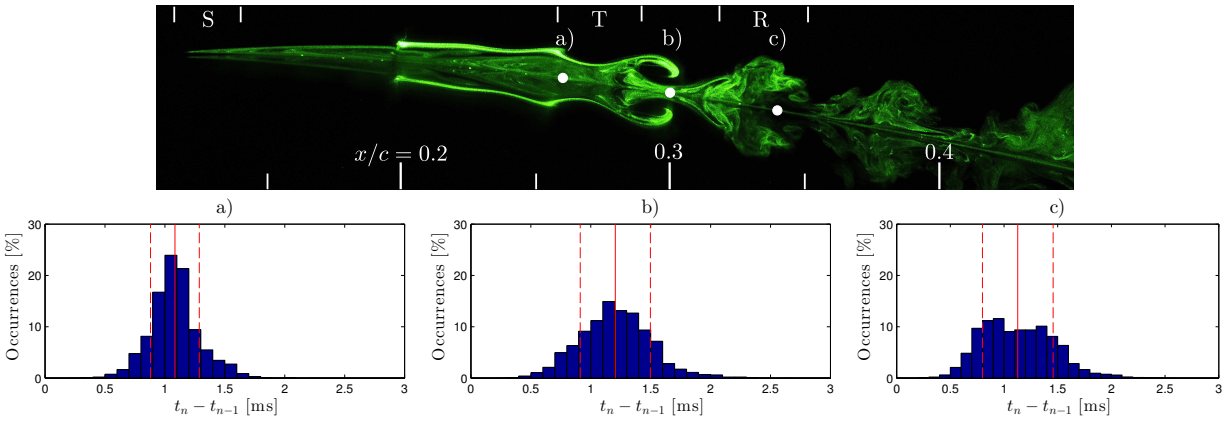

Figure 5.18: Time intervals between consecutive vortices at the microphone locations (a-c) indicated by the white circles for an angle of attack of 8°. The solid red lines on the distributions of the intervals indicate the average time interval and the dashed red lines indicate plus and minus the standard deviation.

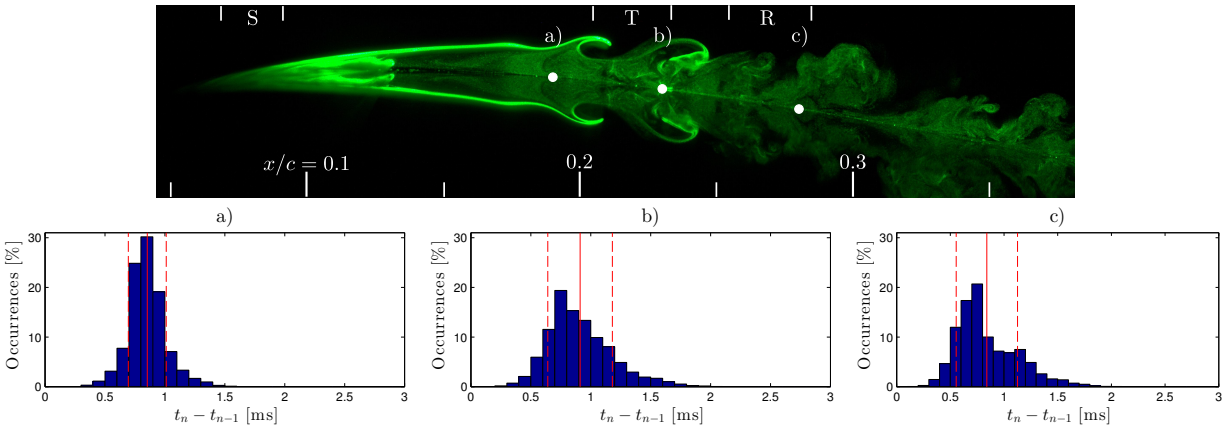

Figure 5.19: Time intervals between consecutive vortices at the microphone locations (a-c) indicated by the white circles for an angle of attack of 10°. The solid red lines on the distributions of the intervals indicate the average time interval and the dashed red lines indicate plus and minus the standard deviation.

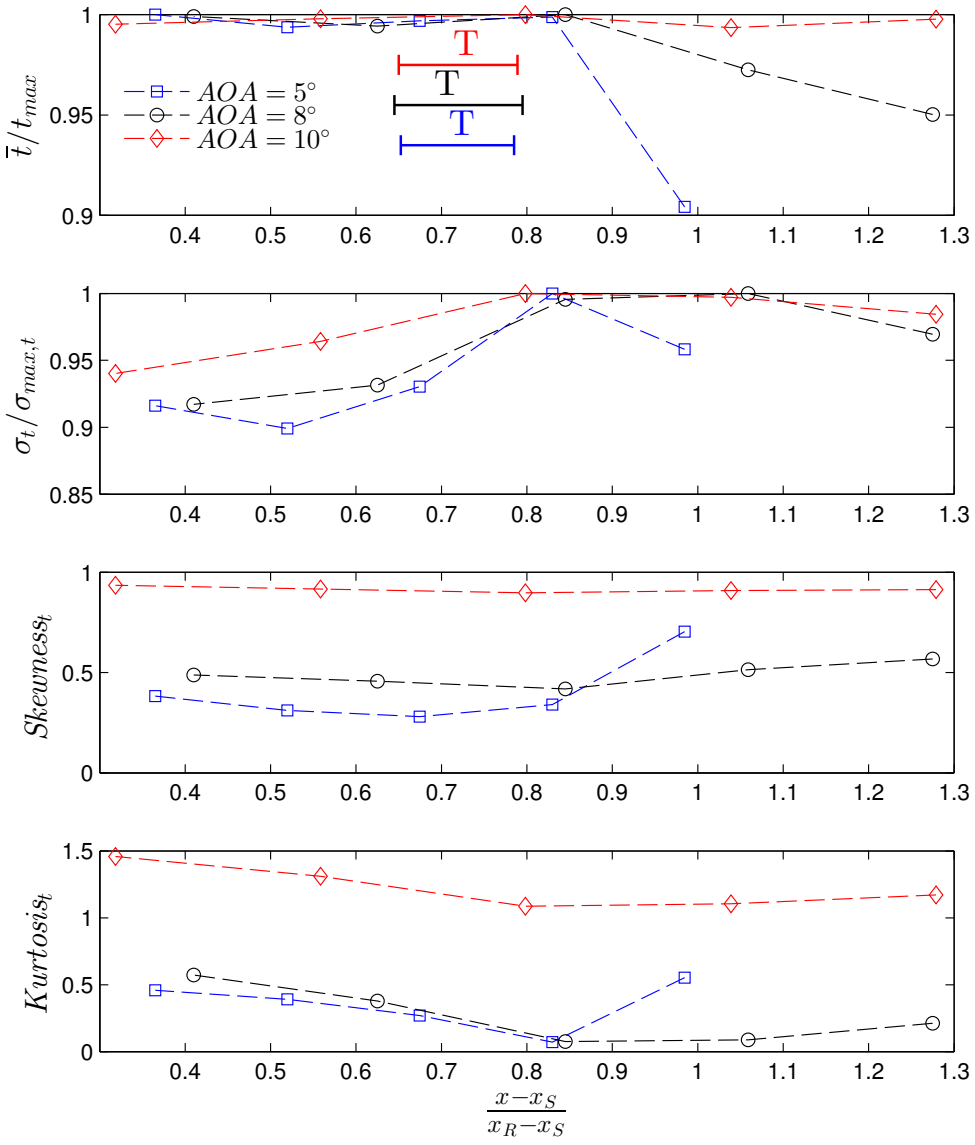

Figure 5.20: The development of the time interval distributions for $AOA = 5°$, $8°$, and $10°$. The average interval and standard deviations are normalized by the maximum value at each angle of attack.

Distributions of convective velocities for the vortices are presented in Figs. 5.21, 5.22, and 5.23 for $AOA = 5°$, $8°$ and $10°$. Initially these velocity distributions are narrow, but show greater variation as vortices displace within the mean flow and interact with each other. Upstream of transition in Figs. 5.21a, 5.22a, and 5.23a, the velocities are closely packed at half of the local edge velocity. Where the vortices are well-defined, Figs. 5.21b, 5.22b, and 5.23b, their velocities begin to spread, particularly towards lower speeds. This decrease in velocity was seen in merging sequences (Fig. 4.13) and the model of merging in Fig. 4.15, where the leading vortex is slowed during a merge. This also leads to a lower average convective velocity. Where the vortices break down, Figs. 5.21c, 5.22c, and 5.23c, the convective velocities become more spread, which is particularly noticeable at $10°$. The changes in convective velocity along the separation bubble are summarized in Fig. 5.24. The distributions of convective velocity become broader towards reattachment. The mean convective velocity relative to the edge velocity also increases as the as the structures convect within the redeveloping turbulent boundary layer.

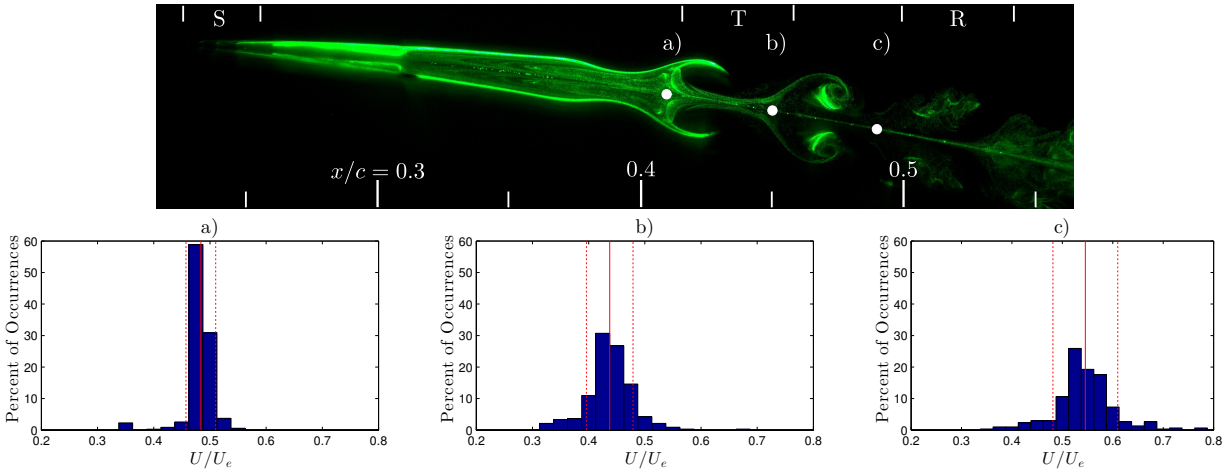

Figure 5.21: The distributions of convective velocities for vortices at $AOA = 5°$. The velocities in a)-c) are calculated for the points indicated by white circles which mark the mid-point between consecutive microphones. The solid red lines show the average convective velocities of the vortices while the dashed red lines show plus and minus one standard deviation.

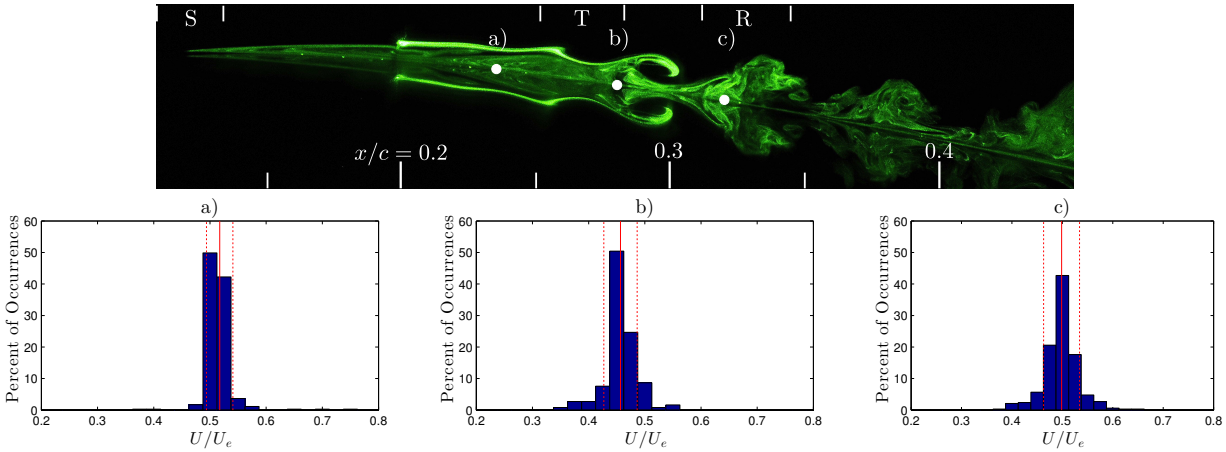

Figure 5.22: The distributions of convective velocities for vortices at $AOA = 8°$. The velocities in a)-c) are calculated for the points indicated by white circles which mark the mid-point between consecutive microphones. The solid red lines show the average convective velocities of the vortices while the dashed red lines show plus and minus one standard deviation.

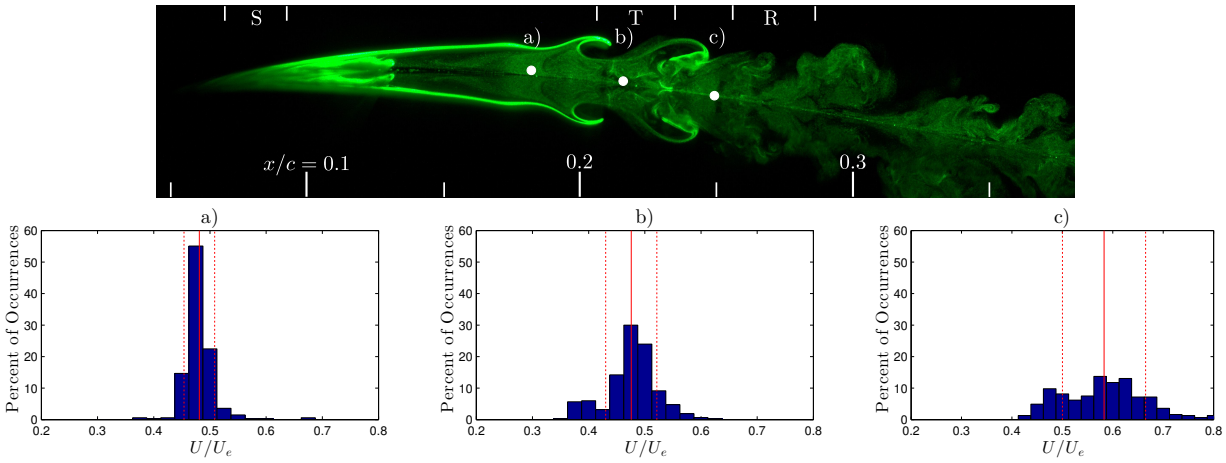

Figure 5.23: The distributions of convective velocities for vortices at $AOA = 10°$. The velocities in a)-c) are calculated for the points indicated by white circles which mark the mid-point between consecutive microphones. The solid red lines show the average convective velocities of the vortices while the dashed red lines show plus and minus one standard deviation.

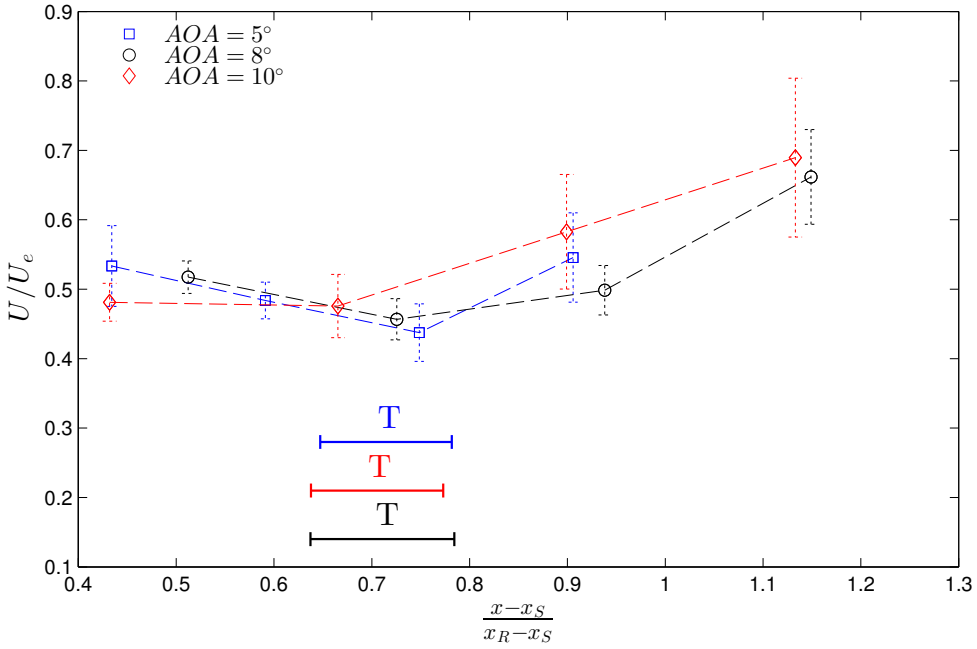

Figure 5.24: The distributions of convective velocities for vortices at $AOA = 5°$, $8°$, and $10°$, presented along the normalized bubble length. The bars indicate plus and minus one standard deviation.

A continuous wavelet transform analysis using a Marr wavelet [100] was used to identify temporal variations in the frequency of the pressure fluctuations. The results of the wavelet transform at $AOA = 5°$, $8°$, and $10°$ are shown in Figs. 5.25-5.27 respectively for the signals high-pass filtered at 125 Hz. These figures demonstrate how the signals progress from activity around a central frequency to one with occasional lower-frequency excursions, and then show an increase in high-frequency content. This progression from a central to lower, then higher frequencies accompanies the evolution of vortices, their merging, and their eventual breakdown. Upstream of mean transition, Figs. 5.25a, 5.26a, 5.27a, the peaks and troughs in the wavelet transform exhibit temporal variations in the frequency of the peaks, while the average frequency changes between AOA. The frequencies of the peaks fall within the amplified band of disturbances identified from power spectra in Figs. 5.8(a)-5.8(c). At $AOA = 5°$ (Fig. 5.25a) these peaks range between $f = 550Hz$ and $f = 700Hz$. At $AOA = 8°$ (Fig. 5.26a) the frequency range is between $f = 800Hz$ and $f = 1000Hz$. In Fig. 5.27a at $AOA = 10°$ the peaks are visible between $f = 1000Hz$ and $f = 1200Hz$. Past transition, Figs. 5.25b, 5.26b, 5.27b, the variation in frequencies of the peaks increases and activity emerges at a subharmonic of the original central frequency as vortices merge. For example, at $t = 983$ ms in Fig. 5.25b, the minima around $f = 600Hz$ join into a single minimum at $f = 600Hz$. The peaks near the central frequency are present at $AOA = 8°$ in Fig. 5.26b), with the negative peaks spreading to $f = 600Hz$ and $f = 1000Hz$. At $AOA = 10°$ in Fig. 5.27b), many of the peaks present around $f = 1100Hz$ merge into peaks near $f = 500Hz$, such as at $t = 522$ and 524 ms. As the vortices break down near reattachment, the peaks taper off into multiple tails at higher frequencies. These cases are shown in Fig. 5.25c at $t = 979ms$, Fig. 5.26c at $t = 785ms$, Fig. 5.27c at $t = 523ms$. The changes in the frequency scales with time and location reflect the merging and breakdown of the individual vortices with excursions in activity to lower and higher frequencies, respectively.

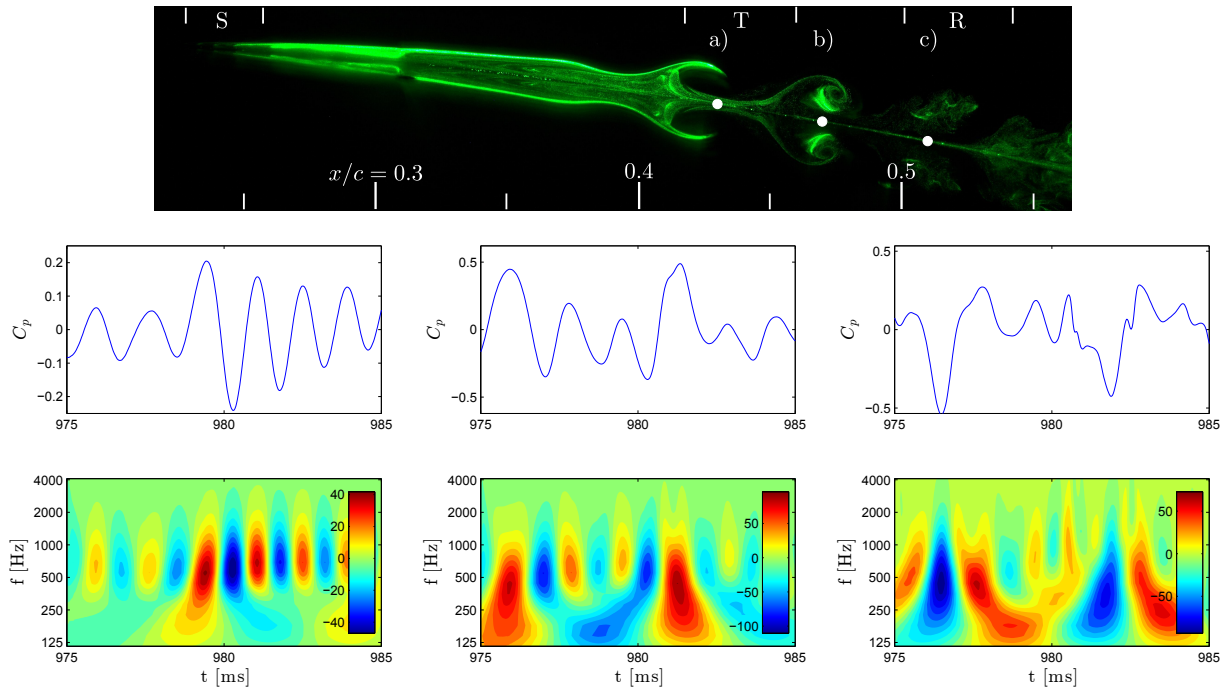

Figure 5.25: For an angle of attack of 5°, microphone signals and their accompanying continuous wavelet transform are presented along the separation bubble. The microphone locations are indicated with the white dots and a)-c) markers.

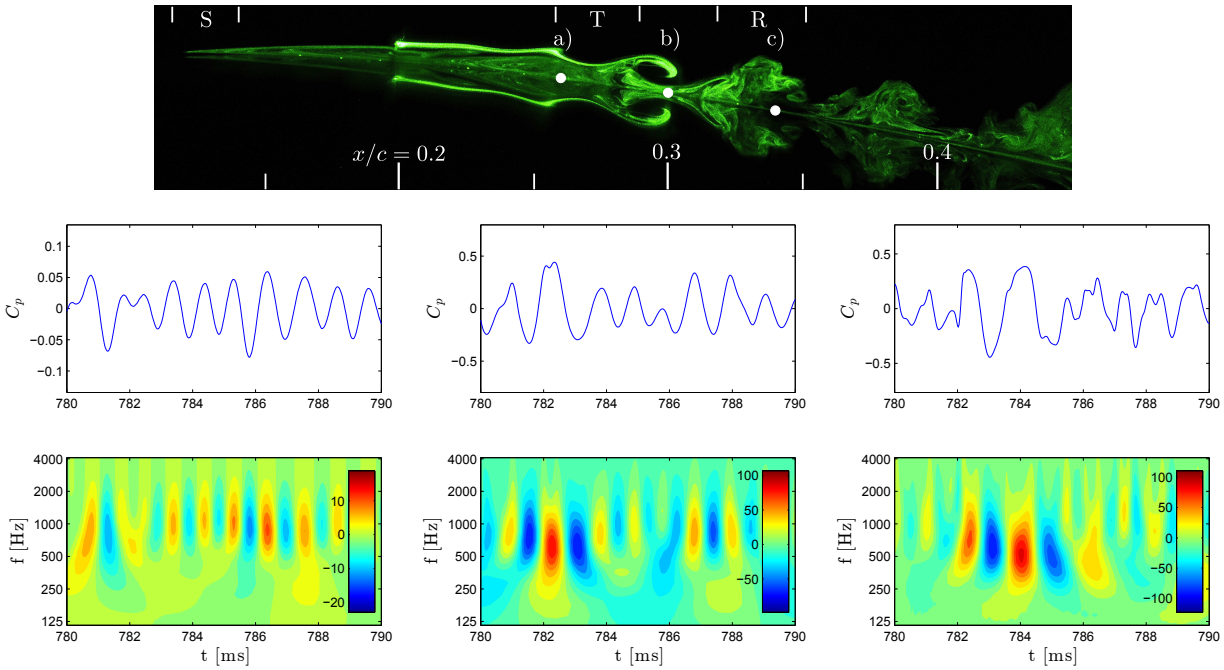

Figure 5.26: For an angle of attack of 8°, microphone signals and their accompanying continuous wavelet transform are presented along the separation bubble. The microphone locations are indicated with the white dots and a)-c) markers.

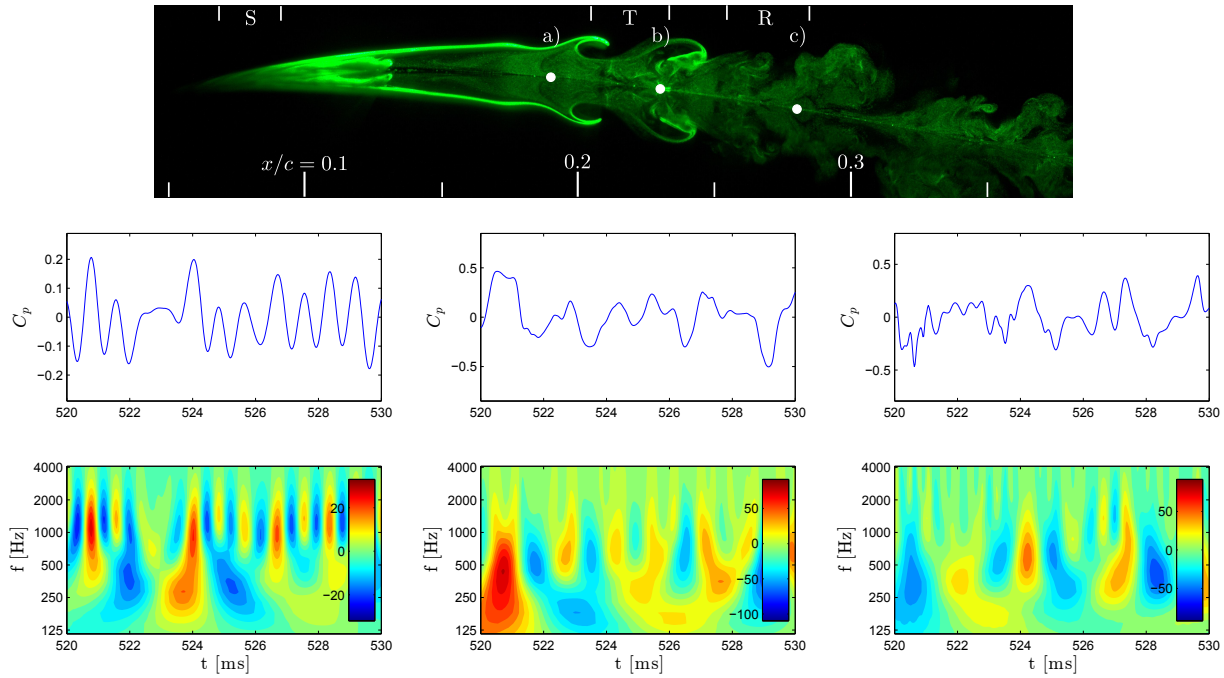

Figure 5.27: For an angle of attack of 10°, microphone signals and their accompanying continuous wavelet transform are presented along the separation bubble. The microphone locations are indicated with the white dots and a)-c) markers.

5.3 Vortex Merging Comparison

Analysis of flow visualization records revealed that merging occurs at different intervals at the selected angles of attack. The change in the relative number of vortices that merge, obtained from vortex tracking, is shown along the separation bubble is presented in Fig. 5.28. The same data are plotted in Fig. 5.29 for the normalized separation bubble length. The vortices merge over a range of x/c that is centered around mean transition. Merging begins where the vortices have rolled up upstream of mean transition, which is $x/c = 0.39$ at $AOA = 5°$, $x/c = 0.26$ at $AOA = 8°$, and $x/c = 0.18$ at $AOA = 10°$. The rate of merging reduces past mean reattachment in all of these cases, especially at $AOA = 5°$ and $8°$. The overall percentage of vortices involved in merging increases from 10% at $AOA = 5°$, to 25% at $AOA = 8°$, and 70% at $AOA = 10°$. From the flow visualizations in Figs. 5.2-5.4, the height of the reverse flow region is larger compared to the spacing of the vortices at $AOA = 10°$. In addition, the vortices develop more quickly, which combines with the greater proportional separation from the wall to delay the attenuation of merging caused by the wall. The progression of merging is plotted on the same scale in Fig. 5.28, and $AOA = 8°$ and $10°$ show a similar spatial rate of merging at their greatest slope. As a result, the increased momentum transfer due to merging at the higher angles of attack allows the flow to reattach in spite of the greater bubble height and airfoil curvature.

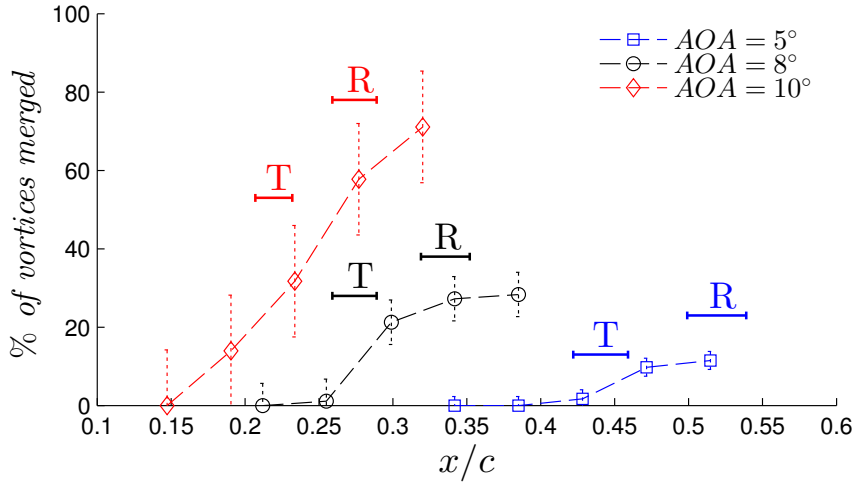

Figure 5.28: Progression of percentage of merged vortices along the airfoil, for $AOA = 5°$, $8°$, and $10°$.

Figures 5.30a, 5.30b, and 5.30c show a sequence of vortices detected at the microphone

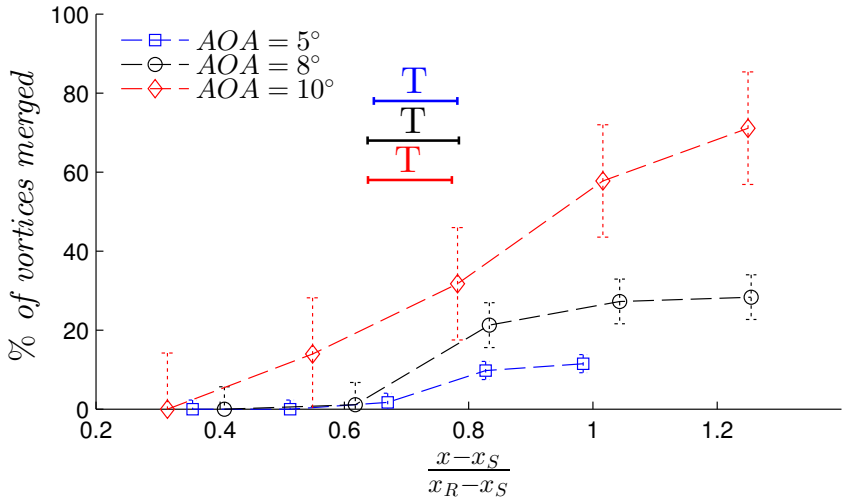

Figure 5.29: Progression of percentage of merged vortices along the normalized position within the separation bubble, for $AOA = 5°$, 8°, and 10°.

location closest to roll-up. The vortices are coloured depending on whether they merge at any point downstream. The distributions of numbers of vortices between the first vortices of consequent merging pairs are summarized in Figs. 5.31a-5.31c. These figures show the intermittent nature of the vortex merging, where merging occurs separated by varying numbers of non-merging vortices. At $AOA = 5°$, (Figs. 5.30a and 5.31a), 1 to 20 vortices occur between merging pairs, with a peak around 3 vortices. An angle of attack of 8°, (Figs. 5.30b and 5.31b), there is a similar range to $AOA = 5°$ from 1 to 20 vortices between merges, with peaks around 2 and 5 vortices. The increased frequency of merging at 10° is accompanied by the shorter intervals seen in Figs. 5.30c and 5.31c. The intervals are below 10 vortices, with peaks at intervals of 2 and 4 vortices.

To investigate a possible underlying periodicity in the occurrence of vortex merging, a temporal sequence involving approximately 100 vortices was converted into a time series by using an interpolation technique. A spectrum analysis was performed on the resulting sequence, and the results for $AOA = 5°$, 8°, and 10° are illustrated in Figs. 5.32a, 5.32b, and 5.32c, respectively. These power spectra show activity at a range of frequencies. At $AOA = 5°$ in Fig. 5.32a, there are some peaks at approximately 1/4, 1/6, and 1/8 of the mean vortex shedding frequency, which is the same range of the intervals between vortices in Fig. 5.31a. At $AOA = 8°$ in Fig. 5.32b there is a peak at around 1/5 of the vortex shedding frequency, matching the peak at an interval of 5 vortices between merges in Fig. 5.31b. The angle of attack of 10° shows a peak around 1/4 and 1/6 of

the shedding frequency in Fig. 5.32c, with shorter intervals in 5.31c falling outside of the frequency range of this analysis. Between the angles of attack there is limited similarity in the frequencies of merging. The wind tunnel resonances do not fall below 190 Hz and are hence not responsible for most of the frequencies of vortex merging. The frequency content of vortex merging changes between all of these angles of attack. The frequency of merging at these AOA is dependent on the AOA and is not dictated by a dominant factor in the disturbance environment.

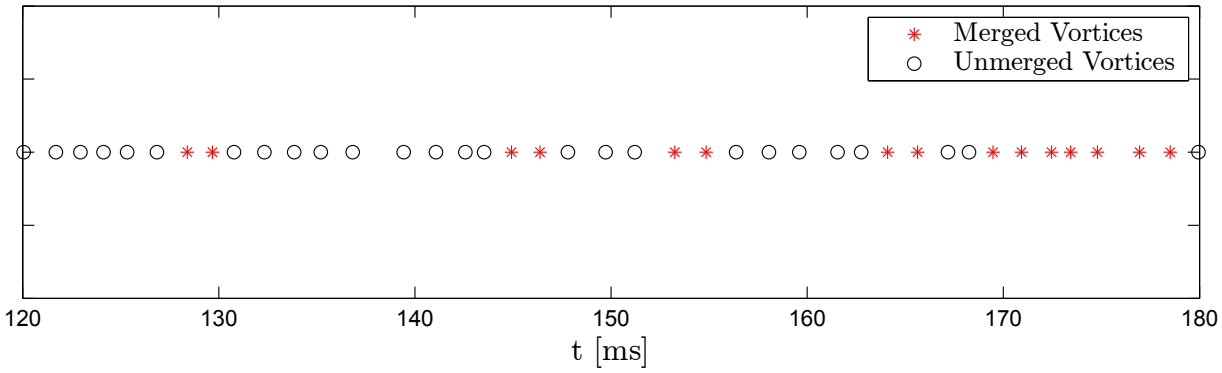

(a) $AOA = 5°$

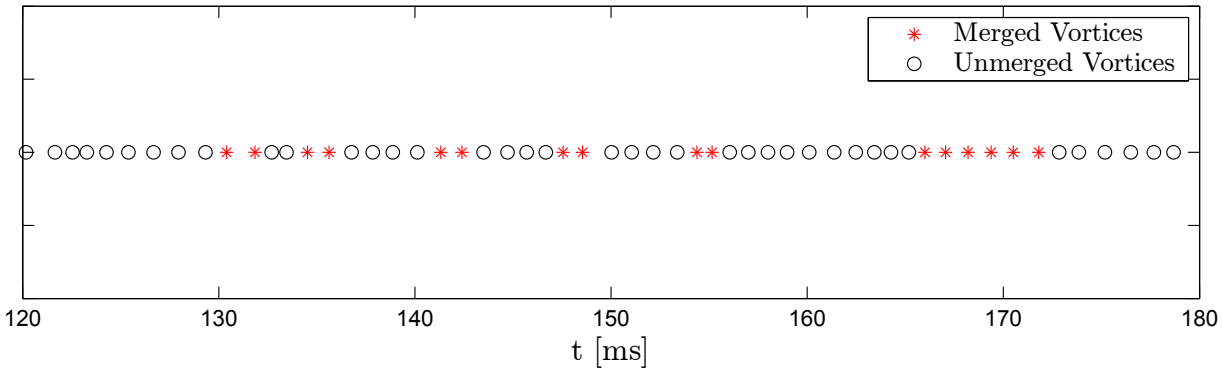

(b) $AOA = 8°$

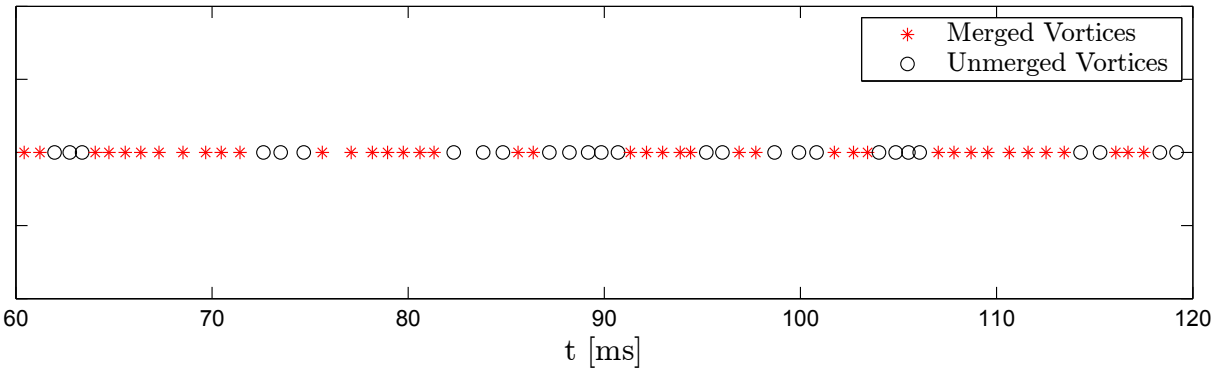

(c) $AOA = 10°$

Figure 5.30: Time sequence of detected vortices at the most upstream location for angles of attack of 5°, 8°, and 10°. The symbols of the vortices indicate whether they merge downstream of their initial detection.

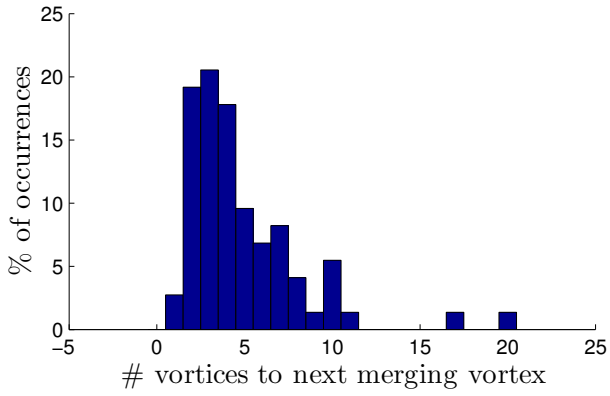

(a) $AOA = 5°$

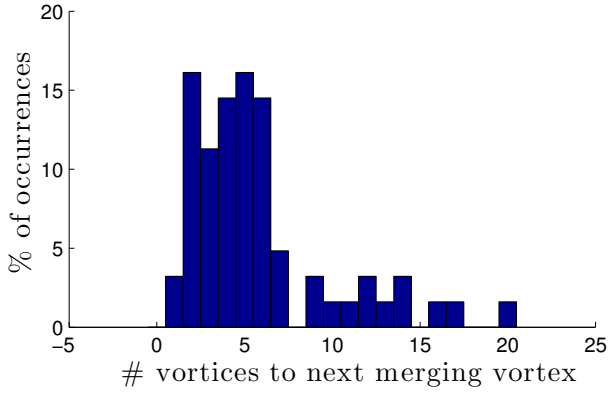

(b) $AOA = 8°$

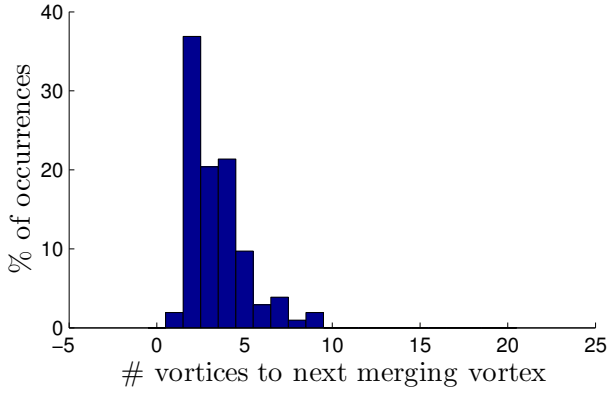

(c) $AOA = 10°$

Figure 5.31: Intervals of vortices between merging events in Fig. 5.30a-5.30c.

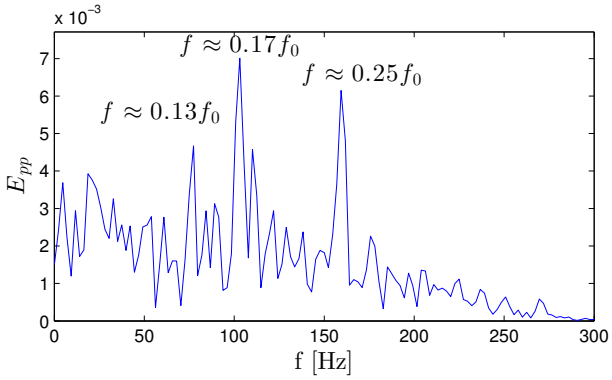

(a) $AOA = 5°$

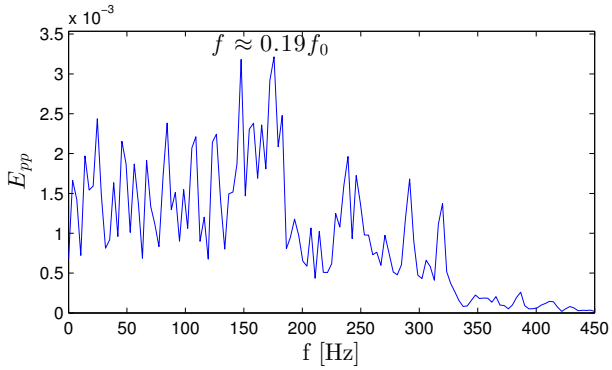

(b) $AOA = 8°$

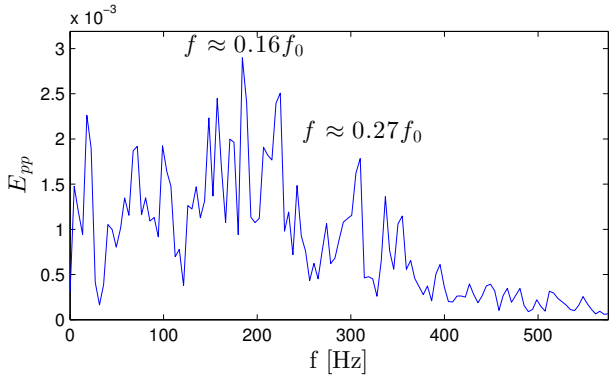

(c) $AOA = 10°$

Figure 5.32: Power spectra of the merging time sequences of over 200 vortices sampled in Fig. 5.30a-5.30c, interpolated for an even sampling rate.

Chapter 6

Conclusions

The evolution of structures within the LSB over a NACA 0018 airfoil at a chord Reynolds number of 100,000 was investigated experimentally at $AOA = 0°$, $5°$, $8°$, and $10°$. These structures were found to exhibit a range of characteristic scales and behaviours. There were two main goals of the investigation: first, relate the flow structures to the fluctuating pressures measured at the surface to develop a method to quantify vortex dynamics solely based on the surface pressure signals; second, to apply this method to the different angles of attack investigated and gain insight into how the vortex dynamics changes with conditions at the separation bubble.

The development of structures within the LSB was investigated using mean and time-resolved methods. Mean surface pressures along the chord of the airfoil located the separation bubbles at the angles of attack investigated. Embedded microphones were used to capture the development of pressure fluctuations along the airfoil. A high-speed separation bubble visualization method was used to track the development of flow structures within the LSB. The direct link between flow structures and surface pressure signals was investigated by synchronizing the high-speed visualizations with simultaneously-acquired microphone measurements.

6.1 Flow Physics

Smoke visualizations of the laminar separation bubble were performed to investigate the development of flow structures at $AOA = 8°$. These visualizations found the persistent formation of vortices over the suction side of the airfoil. Mean surface pressure

measurements were used to identify the mean locations of separation, transition, and reattachment on these visualizations. A temporal average of smoke visualizations showed the reverse-flow region near the wall, similar to the classical schematic of separation bubble topology. The increased momentum transfer due to turbulence is shown with the smoke streaklines becoming dispersed near transition, then diffusing towards the airfoil. These visualizations confirmed the estimates of the points of separation and reattachment from the mean pressure measurements.

The sequences of smoke visualizations of structures were examined. They show that the vortices in the separation bubble develop from disturbances that grow as they are carried with the flow. These disturbances exhibit temporal variations in their spacing. The location where the vortices begin to roll up varies cycle-to-cycle, as does the location where these vortices begin to break down further downstream. High-speed sequences of flow visualization images show that these vortices may merge as they develop, similar to the merging seen in free shear layers [3] and previously found over backward-facing steps [52]. The vortices break down past reattachment, where merging is inhibited.

The top view image sequences show the spanwise development of the vortices. The initial disturbances show a two-dimensional growth and roll-up that occurs nearly simultaneously across the span of the airfoil. Towards mean transition, the structures begin to distort across the span as they begin to break down. Due to the developing three-dimensionality, the local microphone measurements are restricted to represent the local vortex activity across the span.

Embedded microphones were used to track the development of fluctuating pressures along the airfoil. These disturbances show an initial exponential growth to a maximum near mean transition, which then decays past reattachment. The microphone signals indicate the growth of a periodic signal, which becomes less regular as the flow develops along the separation bubble. The spectra of the signals illustrate that a band of disturbances grows and then spreads to higher and lower frequencies as it forms the broadband energy content expected of turbulence. This broadening in the band of frequencies mirrors the increasing variation in vortex spacing along the separation bubble.

Comparisons between flow visualizations and simultaneously acquired pressure signals found that the passage of a vortical structures over the embedded microphone accompanies a local minimum in the pressure signal [23]. The physical relationship between vortices and surface pressure minima was further substantiated by an inviscid simulation of vortices over a surface. The vortices in the simulation produce pressure minima on the surface immediately below the respective vortices, and a sequence of these vortices produces a periodic signal similar to that seen from the microphones. Hence, the minima can be used

to identify the structures solely based on the microphone signals.

Sequences of vortex merging and synchronized pressure signals show that the associated pressure minima approach each other and produce a single minimum for the merged structure. A potential flow simulation of the vortices over a flat surface replicated the merging of the surface pressure minima. In the simulation, the leading vortex moves towards the surface while the following vortex moves further away. The self-induced velocity of the vortex mirror pairs against the flow increases as they move towards the surface. When the vortices are the closest to the surface, it results in the near-stationary vortices as seen in merging sequences. In the experiment, the cross-flow velocity gradient amplifies the height offsets induced by the vortices and moves the vortices closer together. Thus, both the mean flow and the vortex induced velocities contribute to the merging of vortices. This follows the well-reported progression of merges in free shear layers [3, 4].

Vortices were tracked in a series of images to capture their dynamics and merging. This tracking showed the variability in convection speed of the vortices, as well as variation in the location where they merge. To track vortices using only the microphones, the signals were analyzed using pattern recognition as well as a cross-correlation technique. The pattern recognition algorithm required training that used the visual data tied with the microphone data to relate the features of the pressure signal to the activity of the flow structure passing over the microphone. Due to the similarities in some features between the classes of activity, this method was 90% accurate overall, but 60% accurate for detecting merges. A tracking method that cross-correlated segments of the signal between subsequent microphones was used, with segments centered where the vortices were expected to occur. In comparison with the visualization tracking, the cross-correlation vortex tracking accurately captured convective speeds, and is 80% accurate on vortex merging detection. This technique captures the individual vortex activity sufficiently accurately to be useful in determining the time-varying aspects of the vortex dynamics under different flow conditions, without the need for training the pattern recognition algorithm.

6.2 Vortex Dynamics Characterization

The analysis developed from the test case at $AOA = 8°$ was applied to characterize and compare the vortex activity at a smaller ($AOA = 5°$) and larger ($AOA = 10°$) angle of attack, with microphones unavailable at $AOA = 0°$. As the angle of attack increases, the initial structures become smaller and show increased cycle-to-cycle variations. The regular vortex merging at 0° becomes intermittent at 5°, more prevalent merging at 8°, and chaotic

merging at 10°. At higher angles the vortices exhibit more rapid spatial development and breakdown than at the lower angles.

From the mean surface pressure measurements on the airfoil, the locations of mean separation, transition, and reattachment on the airfoil were identified. The separation bubble moves upstream with increasing angle of attack due to the increased adverse pressure gradient following the larger suction peak, as found by Lee & Gerontakos [99]. The length of the separation bubble also shrinks as the structures develop more rapidly at the greater angles of attack [38]. The distance between transition and reattachment remains similar for the angles of attack studied here. The larger angles of attack have a greater pressure recovery after transition, which suggests greater momentum transfer is required for reattachment.

The surface pressure fluctuations change with angle of attack in response to the changes in the vortex dynamics. The rms of the pressure fluctuations all show an initial exponential growth to a maximum just downstream of mean transition. This agrees with what has been found in other separating-reattaching flows such as blunt-edged splitters [22] and fences [25]. Past this maximum of just over 10% of dynamic pressure, the pressures gradually decrease towards reattachment. The power spectra of the pressure fluctuations show a band of disturbances that are amplified and spread along the separation bubble. As the angle of attack is increased, the band of amplified frequencies shifts to higher frequencies. The spectra show growth at lower frequencies before breakdown. This has previously been attributed to vortex merging [52], which is confirmed with the flow visualizations of merging increasing with increasing angle of attack. Plotting the rms of pressure signals filtered around the amplified bands along the bubble length shows similar normalized exponential growth rates across the three angles of attack.

The magnitudes of the individual pressure minima associated with the vortices follow a trend similar to the rms of the pressure signals. The growth of the magnitudes of the peaks is exponential for a greater extent at the smaller angles of attack, and deviates further at higher angles of attack where merging is more prevalent. The minima reach their greatest magnitudes upstream of reattachment. The changes in minima for a single vortex were followed using the vortex tracking method. An increase to a maximum pressure minimum shows the completion of vortex roll-up, as the vorticity in the shear layer pinches off into a single vortex. The growth of magnitudes varies between cycles, with vortices that merge also showing a delayed growth in magnitudes. While the magnitudes of the vortices reach a maximum at reattachment, at this point around 50% of the vortices have begun to show a reduced magnitude, in spite of reattachment being expected to move the vortices closer to the wall. This decrease in magnitudes indicates that the vortices have begun to break down, and redistribute their energy to smaller scales as part of the transition to turbulence.

At individual microphones, the intervals between detected minima characterizes how the spacing between vortices changes along the separation bubble. The initial distributions of intervals is approximately normal, but the effect of merging broadens the distribution. When merging is more prevalent, this results in a bimodal distribution. As breakdown progresses, the distributions also skew towards the shorter intervals expected for the resulting smaller structures.

The vortex tracking algorithm developed in Section 4.4.2 measures the convective velocity of the vortices. The velocities have a narrow distribution centered at half of the edge velocity at the location where the vortices are forming along the bubble, similar to other studies on airfoils [95]. This velocity distribution broadens as vortices approach each other and merge. Velocities of the vortices also increase relative to the edge velocity past reattachment as the vortices convect within the redeveloping turbulent boundary layer. The convective speeds of the individual vortices are hence influenced by merging and the increasing chaos within the transitioning flow.

Continuous wavelet transforms capture the changes in the instantaneous frequency content of the signal, and shows the range of intervals experienced in sequences of vortices. Initially the wavelet transforms show that the vortex activity varies within the amplified band measured from the power spectra. There are variations in the frequency content of the signals that increase as the vortices merge with each other around mean transition. Progressions of vortices to merging results in two minima near the original frequency joining into a single negative peak in the wavelet transform at a subharmonic of the original frequency. The individual vortices are seen to break down past reattachment, where the peaks at the main frequency split off into tails at higher frequencies as the vortices break down to smaller structures.

The vortex-tracking was employed to track the merging at the different angles of attack. Merging increases from 10% of the total vortices at $AOA = 5^\circ$ to 30% at $AOA = 8^\circ$, and 70% at $AOA = 10^\circ$. Merging progresses at its greatest rate within a region centered around mean transition. The visualizations show that this region occurs past the areas of roll-up for the vortices. Merging is strongly inhibited at reattachment for the cases of 5° and 8° as the vortices move closer to the airfoil surface. This effect is less at 10°, where the vortices have a closer spacing compared to their distance from the wall. Since vortex merging is associated with increased momentum transfer in shear layers, it is speculated that the trend of increased merging with increased angle of attack accommodates the greater pressure recovery required at the increasing angles of attack.

For any control strategy that introduces disturbances, the disturbances would be expected to impact both the frequencies of the vortices[71] and the periodicity of their merging

[4]. Hence, the periodicity of merging was investigated for these three cases. In all of the cases, merging occurs at a range of intervals, varying from a string of vortices that don't merge to periods of persistent merging. The sequences of merges and lack of merges were converted to time series and the power spectra of the results were obtained. All of the power spectra show a range of periodicity for merging, with most of the activity below 200 Hz for all of the cases. The merging occurs at a range of frequencies, as seen in the flow visualizations, rather than the more regular merging seen in shear layers [3] and flows over steps [52]. The range of frequencies present reflects that the transition process is due to the range of disturbances present in the environment, rather than disturbances introduced at a specific frequency as may be employed in a control strategy.

Chapter 7

Recommendations

Based on the conclusions presented in Chapter 6, the following recommendations are put forward.

1. While flow visualizations can provide some quantitative data about the vortices, it provides limited information about the velocities within the vortices. Simultaneous flow-field measurements along with microphone measurements should be performed to relate the vortex circulation and position independently to the pressure signals. PIV methods would be helpful for tracking vortices, instead of having to apply pattern recognition on the visualized structures.

2. The vortex dynamics in the separation bubble should be investigated in a parametric study. Previous experiments investigated how the position and length of the separation bubble changes with angle of attack and Reynolds number. The vortex-tracking method should be employed to study changes in vortex dynamics in the separation bubble, and how these relate to the airfoil performance. The changes in the LSB may be the result of different regimes of vortex interactions.

3. Since control strategies for LSBs often introduce disturbances, the vortex-tracking technique developed in this thesis should be applied to quantify how the disturbances introduced impact the vortex dynamics. Artificially introducing disturbances may change the frequency of vortices as well as their merging activity. The effects of the changes in vortex dynamics on airfoil performance should then be quantified.

4. Since the microphone spacing is currently on the order of the wavelength of the vortices, it is recommended that the spacing is decreased for any future models.

Decreasing the spacing below half of the vortex wavelength based on the Nyquist wave number would reduce the risk of spatial aliasing where vortices would appear to travel backwards if the signals weren't shifted before cross-correlation.

5. An alternate method of synchronizing the camera recordings and microphone measurements should be devised to make more data acquisition channels available for microphone measurements. The vortex tracking algorithm could be enhanced by expanding the range where microphones are measured, or increasing the spatial resolution if more than the current 5 channels of microphone measurements are available.

6. In the power spectra of the microphone signals, the resonances of the span and height of the wind tunnel test section are present. These disturbances also appear on earlier hot-wire measurements of the spectra over the airfoil, and these resonances and their harmonics occur within the amplified band of disturbances. If possible given constraints for optical access, these resonances from the hard walls should be reduced using acoustic panels or possibly by using an open jet in an anechoic chamber. This would benefit studies on the effect of excitation frequency on vortex dynamics, as it would remove the acoustic excitation from the resonance.

7. This investigation found that the vortex-shedding process varies across the span, for example where consecutive vortices do not merge simultaneously across the flow. In practical applications there is greater three-dimensionality which can lead to more complicated flow structures. Hence, the impact of flow three-dimensionality on the measurements from linear arrays of microphones should be studied, along with the benefits of spanwise-distributed arrays to capture the changing dynamics.

PERMISSIONS

September 30, 2015

Andrew R. Lambert
Department of Mechanical & Mechatronice Engineering
University of Waterloo
200 University Avenue West
Waterloo, ON, Canada, N2L 3G1

Hello Andrew,

In response to your request, I hereby grant permission for you to publish content from the following papers in full or in part in your MASc thesis:

1) Lambert, A. R. and Yarusevych, S. Vortex Visualization and Characterization in the Laminar Separation Bubble over a NACA 0018 Airfoil. In Proceedings of the CANCAM 2015 Conference, 3 1 May – 4 June 2015, London, Ontario. Paper # 1111

2) Lambert, A. R. and Yarusevych, S. Analyzing Vortex Dynamics in the Laminar Separation Bubble via Surface Pressure Measurements. In Proceedings of the AIAA Aviation Conference, 22-26 June 2015, Dallas, Texas. Paper Number 2149891

Best regards,

Serhiy Yarusevych, Ph. D., P. Eng.,
Associate Professor
Department of Mechanical & Mechatronics Engineering
University of Waterloo
200 University Avenue West
Waterloo, ON, Canada, N2L 3G1
Phone: (519) 888-4567 x35442
Fax: (519) 885-5862
E-mail: syarus@uwaterloo.ca
Web: www.fmrl.uwaterloo.ca

References

[1] S. Yarusevych, J. G. Kawall, and P. E. Sullivan. Unsteady Separated Flow Characterization on Airfoils Using Time-Resolved Surface Pressure Measurements. *AIAA Journal*, 46(2):508–516, February 2008.

[2] H. P. Horton. *Laminar Separation Bubbles in Two and Three-Dimensional Incompressible Flow*. PhD thesis, Queen Mary College, 1968.

[3] G. L. Brown and A. Roshko. On density effects and large structure in turbulent mixing layers. *Journal of Fluid Mechanics*, 64:775, 1974.

[4] Chih-ming Ho and Lein-saing Huang. Subharmonics and vortex merging in mixing layers, 1982.

[5] Michael S H Boutilier. *Experimental Investigation of Transition over a NACA 0018 Airfoil at a Low Reynolds Number*. PhD thesis, University of Waterloo, 2011.

[6] Thomas M Kirk. *The Later Stages of Transition over a NACA0018 Airfoil at a Low Reynolds Number*. Masc thesis, University of Waterloo, 2014.

[7] T. J. Mueller. The influence of laminar separation and transition on low Reynolds number airfoil hysteresis. *Journal of Aircraft*, 22(9):763–770, September 1985.

[8] P B S Lissaman. Low-Reynolds-Number Airfoils. *Annual Review of Fluid Mechanics*, 15(1):223–239, January 1983.

[9] Michael S Selig. Low Reynolds Number Airfoil Design Lecture Notes VKI Lecture Series Various Approaches to Airfoil Design. Technical Report November, NATO Research and Technology Organization, 2003.

[10] B. H Carmichael. Low Reynolds number airfoil survey, volume 1. Technical report, National Aeronautics and Space Administration, Capistrano Beach, 1981.

[11] M Gaster. The Structure and Behaviour of Laminar Separation Bubbles. Technical Report 3595, Aeronautical Research Council, 1967.

[12] AV Dovgal, VV Kozlov, and A Michalke. Laminar boundary layer separation: instability and associated phenomena. *Progress in Aerospace Sciences*, 30:61–94, 1994.

[13] S. Burgmann and W. Schröder. Investigation of the vortex induced unsteadiness of a separation bubble via time-resolved and scanning PIV measurements. *Experiments in Fluids*, 45(4):675–691, August 2008.

[14] C. D. Winant and F. K. Browand. Vortex pairing : the mechanism of turbulent mixing-layer growth at moderate Reynolds number. *Journal of Fluid Mechanics*, 63:237, 1974.

[15] Itiro Tani. Low-speed flows involving bubble separations. *Progress in Aerospace Sciences*, 5:70–103, January 1964.

[16] Thomas J. Mueller and James D. DeLaurier. a Erodynamics of S Mall V Ehicles. *Annual Review of Fluid Mechanics*, 35:89–111, 2003.

[17] S. Oerlemans, P. Sijtsma, and B. Méndez López. Location and quantification of noise sources on a wind turbine. *Journal of Sound and Vibration*, 299:869–883, 2007.

[18] Olaf Marxen, Matthias Lang, and Ulrich Rist. Vortex formation and vortex breakup in a laminar separation bubble. *Journal of Fluid Mechanics*, pages 58–90, 2013.

[19] Olaf Marxen and Dan S. Henningson. The effect of small-amplitude convective disturbances on the size and bursting of a laminar separation bubble. *Journal of Fluid Mechanics*, 671:1–33, 2011.

[20] Ryan Gerakopulos and Serhiy Yarusevych. Novel time-resolved pressure measurements on an airfoil at a low reynolds number. *AIAA Journal*, 50(5):1189–1200, May 2012.

[21] Michael S. H. Boutilier and Serhiy Yarusevych. Separated shear layer transition over an airfoil at a low Reynolds number. *Physics of Fluids*, 24(8):084105–084105–23, 2012.

[22] Masaru Kiya, Kyuro Sasaki, and Mikio Arie. Discrete-vortex simulation of a turbulent separation bubble, 1982.

[23] M Kiya and K Sasaki. Structure of a turbulent separation bubble. *Journal of Fluid Mechanics*, 137:83–113, 1983.

[24] M Kiya and K Sasaki. Structure of large-scale vortices and unsteady reverse flow in the reattaching zone of a turbulent separation bubble. *Journal of Fluid Mechanics*, 154, 1985.

[25] Laura M. Hudy, Ahmed Naguib, and William M. Humphreys. Stochastic estimation of a separated-flow field using wall-pressure-array measurements. *Physics of Fluids*, 19(2):024103, 2007.

[26] Michaels Selig, James J Guglielmo, Andy P Broeren, and Philippe Giguere. *Summary of Low-Speed Airfoil Data Volume 1*, volume 1. 1995.

[27] Michael S. Selig, Christopher A. Lyon, Philippe Giguere, Cameron P. Ninham, and James J. Guglielmo. *Summary of Low-Speed Airfoil Data*, volume 2. 1996.

[28] Michael S. Selig and James J. Guglielmo. High-Lift Low Reynolds Number Airfoil Design. *Joa*, 34(1):72–79, 1997.

[29] Michael S. Selig and Bryan D. McGranahan. Wind Tunnel Aerodynamic Tests of Six Airfoils for Use on Small Wind Turbines. *Journal of Solar Energy Engineering*, 126(November 2004):986, 2004.

[30] Simon Watkins, Juliette Milbank, Benjamin J. Loxton, and William H. Melbourne. Atmospheric Winds and Their Implications for Microair Vehicles. *AIAA Journal*, 44(11):2591–2600, 2006.

[31] George B. McCullough and Donald E. Gault. Examples of Three Representatine Types of Airfoil-Section Stall at Low Speed. Technical Report September 1951, 1951.

[32] George B. McCullough and Donald E. Gault. Boundary-Layer and Stalling Characteristics of the NACA 64A006 Airfoil Section. Technical Report 1923, National Advisory Committee for Aeronautics, Moffett Field, 1949.

[33] Aerodynamics of the Model Airplane. Part I. Airfoil Measurements. *Redstone Scientific Information Centre*, (RSIC-721), 1967.

[34] B. Melvill Jones. An Experimental Study of the Stalling of Wings. *British A. R. C.*, 38(285):753–770, 1934.

[35] B. Melvill Jones. Stalling. *Journal of the Royal Aeronautical Society*, 38(285):753–770, 1934.

[36] George B. McCullough. The Effect of Reynolds Number on the Stalling Characteristics and Pressure Distributions of Four Moderately Thin Airfoil Sections. Technical report, National Advisory Committee for Aeronautics, Moffett Field, 1955.

[37] Robert H Liebeck. A class of airfoils designed for high lift in incompressible flow. *Journal of Aircraft*, 10(10):610–617, 1973.

[38] Michael S. H. Boutilier and Serhiy Yarusevych. Parametric study of separation and transition characteristics over an airfoil at low Reynolds numbers. *Experiments in Fluids*, 52(6):1491–1506, February 2012.

[39] Thomas. J. Mueller and Stephen M. Batill. Experimental studies of the Eppler 61 airfoil at low Reynolds numbers. 20(4):1982, 1982.

[40] T. J. Mueller, L. J. Pohlen, P. E. Conigliaro, and B. J. Jansen. The influence of free-stream disturbances on low Reynolds number airfoil experiments. *Experiments in Fluids*, 1:3–14, 1983.

[41] Itiro Tani. Boundary-Layer Transition. *Annual Review of Fluid Mechanics*, 1:169–196, 1969.

[42] D C Mccormick. Boundary Layer Separation Control with Directed Synthetic Jets. *AIAA-Paper*, pages 2000–0519, 2000.

[43] Delay of Airfoil Stall by Periodic Excitation. *Journal of Aircraft*, 33(4):691–698, 1996.

[44] Wei Zhang, Rainer Hain, and Christian J. Kähler. Scanning PIV investigation of the laminar separation bubble on a SD7003 airfoil. *Experiments in Fluids*, 45(4):725–743, September 2008.

[45] Thomas C. Corke, C. Lon Enloe, and Stephen P. Wilkinson. Dielectric Barrier Discharge Plasma Actuators for Flow Control*. *Annual Review of Fluid Mechanics*, 42:505–529, 2010.

[46] L. E. Jones, R. D. Sandberg, and N. D. Sandham. Direct numerical simulations of forced and unforced separation bubbles on an airfoil at incidence. *Journal of Fluid Mechanics*, 602:175–207, April 2008.

[47] C-M Ho and Patrick Huerre. Perturbed Free Shear Layers. *Annual Review of Fluid Mechanics*, 16(1):365–424, January 1984.

[48] O Marxen, M Lang, U Rist, and S Wagner. A Combined Experimental/Numerical Study of Unsteady Phenomena in a Laminar Separation Bubble. *Flow, Turbulence and Combustion*, 71:133–146, 2003.

[49] C. D. Winant and F. K. Browand. Vortex pairing : the mechanism of turbulent mixing-layer growth at moderate Reynolds number. *Journal of Fluid Mechanics*, 63:237, 1974.

[50] I. Lee and H. J. Sung. Characteristics of wall pressure fluctuations in separated flows over a backward-facing step: Part 1. Time-mean statics and cross-spectral analyses. *Experiments in Fluids*, 30:273–282, 2001.

[51] I. Lee and H. J. Sung. Characteristics of wall pressure fluctuations in separated flows over a backward-facing step: Part II. Unsteady wavelet analysis. *Experiments in Fluids*, 30:273–282, 2001.

[52] T. R. Troutt, S. Bhattacherjee, and B. Scheelke. Modification of vortex interactions in a reattaching separated flow. *AIAA Journal*, 24:623–629, 1986.

[53] T. M. Farabee and M. J. Casarella. Measurements of Fluctuating Wall Pressure for Separated / Reattaohed Boundary Layer Flows. *Journal of Vibration, Acoustics, Stress, and Reliability in Design*, 108(July):301–307, 1986.

[54] Laura M. Hudy, Ahmed M. Naguib, and William M. Humphreys. Wall-pressure-array measurements beneath a separating/reattaching flow region. *Physics of Fluids*, 15(3):706–717, 2003.

[55] Jonathan H. Watmuff. Evolution of a wave packet into vortex loops in a laminar separation bubble. *Journal of Fluid Mechanics*, 397:119–169, October 1999.

[56] M Gaster. Laminar Separation Bubbles. pages 1–13, 2006.

[57] Rolf E. Radespiel, Jan Windte, and Ulrich Scholz. Numerical and Experimental Flow Analysis of Moving Airfoils with Laminar Separation Bubbles. *AIAA Journal*, 45:1346–1356, 2007.

[58] B C Khoo, Y T Chew, and C J Teo. On near-wall hot-wire measurements. *Experiments in Fluids*, 29:448–460, 2000.

[59] S. Yavuzkurt. A Guide to Uncertainty Analysis of Hot-Wire Data. *Journal of Fluids Engineering*, 106:181, 1984.

[60] S. Becker, C. M. Stoots, K. G. Condie, F. Durst, and D. M. McEligot. LDA-Measurements of Transitional Flows Induced by a Square Rib. *Journal of Fluids Engineering*, 124(March):108, 2002.

[61] M J Crompton and R V Barrett. Investigation of the separation bubble formed behind the sharp leading edge of a flat plate at incidence. *Proceedings of the Institution of Mechanical Engineers, Part G: Journal of Aerospace Engineering*, 214:157–176, 2000.

[62] Stavros Tavoularis. *Summary of Low-Speed Airfoil Data*. Cambridge University Press, New York, 1996.

[63] U. Rist, M. Lang, and S. Wagner. Investigations on controlled transition development in a laminar separation bubble by means of LDA and PIV. *Experiments in Fluids*, 36(1):43–52, January 2004.

[64] Sebastian Burgmann, Wolfgang Schröder, and Christoph Brücker. Volumetric measurement of vortical structures in the reattachment region of a laminar separation bubble using stereo scanning PIV. (1228):26–29, 2006.

[65] M. M. O'Meara and T. J. Mueller. Laminar separation bubble characteristics on an airfoil at low Reynolds numbers. *AIAA Journal*, 25(8):1033–1041, 1987.

[66] Michael S.H. Boutilier and Serhiy Yarusevych. Sensitivity of linear stability analysis of measured separated shear layers. *European Journal of Mechanics - B/Fluids*, 37:129–142, January 2013.

[67] Michael V Ol, Brian R. McAuliffe, Ernest S. Hanff, Ulrich Scholz, and Christian J. Kähler. Comparison of Laminar Separation Bubble Measurements on a Low Reynolds Number Airfoil in Three Facilities. *35th AIAA Fluid Dynamics Conference and Exhibit*, (June):11, 2005.

[68] M Alam and N D Sandham. Direct numerical simulation of "short" laminar separation bubbles with turbulent reattachment. *Journal of Fluid Mechanics*, 403:223–250, 2000.

[69] R Hillier and NJ Cherry. The effects of stream turbulence on separation bubbles. *Journal of Wind Engineering and Industrial Aerodynamics*, 8:49–58, 1981.

[70] N. J. Cherry, R. Hillier, and M. E. M. P. Latour. Unsteady measurements in a separated and reattaching flow. *Journal of Fluid Mechanics*, 144(-1):13, April 1984.

[71] L. W. Sigurdson. The structure and control of a turbulent reattaching flow. *Journal of Fluid Mechanics*, 298:139, 1995.

[72] I. Lee, S. K. Ahn, and H. J. Sung. Three-dimensional coherent structure in a separated and reattaching flow over a backward-facing step. *Experiments in Fluids*, 36:373–383, 2004.

[73] T. Nakano, N. Fujisawa, Y. Oguma, Y. Takagi, and S. Lee. Experimental study on flow and noise characteristics of NACA0018 airfoil. *Journal of Wind Engineering and Industrial Aerodynamics*, 95:511–531, 2007.

[74] R. Hain, C. J. Kähler, and R. Radespiel. Dynamics of laminar separation bubbles at low-Reynolds-number aerofoils. *Journal of Fluid Mechanics*, 630:129, June 2009.

[75] S Yarusevych, P E Sullivan, and J G Kawall. Smoke-Wire Flow Visualization in Separated Flows at Relatively High Velocities. *AIAA Journal*, 47(6):1592–1595, 2009.

[76] Laura L. Pauley, Parviz Moin, and William C. Reynolds. The structure of two-dimensional separation. *Journal of Fluid Mechanics*, 220:397, 1990.

[77] C. P. Haggmark, A. A. Bakchinov, and P. H. Alfredsson. Experiments on a Two-Dimensional Laminar Separation Bubble. 358(1777):3193–3205, 2000.

[78] U Maucher, U Rist, M Kloker, and S Wagner. DNS of laminar-turbulent transition in separation bubbles. *High Performance Computing in Science and Engineering 99*, pages 279–294, 2000.

[79] Patrick Huerre and Peter Monkewitz. Local and global instabilities in spatially developping flows. *Annual Review of Fluid Mechanics*, 22:473–537, 1990.

[80] Ulrich Rist and Kai Augustin. Control of Laminar Separation Bubbles Using Instability Waves. *AIAA Journal*, 44(10):2217–2223, 2006.

[81] F. K. Browand and P. D. Weidman. Large scales in the developing mixing layer. *Journal of Fluid Mechanics*, 76:127, 1976.

[82] C. Cerretelli and C. H. K. Williamson. The physical mechanism for vortex merging, 2003.

[83] Patrice Meunier, Stéphane Le Dizès, and Thomas Leweke. Physics of vortex merging. *Comptes Rendus Physique*, 6:431–450, 2005.

[84] E. Hopfinger. Vortices in Rotating Fluids. *Annual Review of Fluid Mechanics*, 25:241–289, 1993.

[85] Patrice Meunier, Uwe Ehrenstein, Thomas Leweke, and Maurice Rossi. A merging criterion for two-dimensional co-rotating vortices. *Physics of Fluids*, 14(2002):2757–2766, 2002.

[86] Frederick W. Roos and Jerome T. Kegelman. Control of coherent structures in reattaching laminar and turbulent shear layers. *AIAA Journal*, 24:1956–1963, 1986.

[87] T. R. Troutt, B. Scheelke, and T. R. Norman. Organized structures in a reattaching separated flow field. *Journal of Fluid Mechanics*, 143:413, 1984.

[88] Dan Palumbo. Determining correlation and coherence lengths in turbulent boundary layer flight data. *Journal of Sound and Vibration*, 331(16):3721–3737, July 2012.

[89] Boris Phillippe Chagnaud, Horst Bleckmann, and Jacob Engelmann. Neural responses of goldfish lateral line afferents to vortex motions. *The Journal of experimental biology*, 209:327–342, 2006.

[90] Boris P. Chagnaud, Horst Bleckmann, and Michael H. Hofmann. K??rm??n vortex street detection by the lateral line. *Journal of Comparative Physiology A: Neuroethology, Sensory, Neural, and Behavioral Physiology*, 193:753–763, 2007.

[91] Vicente I. Fernandez, Stephen M. Hou, Franz S. Hover, Jeffrey H. Lang, and Michael S. Triantafyllou. Lateral-line-inspired MEMS-array Pressure Sensing for Passive Underwater navigation. Technical report, Massachusetts Institute of Technology, Cambridge, Massach, 2007.

[92] Dagmar Vogel and Horst Bleckmann. Behavioral discrimination of water motions caused by moving objects. *Journal of Comparative Physiology - A Sensory, Neural, and Behavioral Physiology*, 186(12):1107–1117, 2000.

[93] Dennis G. Mabey. Analysis and Correlation of Data on Pressure Fluctuations in Separated Flow. *Journal of Aircraft*, 9(9):642–645, 1972.

[94] Robert W. Paterson, Paul G. Vogt, Martin R. Fink, and C. Lee Munch. Vortex Noise of Isolated Airfoils. *Journal of Aircraft*, 10:296–302, 1973.

[95] Serhiy Yarusevych, Pierre E. Sullivan, and John G. Kawall. On vortex shedding from an airfoil in low-Reynolds-number flows. *Journal of Fluid Mechanics*, 632:245–271, July 2009.

[96] Ryan J. Gerakopulos. Investigating flow over an airfoil at low Reynolds numbers using novel time-resolved surface pressure measurements. 2011.

[97] Ryan J. Gerakopulos. *Investigating flow over an airfoil at low Reynolds numbers using novel time-resolved surface pressure measurements*. PhD thesis, University of Waterloo, 2011.

[98] L.E. Jones, R.D. Sandberg, and N.D. Sandham. *Stability and receptivity characteristics of a laminar separation bubble on an aerofoil*, volume 648. 2010.

[99] T. Lee and P. Gerontakos. Investigation of flow over an oscillating airfoil. *Journal of Fluid Mechanics*, 512:313–341, 2004.

[100] Marie Farge. Wavelet Transforms and their Applications to Turbulence. *Annual Review of Fluid Mechanics*, 24(Holschneider 1991):395–457, 1992.

[101] S.H. Chue. Pressure probes for fluid measurement. *Progress in Aerospace Sciences*, 16(2):147–223, 1975.

[102] Robert J. Moffat. Describing the uncertainties in experimental results. *Experimental Thermal and Fluid Science*, 1(1):3–17, 1988.

APPENDICES

Appendix A

Experimental Uncertainty

Every experimental measurement has an uncertainty associated with it, so the uncertainties for the measurements performed in this thesis are presented in this section. There is uncertainty associated with the experimental setup, static pressure measurements, microphone measurements, and quantities derived from flow visualizations. These uncertainties and the methods by which they were estimated are outlined for their individual components.

A.1 Uncertainty in Experimental Setup

For these experiments, the primary factors that are used to define the flow conditions are the chord-based Reynolds number (Re_c) and the Angle of Attack (AOA). These factors both have uncertainty associated with them, and as a result there is some uncertainty in the actual conditions under which experiments were performed. The factors that combine into the overall uncertainty for Re_c and AOA are described below.

The chord Reynolds number is calculated based on the length of the airfoil, the free-stream velocity, and the kinematic viscosity of the fluid. The airfoil has a chord length of $200mm \pm 0.5$ mm for an uncertainty of 0.25%. The velocity within the test section is set based on a curve fit of the pressure drop over the wind tunnel contraction. The relationship between the contraction pressure drop and the pitot-static pressure difference in the test section was fit with a curve to determine the velocity from the contraction pressure. The inclined manometer used to measure the pressures has a resolution of 0.25 Pa, and was used both for the contraction pressure measurements as well as those performed on the

pitot-static tube. The uncertainty in manometer readings is estimated as 0.5 Pa. With the velocity allowed to fluctuate within 1% over time, this gives an uncertainty in the velocity of 2% at the velocities encountered.

The uncertainty in setting the angle of attack for the airfoil depends both on the accuracy of determining the zero-degree angle of attack and the accuracy of setting the experimental angle of attack. The airfoil zeroing results in a bias error while the protractor precision results in a random error. The protractor used in this series of experiments has a resolution of 0.1°. At low Reynolds numbers and angles of attack particularly, there is increased uncertainty compared to higher speeds in determining $AOA = 0°$ directly as the zero-lift angle of attack. The pressure distributions at these angles and Reynolds numbers have a sensitivity to experimental conditions and imperfections in airfoil geometry. To zero the airfoil, the same procedure as described by Kirk [6] was used. First, pressure distributions were taken at a range of positive and negative angles near ±5° and ±10°. Second, the pressure distributions at these angles of attack were compared to determine where they were the most symmetrical. The uncertainty in determining symmetry is 0.1°. Combining the uncertainty in the protractor and the zeroing method, the resulting uncertainty in the angle of attack is 0.22°.

A.2 Uncertainty in Static Pressure Measurements

In this section, the factors that contribute to the uncertainty in the mean surface pressure measurements are analyzed. The uncertainty in quantities derived from these pressures are also examined.

The calibration of the pressure transducer poses the largest contribution to the uncertainty in the pressure measurements. The pressure transducers used in this investigation are a pair of Lucas Schaevitz P3061-2WD pressure transducers. The output voltages of these transducers were read by a National Instruments NI PCI-6221 data acquisition system with 16-bit precision. The uncertainty due to the precision of the system is estimated to be less than 0.05 Pa. The calibration was performed against a Druck DPI 610 pressure calibrator with a differential pressure range of 5 inches of water, or 1250 Pa. The accuracy of the calibrator is 0.05% of full-scale, which is 0.0025 "H_2O or 0.625 Pa. For the calibrations of the pressure transducers, the pressure calibrator was used to apply a pressure difference to the pressure transducer. The pressure measured by the calibrator and the corresponding voltage outputs from the pressure transducer were recorded for around 12 pressures within the range expected to be encountered in the experiments. The uncertainty in the calibration linear fit is less than 0.03 Pa.

The calibration of the pressure transducers is also impacted by the temperature changes that the transducer experiences through time. The manufacturer-specified temperature drift for these pressure transducers increases uncertainty by 0.25 Pa/°C. The calibration procedure takes a short period of time, so the temperature drift over this period is assumed to be negligible. The experiments were performed within 1°C of the calibration temperature, so the uncertainty for measurements between days is estimated as 0.25 Pa.

Additional effects such as pressure tap geometry, pressure measurement settling time, and the number of samples taken contribute to the uncertainty in the measured pressures compared with the actual surface pressures. Boutilier [5] estimated the uncertainty in measured pressure from the pressure tap geometry as less than 0.13 Pa using the results summarized by Chue [101]. The measurements of surface pressure are performed sequentially between pressure taps along the airfoil. The rise time between pressure measurements was set based on an investigation by Boutilier [5]. The rise time and measurement lengths were set to result in a combined uncertainty of less than 0.13 Pa.

These factors of experimental uncertainty were combined into an overall uncertainty in pressure measurements following the methodology of Moffat [102] of $C_p = \pm 0.022$. The pressure distributions are also used to identify the positions of Separation, Transition and Reattachment. Due to the defined pressure plateaus, the uncertainty in determining these locations is half of the spacing of the pressure taps.

A.3 Microphone Measurement Uncertainty

The uncertainty in the fluctuating surface pressure measurements are caused by uncertainty in the calibration as well as the noise level experienced at the microphones. The microphones were individually calibrated by Gerakopulos [96] against a reference microphone in an anechoic chamber. Their response was found to be flat up to 2000 Hz, with error due to nonlinearity of 7%. A linear response to pressure amplitude was found for amplitudes from 1 Pa to 36 Pa. The error in calibration was estimated as less than 20% of the measurement [5]. The microphones encounter electrical noise as well as acoustic noise sources, which include the fan, DC generator for the motor, and HVAC system in the laboratory. The noise bias level was determined to be the lowest pressure fluctuations encountered with the wind tunnel running, the same method as used by Boutilier [5]. This value was also found to be around 0.02 times the dynamic pressure. When these error sources are combined as recommended by Moffat [102], the resulting uncertainty on the coefficients of pressure is $\sqrt[2]{0.02^2 + 0.2C_p^2}$.

A.4 Flow Visualization Uncertainty

The flow visualizations and their synchronization with microphone measurements are subject to uncertainty in locating the visualizations relative to the microphones, and aligning the images and microphone measurements in time. The positions of the microphones on the visualizations have a bias error and error in scaling. The scales were determined using images of the scale along the airfoil acquired in the visualization plane and measuring the number of pixels corresponding to a known length. Distances were on the order of 0.05 m and 900 pixels, with an uncertainty estimated as 6 pixels for the length, or an error of 0.7%. The absolute locations of the images were determined from the scale, with a bias error estimated at less than 4 pixels, or 0.001 x/c. The locations of the smoke wires were used as the reference locations. The combined error is $\sqrt[2]{0.001^2 + (0.007(x/c - x_{wire}/c))^2}$.

To synchronize the microphones with the high-speed images, the trigger signal and laser pulse signal were acquired. The uncertainty in the trigger signal and laser signal is estimated as the time period of the microphone measurements taken at 40 kHz. This gives the uncertainty in the synchronization as less than 0.005 ms.

Rates of vortex shedding were calculated based on taking the number of frames (typically around 300) required for at least 50 vortices to be shed. The resulting uncertainty in the frequency is estimated as 4% of the resulting frequency estimate.

A.5 Vortex Tracking by Pressure Signals Uncertainty

The uncertainty in quantities derived from the pressure signal vortex tracking depends on the uncertainty in microphone locations, temporal resolution of the measurements, and the accuracy of the detected events. The resolution of time intervals between vortices is 0.025 ms, or 3% of the shortest average time interval, which is seen at $AOA = 10°$. The uncertainty in velocity measurements also depends on the uncertainty in the positions of the microphones, which is estimated as the diameter of the pressure tap hole, 0.8 mm or 9% of the microphone spacing. The uncertainty in individual velocities given a typical 60 samples between detections at subsequent microphones is 9.4%.

The uncertainty in numbers of vortex merges was estimated from the comparison of counts of merging made from flow visualizations and the microphone vortex-tracking methods. To gather a reference of vortex dynamics to compare with tracking techniques, vortices were tracked in 1500 frames of visualizations at $AOA = 8°$. The number of overall

vortices identified as merging from the visualization were compared, and found that the microphones identified the overall number of merges to within 20%.

Appendix B

Separation Bubble Flow Visualization

Separation bubbles are known to be sensitive to the disturbance environment. When measurements are taken over airfoils at low Reynolds numbers, care must be taken to ensure that disturbances that alter the flow physics aren't introduced. I these experiments, a smoke-wire was introduced into the separation bubble at $x/c = 0.66$ at $AOA = 0°$, $x/c = 0.33$ at $AOA = 5°$, $x/c = 0.21$ at $AOA = 8°$, and $x/c = 0.13$ at $AOA = 10°$. The impact of the visualization technique is analyzed in this section

The mean surface pressure distributions over the airfoil at $AOA = 0°$, $5°$, $8°$, and $10°$ are presented in Figs. B.1a-B.1d both with and without the smoke-wire equipment in place. These distributions show similar shapes in the surface pressure distributions for the airfoil in its clean condition as well as with the smoke-wire. The pressures overall are slightly lower for the cases with the smoke wire. The smoke-wire equipment in the wind tunnel slightly increases the solid blockage and wake blockage, which increases the velocity over the center portion of the airfoil. To within the spatial resolution of the microphones, the pressure plateaus maintain their locations at all of the angles of attack.

The rms of the fluctuating pressures is shown in Figs. B.2a-B.2c for $AOA = 5°$, $8°$, and $10°$ with and without the smoke wire. The measurements with the wire in the separation bubble were made during visualization runs to include any effect from activating the smoke-wire. The pressure fluctuations follow the same trends when the smoke wire is introduced, with some changes in the levels of pressure fluctuations along the separation bubble. The locations of the peaks in rms levels remain the same at all of the angles studied. Elsewhere the pressure levels tend to remain within the uncertainty on the fluctuating pressure. The changes indicate only a small change in the locations where the structures develop.

The power spectra of the microphone signals are presented in Figs. B.3-B.5 for $AOA =$

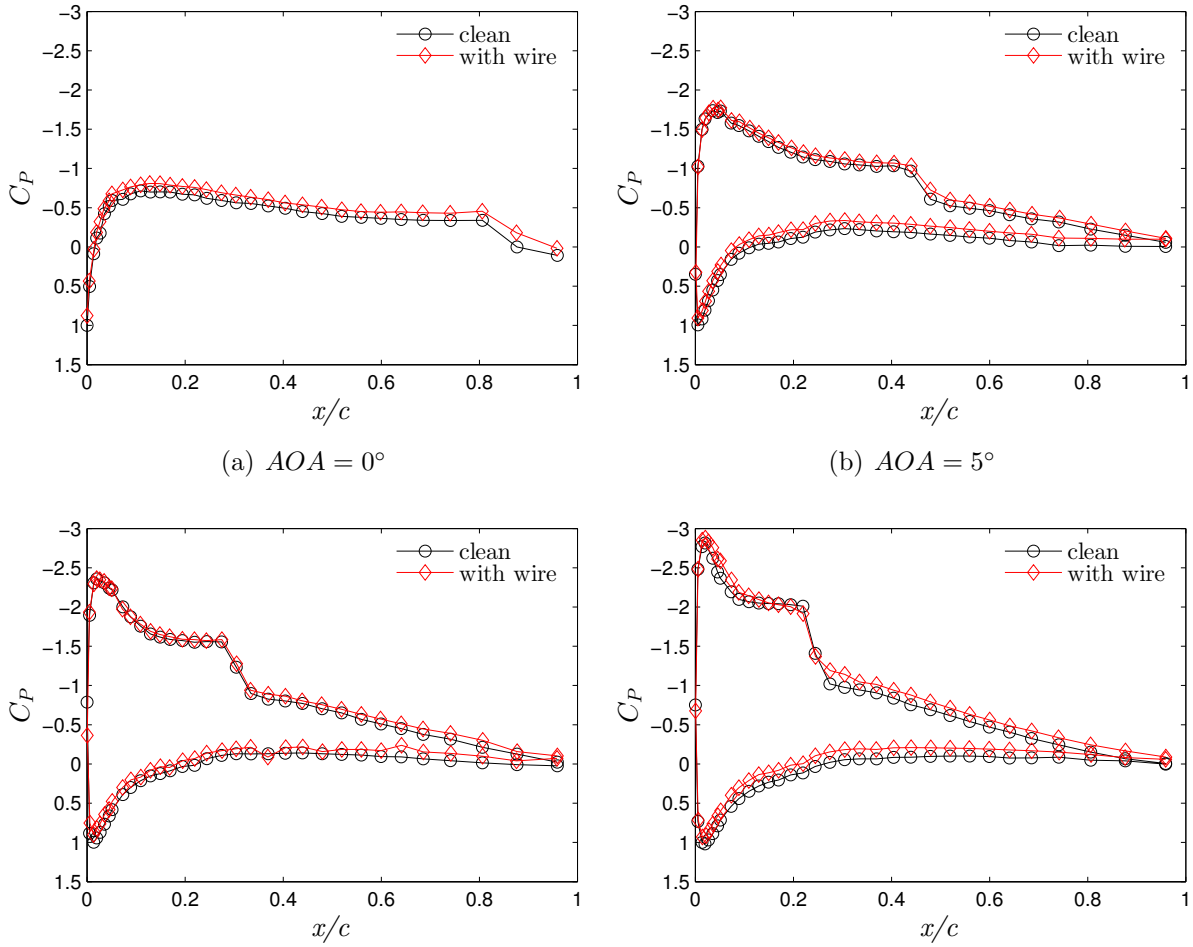

(a) $AOA = 0°$

(b) $AOA = 5°$

(c) $AOA = 8°$

(d) $AOA = 10°$

Figure B.1: Mean surface pressure distributions along the airfoil are presented for $AOA = 0°$, $5°$, $8°$, and $10°$ with and without the smoke wire in the separation bubble. Uncertainty is on the order of the symbol size.

$5°$, $8°$, and $10°$. The spectra are shown for the clean airfoil and for the microphone measurements captured during flow visualizations, as in Figs. B.2a-B.2c. The spectra are recorded downstream of where the smoke-wire, and do not show the addition of high-frequency content as would be expected if there was vortex shedding from the wire. These spectra show very similar development of the amplified bands of the spectra between the cases. At $AOA = 5°$ in B.3 and $AOA = 8°$ in B.4 the amplified bands shift very slightly to higher

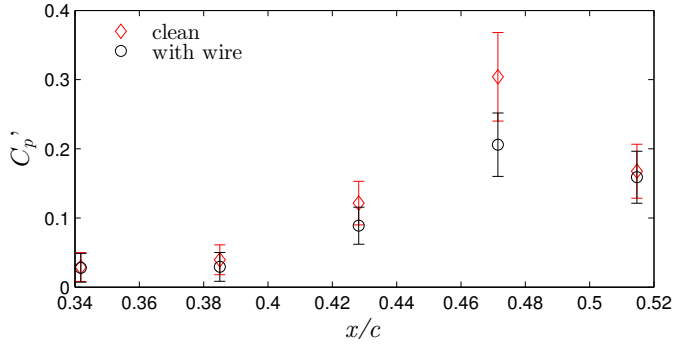

(a) $AOA = 5°$

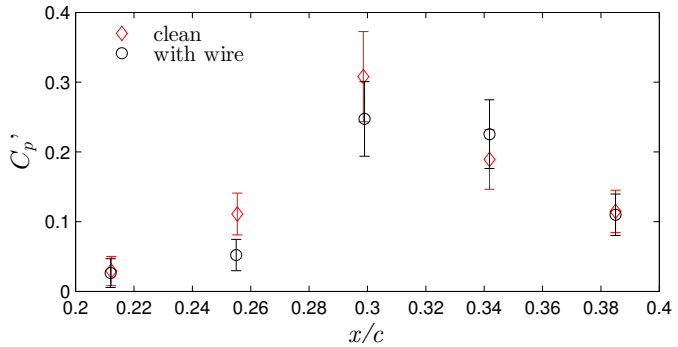

(b) $AOA = 8°$

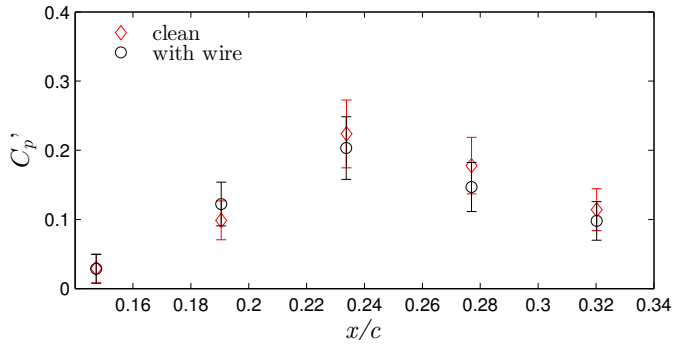

(c) $AOA = 10°$

Figure B.2: Root-mean-square of pressure fluctuations along the airfoil are presented for $AOA = 5°$, $8°$, and $10°$ with and without the smoke wire in the separation bubble.

frequencies, visible as the bands shift slightly from the acoustic peaks at 570 and 760 Hz respectively. This is expected from the slightly increased blockage with the flow visualization equipment. The bands of frequencies show some variation in their development along the chord between the cases with and without the smoke wire. At $AOA = 5°$ the spectra for $x/c = 0.43$ show greater content around $f \approx 250$ Hz for the clean airfoil than with the wire. This also occurs for $AOA = 8°$ in the spectra for $x/c = 0.26$. However, while there are slight variations in where the fluctuations at certain frequencies show growth, the overall spectral shapes are maintained for the different cases. The similarities between the measurements with and without the smoke wire present give confidence that the vortex activity that is visualized represents what occurs on the natural airfoil.

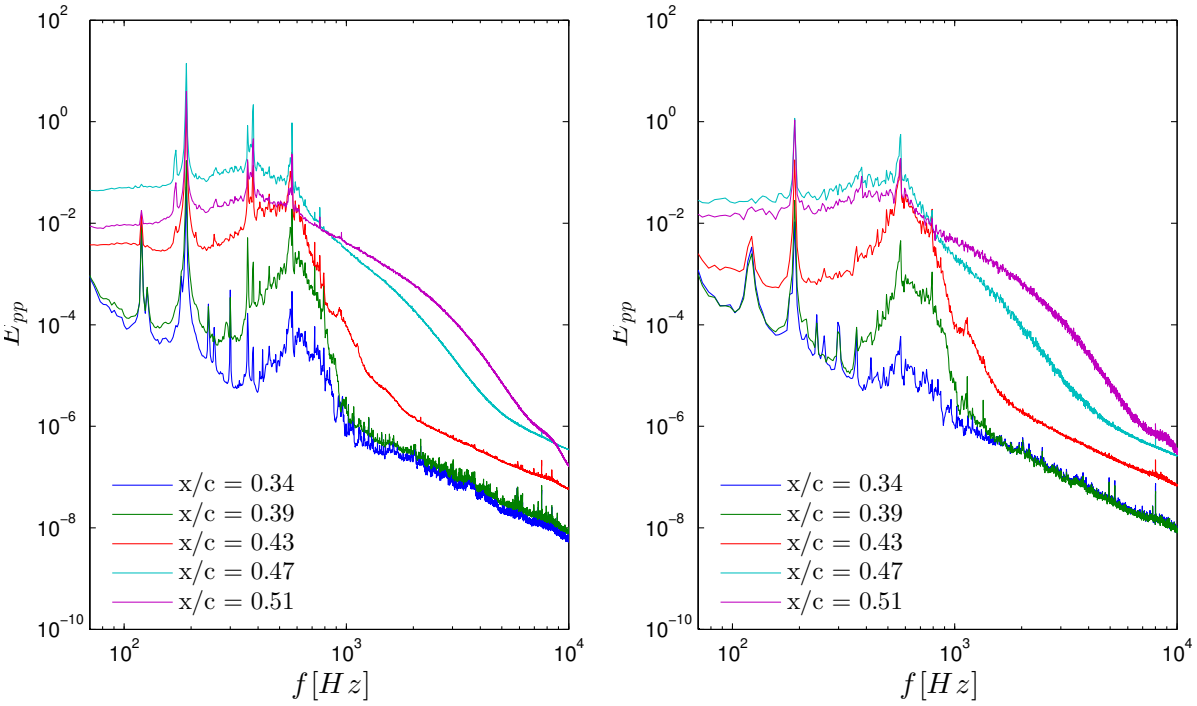

(a) Clean Airfoil

(b) Wire in LSB

Figure B.3: Pressure spectra along the airfoil are presented for $AOA = 5°$, with and without the smoke wire in the separation bubble.

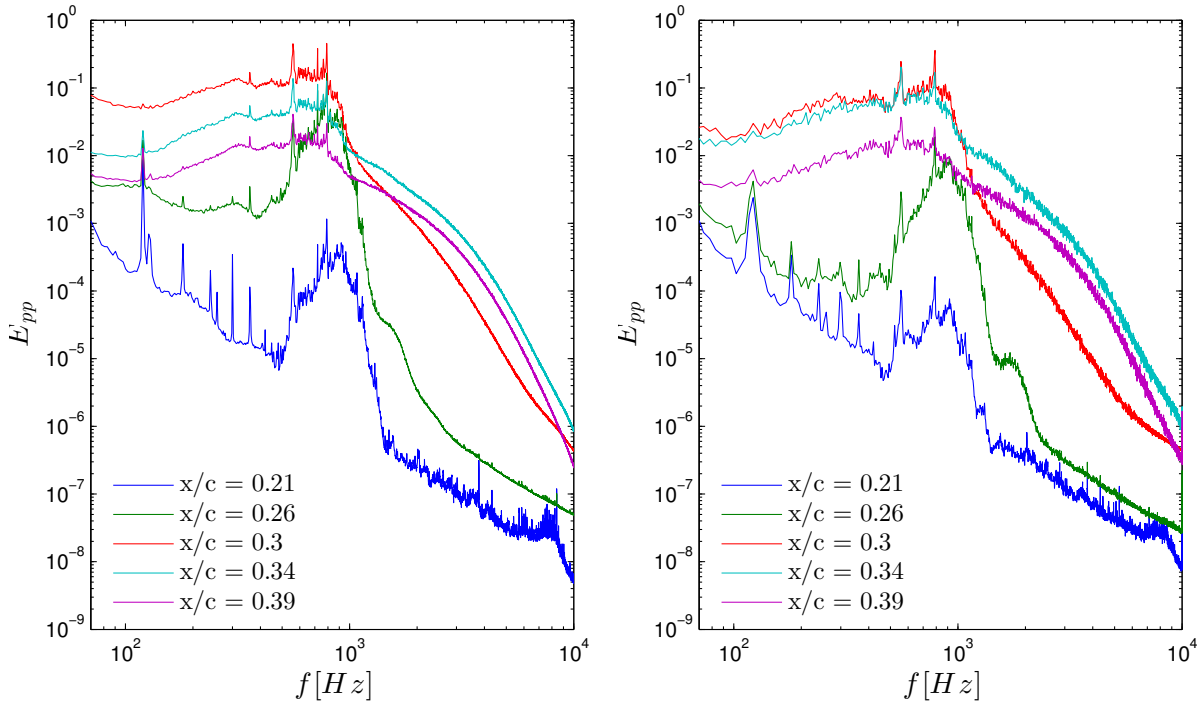

(a) Clean Airfoil

(b) Wire in LSB

Figure B.4: Pressure spectra along the airfoil are presented for $AOA = 8°$, with and without the smoke wire in the separation bubble.

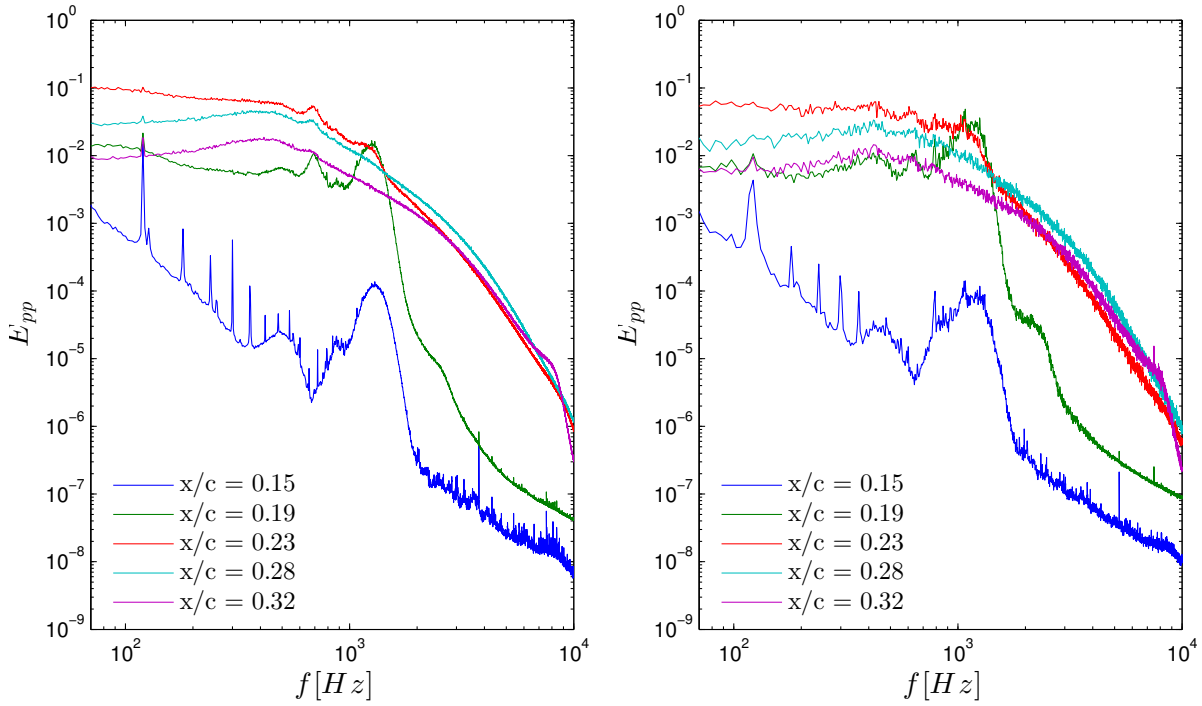

(a) Clean Airfoil

(b) Wire in LSB

Figure B.5: Pressure spectra along the airfoil are presented for $AOA = 10°$, with and without the smoke wire in the separation bubble.